QUANTUM THERMAL CONDUCTIVITY OF LOW-DIMENSIONAL DISORDERED MATERIALS

A Thesis Submitted to
the Graduate School of Engineering and Sciences of
İzmir Institute of Technology
in Partial Fulfillment of the Requirements for the Degree of

DOCTOR OF PHILOSOPHY

in Materials Science and Engineering

by
Gizem KURT

December, 2023
İZMİR

We approve the thesis of **Gizem KURT**

Examining Committee Members:

Prof. Dr. Hâldun SEVİNÇLİ
Department of Materials Science and Engineering, İzmir Institute of Technology

Prof. Dr. Alev Devrim GÜÇLÜ
Department of Physics, İzmir Institute of Technology

Asst. Prof. Dr. Mahmut Barış OKATAN
Department of Materials Science and Engineering, İzmir Institute of Technology

Prof. Dr. Serpil ŞAKİROĞLU
Department of Physics, Dokuz Eylül University

Prof. Dr. Gürsoy Bozkurt AKGÜÇ
Department of Physics, İzmir University of Economics

08/12/2023

Prof. Dr. Hâldun SEVİNÇLİ
Supervisor, Department of Materials Science and Engineering, İzmir Institute of Technology

Assoc. Prof. Dr. Özgür ÇAKIR
Co-Supervisor, Department of Physics, İzmir Institute of Technology

Prof. Dr. Yaşar AKDOĞAN
Head of the Department of Materials Science and Engineering

Prof. Dr. Mehtap EANES
Dean of the Graduate School

ACKNOWLEDGMENTS

First, I would like to express my sincere thanks to my esteemed advisor, Prof. Dr. Hâldun SEVİNÇLİ, who made it possible for me to continue by not giving up on me even when I gave up on myself, and to İdil Merve KARAOĞLU, who made it possible for me to write my master's thesis and thus do a doctorate. Many thanks also to Prof. Dr. Durmuş Ali DEMİR, who patiently and engagedly answered every question I asked while doing the tunneling work. I want to thank all my committee members for their valuable feedbacks and my former jury member, Dr. Aziz GENÇ, for his contributions.

I am also grateful to Mustafa Neşet ÇINAR for his help in writing the Kubo-Greenwood code and to Şamil ŞİRİN for introducing me to parallel programming. Also, I would like to thank my group and office mate Hazan ÖZKAN for her friendship and support during the most challenging times of the thesis. Last but not least, I want to express my sincere gratitude to my family, who believed in me at every moment of my long educational life and stood by me in every difficulty with their positive perspective.

I acknowledge support from TÜBİTAK (119F353) and TÜBİTAK (117F480), and computations are partially performed on TÜBİTAK ULAKBİM, High-Performance and Grid Computing Center (TRUBA resources).

ABSTRACT

QUANTUM THERMAL CONDUCTIVITY OF LOW-DIMENSIONAL DISORDERED MATERIALS

The shrinking of technological devices leads to the emergence of exotic heat conduction behaviors such as quantization of thermal conductivity, phonon tunneling, and ballistic conduction. Understanding and exploiting these quantum effects is crucial for advancing technologies such as thermal management and designing advanced materials in nanoscale systems. This research has focused on two topics: the possibility of constructing a device based on phonon tunneling and the quantum thermal conductivity of amorphous graphene, which shows quantum effects on room temperature due to strong carbon-carbon bonds. In doing so, we calculated the transmission coefficients using Green's functions for both systems, and the Kubo-Greenwood method was used additionally for amorphous graphene. We worked in the harmonic limit since the scattering due to the material's internal structure is the dominant scattering mechanism in disordered materials. Thermal conductivities were calculated using the Landauer formulation. For the distribution function in the Landauer formula, two different distribution functions, Bose-Einstein and Maxwell-Boltzman, were used to determine the quantum and classical thermal conductivities.

A thermal chromator and a medium with a phononic gap were adjoined and placed between two thermal reservoirs to construct the phonon tunneling device. The dependency of transport properties on the gap system's length is investigated. Results reveal the possibility of building such a device. Besides, the classical thermal conductivities of amorphous graphene are almost twice as high as the quantum thermal conductivity, which shows that quantum thermal conductivity determines the thermal properties in high Debye materials where phonon-phonon interactions are suppressed.

ÖZET

DÜŞÜK BOYUTLU DÜZENSİZ MALZEMELERİN KUANTUM ISIL İLETKENLİĞİ

Teknolojik cihazların küçülmesi, termal iletkenliğin kuantizasyonu, fonon tünellemesi ve balistik iletim gibi egzotik ısı iletimi davranışlarının ortaya çıkmasına neden olmaktadır. Bu kuantum etkilerinin anlaşılması ve kullanılması, termal yönetim gibi teknolojilerin ilerletilmesi ve nano ölçekli sistemlerde gelişmiş malzemelerin tasarlanması için çok önemlidir. Bu araştırma iki konuya odaklanmıştır: fonon tünellemesine dayalı bir cihaz inşa etme olasılığı ve güçlü karbon-karbon bağları nedeniyle oda sıcaklığında kuantum etkileri gösteren amorf grafenin kuantum termal iletkenliği. Bunu yaparken, her iki sistem için de Green fonksiyonlarını kullanarak iletim katsayılarını hesapladık ve amorf grafen için ek olarak Kubo-Greenwood yöntemini kullandık. Malzemenin iç yapısından kaynaklanan saçılma, düzensiz malzemelerdeki baskın saçılma mekanizması olduğundan harmonik limitte çalıştık. Termal iletkenlikler Landauer formülasyonu kullanılarak hesaplanmıştır. Landauer formülündeki dağılım fonksiyonu için, kuantum ve klasik termal iletkenlikleri belirlemek üzere Bose-Einstein ve Maxwell-Boltzman olmak üzere iki farklı dağılım fonksiyonu kullanılmıştır.

Fonon tünelleme cihazını oluşturmak için bir termal kromatör ve fononik bant boşluklu bir ortam bitişik hale getirilmiş ve iki termal rezervuar arasına yerleştirilmiştir. Taşıma özelliklerinin boşluk sisteminin uzunluğuna bağımlılığı araştırılmıştır. Sonuçlar böyle bir cihazın inşa edilebileceğini ortaya koymaktadır. Ayrıca, amorf grafenin klasik termal iletkenlikleri kuantum termal iletkenliğinin neredeyse iki katıdır, bu da kuantum termal iletkenliğinin fonon-fonon etkileşimlerinin bastırıldığı yüksek Debye malzemelerindeki termal özellikleri belirlediğini göstermektedir.

To my mom, my family, and John Francis Anthony Pastorius III...

TABLE OF CONTENTS

LIST OF FIGURES

LIST OF TABLES

LIST OF SYMBOLS

SYMBOL	EXPLANATION
H	Hamiltonian
D	Dynamical matrix
Φ	Force Constants
X	Position Matrix
U	Total Interatomic Potential
ω	Angular Frequency
ω_{crf}	Common Resonance Frequency
ν	Frequency ($\omega = 2\pi\nu$)
$v_g(\omega)$	Average Group Velocity
$\boldsymbol{q},\ \boldsymbol{Q}$	Wave Vectors
k_B	Boltzman Constant
h	Planck Constant
$\hbar$	Reduced Planck's Constant ($\hbar = h/2\pi$)
κ	Thermal Condcutivity
G	Thermal Conductance
$\hat{J}$	Heat Flux
Ξ	Transmission
T	Temperature
$M,\ m$	Atomic Masses

SYMBOL	EXPLANATION
DOS	Density of States
mfp	Mean Free Path
$\mathcal{D}$	Diffusion Coefficient
$U(t)$	Time Operator
$\mathrm{Tr}\{...\}$	Trace Operator
$G(\omega)$	Green's function
f	Distirbution Function
E	Energy
P	Probability
t	Time
L	Length
A	Cross Sectional Area
u	Displacement of Atoms
ψ_{rp}	Random Phase Vector
$a_n,\ b_n$	Lanczos Recursion Coefficients
a_k	Chebyshev Coefficients
T_k	k-th Chebyshev Polynomial
$J_k(x)$	k-th order Bessel Functions
$Y_l^m(r)$	Spherical Harmonics

LIST OF ABBREVIATIONS

ABBREVATION	EXPLANATION
3CGM	3-Coordinated, Geometring Modelling
3C	3-Coordinated
NC	Not Constrained
LAMMPS	Large-scale Atomic/Molecular Massively Parallel Simulator

CHAPTER 1

INTRODUCTION

Any material contains disorders above a specific temperature.[1] Even in crystalline materials, where atoms dwell in a repetitive, ordered pattern, irregularities are inevitable. The most common disorder in crystals is the thermal motion of atoms.[2] Besides, atoms can be displaced, substitutional or interstitial impurity atoms can be present, and points defects may form. Disorders can occur randomly, or they can be intentionally created in order to control the properties of materials since the existence of disorder gives rise to rich physics.[3–10] Apart from deviations from crystalline structure, atoms in a solid may dwell in a completely irregular, amorphous pattern.[11] These amorphous solids lack long-range translational order. Earlier, amorphous solids were thought of as crystals containing disorders.[12, 13] However, many amorphous solids do not even have a crystalline structure that is a counterpart. In 1932, Zachariasen worked on the forms of oxide glasses and concluded that the amorphous solids have continuous random networks. He asserted the fundamental discrepancy between a pristine and amorphous network is the absence of symmetry and long-range periodicity in the latter.[12] Apart from this, the bond character is the same, and the angles in Zachariasen's glasses slightly differ from those in crystals. Even though Zachariasen's work is an essential cornerstone in understanding amorphous solids' structural properties, different models continue to emerge, and an adequate scientific explanation of the amorphous form is still being investigated. [14–18]

Materials in which the wave equation of carriers is confined to at least one dimension are called low-dimensional materials. High-tech practical instances of low-dimensional systems are one-dimensional (1D) materials, such as nanotubes, nanowires, rods, and fibers; two-dimensional (2D) materials, graphene, layered insulators and semiconductors; and zero-dimensional materials(0D), quantum dots. Low-dimensional materials have emerged as favorable candidates for practical device ingredients due to the rapid development of nanoscience and nanotechnology. Low-dimensional materials mostly own this prominence to the quantum confinement effect and high surface area to volume. [19] The higher surface-to-volume ratio and ultra-shrink size provide more active sites than conventional bulk materials.[20–24] The quantum confinement of the carriers constitutively leads to a discrete spectrum. Low-dimensional materials provide parameters, such as size, to tune energy levels.[25] This property allows us to tune the properties

of low-dimensional materials.

Thermal conductivity is one of the principal characteristics of materials. So, we cannot design materials without regarding their thermal properties. In one condition, high thermal conductivity is desirable, while in another situation, low thermal conductivity is vital. Thermoelectrics is a typical example that requires materials with low thermal conductivity. On the other hand, electronic applications require materials with high heat conduction properties to remove excessive heat from devices. Fourier made the first quantitative description of thermal conductivity in the early 1800s. This definition states that the heat flux is inversely proportional to the temperature gradient, $\boldsymbol{J} = -\kappa \triangle T$.[26]. The proportionality constant, k, is called the thermal conductivity. However, Fourier's law is a relevant picture when diffusion dominates heat conduction. With the miniaturization of devices, the mean free path, the average distance traveled by carriers without collisions, has become comparable with devices' lengths, see Fig.1.1. As a result, carriers travel through devices without scattering, and the diffusion picture fails to describe the transport properties. Electrons are the dominant heat carriers in metals and conductors. Nonetheless, in dielectric solids, phonons, the quanta of collective atomic vibrations, are primary heat carriers. Below the temperature corresponding to the highest phonon mode energy, i.e., Debye temperature, materials manifest quantum effects.[27] The research on quantum thermal transport is of critical importance for the progress of state-of-art nanodevices that drastically differ from macroscopic devices.

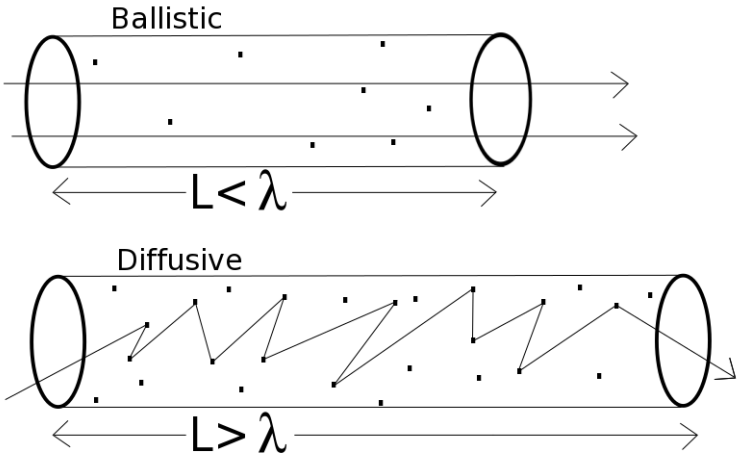

Figure 1.1. The illustration of carriers' propagation through a solid in the ballistic(upper) and diffusive(lower) transport regime. λ indicates the mean free path.

1.1. Quantum Thermal Transport

Classical particles obey the Maxwell-Boltzmann distribution. Bose-Einstein or Fermi-Dirac distributions govern the occupancy of quantum particles due to their spins; see Fig.1.2.[28] Particles with integer spins are called bosons, and particles with odd half-integral spins are called fermions. Fermions can not occupy the same state due to the Pauli exclusion principle, while more than one boson can occupy the same energy level. One of the boson statistics' primary conclusions is the disparency between the diamond's heat capacity at low and high temperatures. When the thermal energy is lower than the gap between the discrete vibrational spectrum, the quantum effects govern the heat capacity much lower than the Dulong-Petit prediction at low temperatures.[29–32]

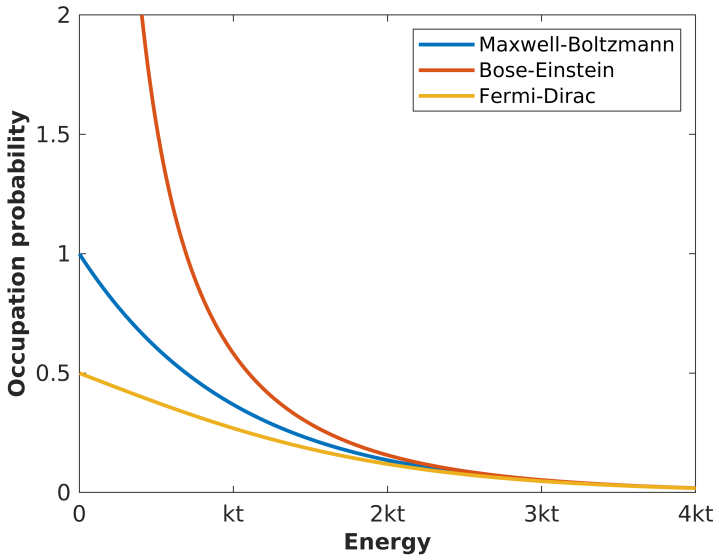

Figure 1.2. Comparision of Maxwell-Boltzmann, Bose-Einstein, and Fermi-Dirac distributions. Both quantum mechanical distributions become Maxwell-Boltzman at high temperatures, as they should be. Nevertheless, at low temperatures, there is a marked difference between them.

In the nanoscale, thermal transport occurs through discrete channels. Heat conduction, like electron conduction, is quantized when the mean free path of the carriers is equal to or longer than the length of the medium. Landauer-Buttiker formula describes the thermal flux as[33–35]

$$J_{th} = \sum_{m} \int_{0}^{\infty} d\omega \; \hbar\omega \; [f_{hot} - f_{cold}] \; \Xi_m(k) \tag{1.1}$$

where m is the mode index, Ξ_m reprensents transmission coefficient, $\omega_m(\boldsymbol{q})$ indicates the phonon dispersion relation, $f = [\exp(\hbar\omega_m/k_BT) - 1]^{-1}$ is Bose-Einstein distribution for the two(hot/cold) thermal reservoirs. The conductance is determined from the heat flux via

$$G_{th} = \frac{J_{th}}{\triangle T} = \frac{k_b^2}{h} \sum_m \int_{x_m}^{\infty} dx \frac{x^2 e^2}{(e^x - 1)^2} \Xi_m(x k_B T/\hbar) \tag{1.2}$$

where $x = hw(\boldsymbol{q})/k_bT$. In the limit, $\hbar\omega(\boldsymbol{q} = 0) = 0$, consider a one-dimensional ballistic system, where the four lowest lying modes, one longitudinal, two transverse, one torsional, make an appreciable contribution and if the interface between the reservoirs and the scattering field is perfect, i.e., the transmission coefficient is equal to one, the Eq.1.2 becomes

$$G_{th} = g_0 = \pi^2 k_B^2 T/(3h) \tag{1.3}$$

This value characterizes the maximum possible contribution of a single phonon channel. The quantization of the thermal conductance has been experimentally observed at room temperature in a gold single-atom junction[36] and at very low temperatures in suspended insulating nanostructures[37]. In the ballistic regime, the transmission coefficient equals the number of channels.

1.2. Phonon Tunneling

Tunneling, a characteristic behavior of waves, may occur when the wave propagates through different mediums. So, electromagnetic waves penetrate optic barriers just as water waves pass through a barrier in a ripple tank.[38] When a propagating wave encounters an interface, the second medium may transmit, refract, or totally reflect the incoming wave. The wave equation has decaying solutions with an imaginary wave vector for total reflection in the second medium region.[39] These evanescent solutions exponentially decay with the length. If a third medium is placed sufficiently close to the boundary between the first and second, the incoming wave can tunnel through the second medium via these evanescent waves.[38] Under wave-particle duality, quantum mechanical particles can also tunnel through an energy barrier.[40]

Phonons, the primary heat carriers in non-metallic (insulating or semiconducting) crystalline solids, propagate through vibrational waves. In some solids, a certain number of vibrational modes are forbidden; this opens a gap in their thermal spectrum, the so-called phononic gap or stopband. Consequently, the phonon propagation in such solids may display the tunneling phenomenon when the frequency of propagating phonon falls

inside the phononic gap. Several Molecular Dynamical studies have shown that phonon tunneling plays an essential role in tuning thermal conductivity behavior of periodic structures, nano-composites[41], superlattices[42–44], interface structures [45, 46], and layered (wander walls) structures[47].

Due to the artificial periodicity of superlattices, a stop band appears at the center and the boundary of the folded Brillouin zone. The experimental evidence for this occurrence was demonstrated by the use of the phonon spectroscopy technique in crystalline superlattices[48] and in amorphous superlattices[49]. Since the early experimental study of Narayanamurti, the forbidden phonon propagation mechanism has been investigated experimentally and theoretically. Mizuno and Tamura studied phonon resonant tunneling on single-[50], double-[51] and multiple-barrier[52] structures where barriers are made of periodic superlattices. They adopted the continuum model-based transfer matrix method and revealed the resonant transmission condition of acoustic phonons. Further, they discussed the tunneling times through single- and double-barrier structures.[53, 54]. They claim that since phonons' propagation occurs at the speed of sound, much slower than that of light, the measurement of tunneling time is expected to be easier.

Ridley elucidated that despite the absence of propagating vibrational modes, the polar optical modes can be transmitted through a rigid barrier layer in favor of long-range electric fields generated by themselves.[55] He used a macroscopic continuum model that simultaneously includes the mechanical and electrostatic boundary conditions. The model's scope has been widened to explain the phonon tunneling of optical nonpolar modes by Perez and Alvarez.[56] Additionally, they et al. are concerned with the times of phonon tunneling phenomenon.[57–60] Beside these, a particular amount of experimental and theoretical works have been made on tunneling through waveguides and phononic crystals.[61–67] These studies can be exemplary of acoustic phonon tunneling. A few experimental measurements from them assert that tunneling of phonons occurs at supersonic speed. Despite the considerable work on tunneling and its times, there are still open questions.

The nanobridge structure is a typical structure widely used in molecular electronics, nanophononics, nanomechanics, and optoelectronics.[68–73] With the novel experimental techniques, it is now possible to measure the thermal conductance of a single molecule in favor of this structure.[74] In this study, we propose a phonon tunneling device that could enable observation of the phonon tunneling phenomenon through a general bridge set-up based on advances in nano-scale heat transfer measurements. The device consists of a thermal dichromator, a medium with a phononic gap at the frequency of inter-

est, and two macroscopic reservoirs. The thermal dichromator is instead of a monochromator since acoustic phonons are hard to scatter and barely affected by atomic details. So, we can not open a gap in the low-frequency range. As a result, the dichromator only allows the propagation of low-frequency phonons and a portion of phonons with frequencies that coincide with the phononic gap. The phononic gap system acts as a barrier to selected phonons. Transmission characteristics of the structure are revealed based on Green's Functions Method, which, in phonon tunneling research, was used only to verify the resonance condition in Mizuno's work to the best of the author's knowledge.[51]

1.3. Thermal Transport in Amorphous Materials

The mechanism that underlies amorphous materials' thermal conductivity is distinctively different from ordered solids.[75, 76] Fig.1.3 demonstrates the thermal conductivity of both ordered and amorphous phases of silicon. The amorphous silicon phase has a much lower thermal conductivity than the crystalline phase. A significant drop is noticeable in the low-temperature range compared with crystalline thermal conductivity. The thermal conductivity of ordered solids increases with temperature at low temperatures but decreases at high temperatures due to the phonon-phonon scatterings, the solid line in Fig.1.3. However, the amorphous silicon's thermal conductivity shows a peculiar relationship with temperature. At low temperatures, amorphous conductivity increases with temperature, as in crystals. A plateau region appears at medium temperatures; within this region, the conductivity is independent of the temperature. Then, with the increasing temperature, the amorphous conductivity increases again until it saturates a finite value. The strange temperature dependence is also recognized in a few noncrystalline dielectric solids, such as B_2O_3, SiO_2, and As_2S_3.[77] As well known, phonons are responsible for thermal transport in perfectly ordered semiconductors or insulators. They are delocalized carriers and have plane-wave-like character. Nevertheless, the concept of phonons is irrelevant due to the absence of long-range periodicity of amorphous solids. Scientists have made several attempts to explain the physical mechanism underlying the thermal transport of amorphous solids.

Slack established the minimum thermal conductivity model in 1979.[78] He assumed that the mean free paths of oscillators are equal to the phonon's wavelength. In 1989, Cahill advanced the minimum thermal conductivity model by equating the mean free paths to half the Debye wavelength.[79] The thermal conductivity is expressed within the minimum thermal conductivity model with this advance as

$$\kappa_{min} = \left(\frac{\pi}{6}\right)^{\frac{1}{3}} k_b n^{\frac{2}{3}} \sum_i v_i \left(\frac{T}{\Theta_D}\right)^2 \int_0^{\Theta_D/T} \frac{x^2 e^x}{(e^x - 1)^2} dx \tag{1.4}$$

where n is the number density of atoms, v_i is the speed of sound, and Θ_D is the Debye frequency. With Cahill's contribution to this method, the model successfully predicted the thermal transport properties of many amorphous solids.[80]. Later, Agne developed the diffusion minimum thermal conductivity model, an efficient model in diffusional transport regimes.[81] Besides these, Molecular Dynamics is a widely adopted tool to predict amorphous solids' thermal transport properties.[82]

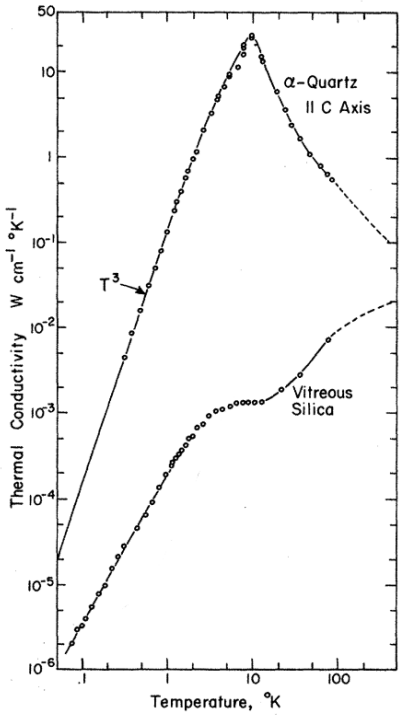

Figure 1.3. The thermal conductivity of crystalline, and fused quartz. Reprinted figure with permission from Ref.[76]. Copyright 1971, American Physical Society.

Even though some of these existing models reasonably predict the thermal conductivity of amorphous materials, more is needed to explain the strange three-stage relationship of amorphous conductivity with temperature. In 1993, Allen and Feldman proposed a theoretical model based on supercell lattice dynamics to explain the reason behind this strange dependence.[83, 84] According to heat carriers' characteristics of amorphous phases, they divided the vibrational modes into three classifications: locons, propagons, and diffusons.[85]

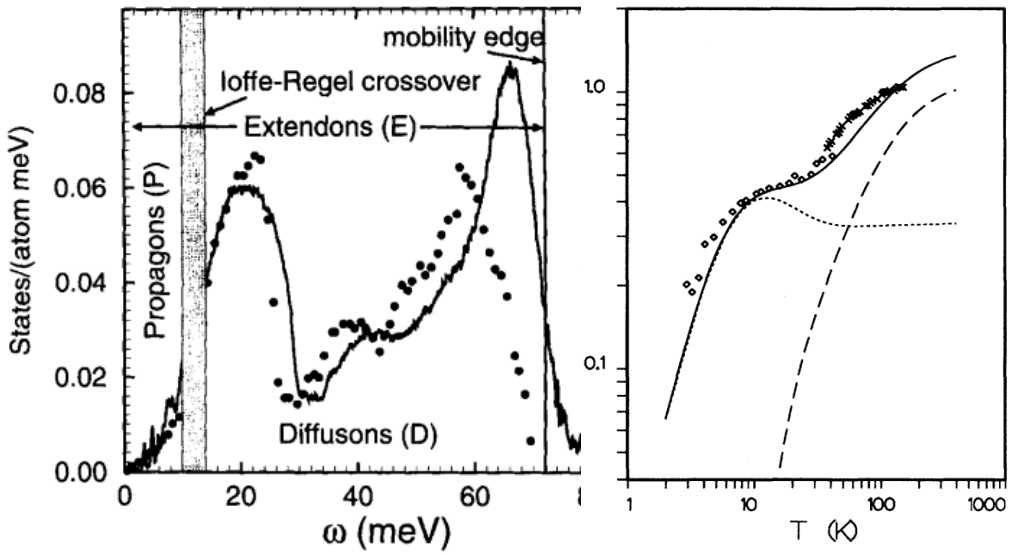

Figure 1.4. The density of vibrational states of amorphous silicon(left). Reprinted figure with permission from Ref[85]. Copyright 1999, Taylor and Francis. The thermal conductivity of vitreous silica(right). The dashed lines show the individual contributions of different carriers. Reprinted figure with permission from Ref[84]. Copyright 1993, American Physical Society.

Locons are highly localized carriers and have a negligible contribution to transport. Both diffusons and propagons are extendons as opposed to locons. Propagons are also delocalized and have common characteristics with phonons. They have long wavelengths and a well-defined wavevector like phonons. Diffusons are also delocalized carriers, but they are non-propagating. Their transport profile is diffusive. The left panel of Fig.1.4 demonstrates the density of vibrational states of amorphous silica. The boundary between locons and extendons is known as "mobility edge". The frontier zone between the diffusons and propagons is named "Ioffe-Regel crossover" by Allen and Feldman. The whole vibrational spectrum consists mainly of diffusons.

The right panel of Fig.1.4 demonstrates the contribution of different vibrational modes to the conductivity of amorphous silica. Propagons are the dominant carrier at the low-temperature range, and the relationship of conductivity with temperature is quadratic. The individual contribution from propagons is shown with the dotted line in the right panel Fig.1.4. Propagons significantly contribute to conductivity since their profile is similar to the phonons, and their mean free path is more extended than diffusions and locons. Propagons are scattered by inelastic processes like phonons, causing a fall in the contribution from propagons above $T \approx 10K$, which evolves the plateau. Then, with the

rising temperature, diffusons start to contribute, and the rise with temperature continues until a saturated value is reached. The dashed line in the right panel Fig.1.4. shows the individual contribution from the diffusons.

Locons do not contribute to the conductivity due to the robust localization, and diffusons are not as efficient carriers as phonons; consequently, amorphous solids demonstrate much lower thermal conductivity than ordered solids. Owing to low thermal conduction, amorphous solids are promising candidates for thermal barrier coatings, thermal protection, and thermoelectric applications. Although this work by Allen and Feldman has opened a critical perspective into our understanding of the thermal conductivity of amorphous solids, there are still controversial topics.[86] How these heat carriers interact with other particles, like electrons, is a fascinating debate and can lead to room-temperature superconductors.[86] Moreover, the distinction between propagons and diffusons has only been made qualitatively. What exactly distinguishes these carriers? Lastly, whether the peculiar temperature dependence is observed in all amorphous solids, especially in two-dimensional amorphous solids, is a critical question of the literature.[87]

Moreover, the specific heat also demonstrates distinct behavior in amorphous solids at low temperatures.[88] In this range, amorphous solids have higher specific heat than their crystalline counterparts.[76] Further, the density of states of amorphous solids does not involve a Van Hove singularity. The absence of translational symmetry broadens it.[75]

1.4. Two-dimensional amorphous materials

Lately, the research on two-dimensional materials has attracted much attention from fundamental and practical applications.[89–92] The atomic thickness and novel layered structure make two-dimensional materials manifest several distinguished optical and electrical properties from their bulk counterparts. Existing studies have primarily focused on two-dimensional crystalline materials.[14] Still, amorphous two-dimensional materials draw expanding attention since they have shown tremendous potential for applications in diverse fields. Bulk amorphous materials have widely been employed in many applications, and exploring their low-dimensional versions would be technologically beneficial.[17, 93] Indeed, two-dimensional, amorphous materials integrate the advantages of both amorphous and two-dimensional morphology.[94] The novel, highly disordered structure, high-quality large-area uniformity, and nominal fabrication expenditure make them fundamental ingredients of numerous practical applications, including

catalysis reactions, energy storage, and electronic and optoelectronic applications.[95–98]

Two-dimensional materials are distinctly different from their bulk parts concerning the confinement of electrons in two dimensions, strong in-plane covalent bonds, unconventional atomic thickness, and high specific surface area.[89, 99, 100] Amorphous structures have more reactive sites due to many defect sites and more exposed atoms.[93, 94] Consequently, two-dimensional, amorphous materials are excellent nominees for catalysis reactions due to more active sites and high surface area. Besides, the ultrathin thickness of two-dimensional structures can shrink the transportation length, and amorphous structures could supply additional paths to carriers.[94, 98, 101] Therefore, fast transportation of ions/electrons might occur in amorphous two-dimensional structures. On the other hand, because of high disorder, the propagation of waves can be restricted in amorphous media; hence, carriers can be localized.[84, 87] Localization of carriers leads to low conductivity; as a result, they can be used as barriers or insulators.

Moreover, it is recognized that their defects and impurities regulate amorphous materials' electronic and thermal properties.[102, 103] This property allows us to tune the properties of two-dimensional, amorphous materials. The synthesis of amorphous two-dimensional materials such as metal oxide, metal hydroxide, metal chalcogenides, alloy, silicates, amorphous graphene, amorphous MoS_2, amorphous BN, and amorphous BP has already been accomplished, and amorphous structures can be produced at a comparably low temperature.[101, 104–111] The amorphous two-dimensional materials' application field is still limited compared to crystalline counterparts, although their excellent catalysis performance, energy storage, and mechanics have been demonstrated. The most practical approach is synthesizing more two-dimensional, amorphous structures with unique properties and functions to expand their applications.

1.4.1. Amorphous graphene

The carbon atom is capable of generating distinctive structures owing to its valency. Carbon-based materials have extreme stiffness and high mechanical strength, and hence, they show excellent thermal transport properties. Its two-dimensional honeycomb lattice, graphene, was first exfoliated in 2004.[112] Since then, the fabrication and characterization of graphene have attracted much attention due to its unique properties.[99, 113–115] It has been shown that graphene fits from aerospace applications to nanoelectronics.[116, 117] For instance, graphene is a promising candidate for flexible electronics, which can dramatically change our lives.[118, 119] Wearable electronics have been advanced

based on flexible electronics, primarily for health care.[120] In the future, clothes can constantly check human health by monitoring blood pressure, temperature, breath, and heart rates.

Researchers have mainly focused on graphene crystal growth, but large-sized fabrication of graphene has polycrystalline morphology. To understand the macroscopic properties of graphene, one must reveal the consequences of the polycrystalline structure, such as grain size distribution.[121] Also, it has been shown that polycrystalline graphene fits a class of applications, from spintronic instruments to wearable-flexible electronics to biosensors. Furthermore, Kotakoski et al. experimentally achieved an amorphous graphene structure from graphene irradiated with electron beams.[122] They demonstrated the process step by step by nucleation and growth of rotated hexagons and polygons. Also, they performed density functional theory calculations to show how defects migrate and gather together. In 2012, a theoretical study predicted an amorphous graphene structure using geometrical modeling and molecular dynamics.[16] The output structures have a continuous random network. So they are Zacheriasen glasses. Recently, an experimental work showed that laser-assisted chemical vapor deposition directly synthesizes monolayer amorphous graphene.[17] The advantage of this growth method over the former methods is the capacity to produce a larger size. The same team also performed Monte-Carlo calculations to construct monolayer amorphous carbon. The work showed that amorphous monolayer carbon is not a Zacheriasen glass due to the presence of crystalline carbon islands. Nevertheless, all agree that amorphous graphene lacks long-range periodicity. The concept of unit cell and lattice is unuseful due to the absence of translational symmetry.

Amorphous graphene is a potential candidate for transparent electronic applications since it demonstrates transparent behavior in the wavelength range from 200 nm to 1000 nm.[123] Due to the high surface area and dielectric strength, amorphous graphene can be used in transformer oil nanofluids applications.[124] Besides, fabricating Zachariasen continuous monolayer into a field-effect transistor increases the resistance two orders of magnitude than that of ordered counterparts.[125] A hybrid system that contains amorphous graphene can enhance field emitter properties because amorphous graphene demonstrates satisfying field emitter performance. Also, owing to flexibility, amorphous graphene can be utilized in flexible electronics applications.

For almost all applications, one of the essential properties of substances is thermal conductivity. Many scientists have widely studied the thermal conductivity of crystalline graphene. However, research on the thermal properties of the amorphous phase lagged

behind the research on the crystalline phase, so there are still open questions. By now, molecular dynamic calculations have been performed to reveal the thermal transport properties of amorphous graphene.[87, 126, 127] Molecular dynamics is a widely accepted method to study the thermal properties of materials, but it is based on Newtonian mechanics; consequently, it does not include the quantum effects intrinsically. Hence, the literature lacks the thermal transport properties of amorphous graphene at a low-temperature range, and the quantum mechanical effects on the thermal transport of the amorphous graphene remain unknown. We expect these effects on amorphous graphene's transport properties to be significant since the material's corresponding crystalline phase has a high Debye temperature.

All existing studies on the thermal conductivity of amorphous monolayer carbon phase agree that amorphous graphene has lower thermal conductivity than crystalline graphene. Mortazavi et al. demonstrated that the thermal conductivity of amorphous carbon monolayer could be two orders of magnitude lower than its pristine form.[128] They considered periodic boundary conditions in their equilibrium molecular dynamics simulation. Zhu and Ertekin performed the generalized Debye/Peierls and Allen/Feldman approach besides molecular dynamics simulations to reveal the contributions of vibrational states to thermal transport.[87] They concluded that diffusons contributions to the transport are negligible, and propagons dominate the transport. They did not observe a plateau region in their temperature dependence of thermal conductivity, but their study lacks low-temperature calculations. Bazrafshan and Rajabpour presented non-equilibrium molecular dynamics calculations for structures with various defect concentrations (up to 54%) and under different tensile strains (up to 0.12).[127] They showed that just 1% defect concentration can develop a 27% decrease of the thermal conductivity. Antidormi et al. analyzed the vibrational modes of amorphous graphene and the effect of the degree of amorphousness, demonstrating how the samples' progressing loss of crystallinity leads.[126] They characterized the degree of amorphousness by computing the triatic order parameter, q_3, which shall be explained in the method section. This parameter effectively captures the deviation from the ideal sp^2-hybridized crystalline structure. Their thermal conductivity computations have been achieved within the Green-Kubo modal analysis, and the results showed a substantial enhancement of thermal conductivity as a function of the triatic order, displaying how amorphousness effectively suppresses thermal transport. Nevertheless, none of these studies demonstrated the quantum effects on amorphous graphene thermal transport properties and lack of low-temperature calculations. The lowest temperature is 200 K in the calculations.

This dissertation is organized as follows: Chapter 2 explains the methods for generating amorphous graphene structures and determining thermal properties. Chapter 3 presents the phonon tunneling device. Chapter 4 focuses on the quantum thermal transport properties of two-dimensional amorphous carbon monolayers. Chapter 5 is the conclusion.

CHAPTER 2

METHODS

2.1. Amorphous graphene structure

There are several theoretical models to generate an amorphous graphene structure. One of the amorphous graphene producing procedures involves Molecular Dynamics.[16] Melting crystalline graphene supercells produces two-dimensional liquid configurations. Cooling the liquid systems by removing kinetic energy generates amorphous graphene. Another method based on Molecular Dynamics is the liquid quench method, a reactive molecular dynamics study.[129] In this method, the process starts with a simulation cell with N carbon atoms placed randomly. Then, the simulation cell is ramped temperature to 10000 K and equilibrated at that temperature like approximately 15 ps. Following this, the cell is quenched to 3000 K to the cell. After annealing at 3000 K for annealing time, t_a, the cell is quenched to 300 K and equilibrated.

The kinetic Monte-Carlo method is the primary method used in this work to generate amorphous graphene structures lacking periodicity.[16, 17] As mentioned in the introduction, there is still debate on amorphous structures.[130] So, we decided to study both the Zachariasen and nanocrystallite phases of the two-dimensional, amorphous carbon phase. Three different kinds of amorphous graphene structures can be gained with two akin kinetic Monte-Carlo algorithms. One starts with the crystal structure and amorphize it, while the other begins with a random network and crystallizes the beginning structure. Common to both algorithms, each iteration rotates a randomly chosen carbon-carbon bond from the device region by 90°. Energies before and after the rotation are determined. All energy calculations have been performed with the LAMMPS package.[131] Adaptive Intermolecular Reactive Empirical Bond Order (AIREBO) potential parameters for hydrocarbons are adapted to describe interatomic forces. During energy calculations, structures and the cell are relaxed with the conjugate-gradient algorithm until all forces fall below $0.1\ eV/$Å, and the relaxation of the simulation cell is allowed. Periodic boundary conditions are implemented in all directions, but the simulation cell is long enough to hinder the layers' interactions in the transverse direction. The Metropolis acceptance

criterion specifies the acceptance of bond transposition.

$$P = \min[1, \exp[(E_i - E_f)/k_bT]] \tag{2.1}$$

where E_i and E_f are the former and later energies of the system. According to the final and initial energy, the upcoming structure shall be accepted or not. Whether the algorithm accepts the new system depends on the network we start with. So, the acceptance conditions are unique to each algorithm.

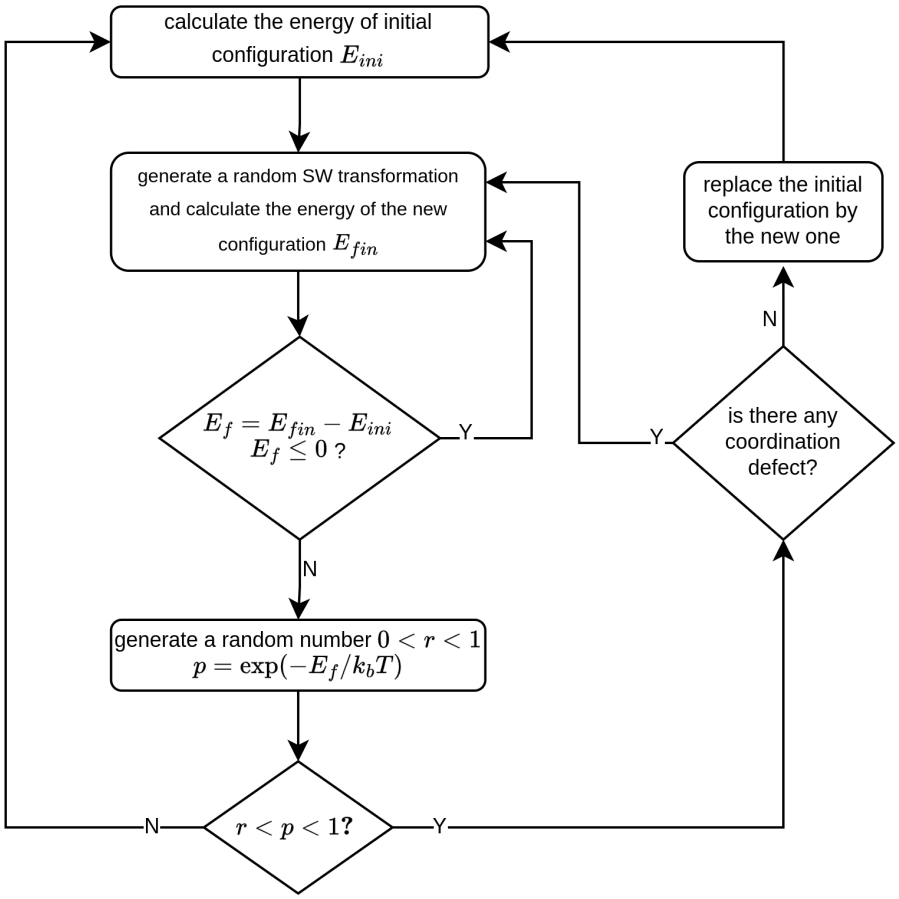

Figure 2.1. Theflowchart of amorphization algorithm.

The amorphization procedure starts with a crystalline graphene supercell. Subsequently, the algorithm rotates a randomly picked bind carbon-carbon pair by 90 degrees, i.e., creates a Stone-Wales defect within the area under interest. The structures and the cell are relaxed, and the energies are calculated as described. To amorphize the beginning structure, we reject the upcoming structures in which bond rotation lowers the energy, i.e.,

$E_f < E_i$. If not, the Metropolis acceptance probability is calculated, and a random number between zero and one is generated; the temperature is kept high enough so that the probability shall be high enough to accept half of the upcoming configurations in which the bond rotation augmented the energy. If the probability is greater than the randomly generated number, r, but lower than one, it is checked whether the structure contains a coordination defect. If the following configuration has any coordination defect, our amorphization algorithm denies it. The flowchart of the amorphization algorithm is shown in Fig.2.1.

With the amorphization algorithm, two different kinds of single-layer amorphous carbon phases are generated. Our first amorphous graphene configuration type is similar to Kumar's configuration obtained by geometric modeling in 2012.[16] Since the most crucial feature of Kumar's structure is that it does not contain any coordination defects, we put the condition that the upcoming configuration can not contain coordination defects in the acceptance cases. We allow each atom to have three atoms around 2.1 Å; thus, each atom is threefold coordinated. The resultant structure is similar to the Zachariasen glasses since it has a continuous random network and mainly consists of five-, six-, and eight-membered carbon rings, as shown in the left panel of Fig.2.2. We named this type of structure the 3CGM type.

For the second type of structure, the acceptance condition has one difference. Now, we let each atom have three neighboring atoms around 2 Å. The difference between the previous and this types of structures is that while the second can consist of three- and four-ring members, the first can not. Again, all atoms are three-coordinated, and this structure type is also equivalent to Zachariasen's glasses. The middle panel of Fig.2.2 displays a piece from this device type named type.

For the crystallization procedure, we use Zhuang's algorithm, which accepts all the upcoming configurations in which bond rotation lowers the energy.[132] The procedure begins with a supercell consisting of randomly placed carbon atoms with the same density as crystalline graphene. The system is subsequently relaxed, adopting a conjugate gradient algorithm. The simulation cell is not relaxed at the algorithm's early steps since the completely random configurations tend to disperse due to a lack of order. Then, the bond-switching process applies to a randomly chosen carbon-carbon bond. The initial and final energies are determined as we described previously. The next step is calculating the Metropolis acceptance probability and generating a random number between zero and one. The temperature was set at 6000 K. If the Metropolis probability is higher than the randomly generated number, r, the upcoming configuration is accepted. The flowchart

and a detailed description of this algorithm can be seen in Ref.[132]. This last configuration type is significantly different from the two others, and it is not Zazhariasen glasses since it still has some crystalline phases; indeed, its structure is similar to the crystallite model in which crystalline carbon islands still remain in amorphous media. Also, resultant structures may have coordination defects, voids, and three- and four-membered rings. We named this structure NC type. The right panel of Fig.2.2 shows a fragment from this type of configuration. All three-type structures have out-of-plane buckling due to internal distortions.

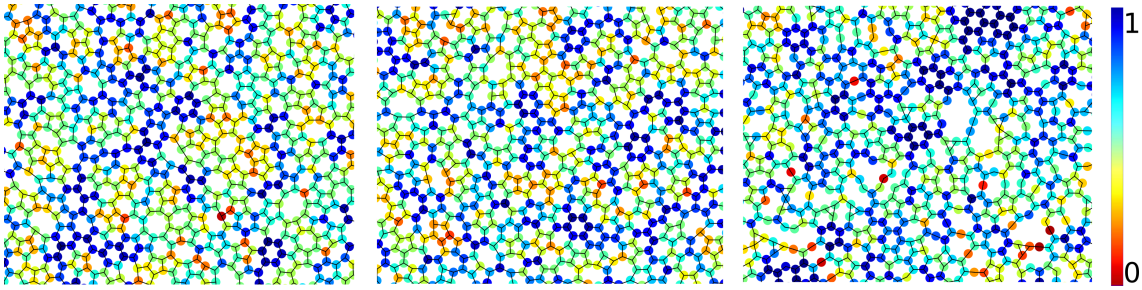

Figure 2.2. The piece from the structures for the exhibition of the difference between device types. The left, middle, and right are 3CGM, 3C, and NC device types. Color map representing the q3 parameter value.

The last thing required to be introduced is the triatic order parameter, which quantitatively identifies the degree of amorphousness and effectively captures the deviation from the ideal hexagonal pristine graphene structure.[126, 133, 134] The amorphousness of structures is quantified with the local bond order parameter, which quantifies the structural symmetry around a particle, i, and is defined as

$$q_{lm} = \frac{1}{N_b(i)} \sum_{j=1}^{N_b(i)} Y_{lm}(\boldsymbol{r}_{ij}) \tag{2.2}$$

where $N_b(i)$ is the number of first neighbors around particle i, i.e., number of atoms of the ith atom around 2.3 Å(the second pick of the radial distribution function of perfect graphene), and $Y_l^m(\boldsymbol{r}_{ij})$ is the spherical harmonics of the vector from ith atom to jth atom. l is an integer within the range $-l \leq m \leq l$. Since for sp^2-hybrization, $l = 3$, the local bond order parameter becomes the triatic order parameter

The individual local bond order parameter for each atom is calculated as

$$\tilde{q}_l(i) = \frac{1}{N_b(i)} \sum_{j \epsilon N_b(i)} \boldsymbol{q}_l(i) \cdot \boldsymbol{q}_l(j) \tag{2.3}$$

$$= \frac{1}{N_b(i)} \sum_{j \epsilon N_b(i)} \sum_{m=-3}^{m=3} \frac{q_{l3}(i)}{\sqrt{\sum_{m=-3}^{m=3} |q_{3m}(i)|^2}} \cdot \frac{q^*_{l3}(j)}{\sqrt{\sum_{m=-3}^{m=3} |q_{3m}(j)|^2}} \tag{2.4}$$

The system's order parameter is determined by averaging the $\tilde{q}_l(i)$ values. The q3 parameter takes a value between zero and one and is one for perfect crystals. For ideal pristine graphene, $q_3 = 1$. In other words, lesser q_3 means more disordered graphene structure. For a detailed explanation of the local bond order parameter, see [135].

All the local bond order parameters are determined after the uttermost relaxation with optimized Tersoff potential parameters, as described in the upcoming section. In Fig.2.2, each colored circle stands for one carbon atom, and its color indicates the q3 parameter value. Fragments shown in Fig.2.2 were selected from configurations with the same q3 parameter. For the atoms that belong to three- and four-membered rings or have coordination defects, the q3 parameter is close to zero due to high asymmetry.

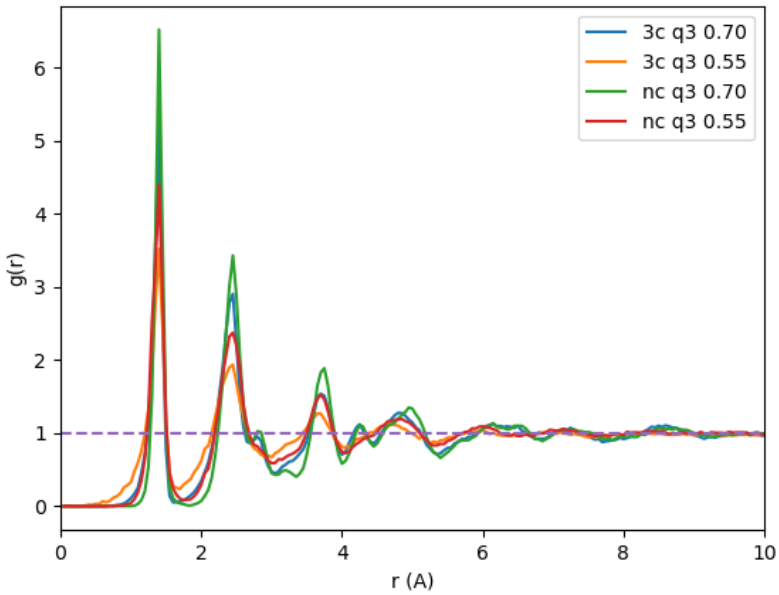

Figure 2.3. The radial distribution function, which is calculated with Ref.[136]

We have plotted the radial distribution function, which provides information about the internal structure, in Fig.2.3. The radial distribution function is discrete at T=0 K in crystalline structures due to the high symmetry. Nonetheless, in networks where the long-range order is missing, the peaks are broadened due to variations in the bond lengths and vanish after a few angstroms. In our structures, the peaks are broadened, indicating the absence of long-range order. The first peak came in around 1.42, as in crystals, but unlike crystals, it was broadened. Peaks start to vanish at distances greater than four angstroms because of randomness in structures. The highest peaks came in the NC configuration with q3=0.70 structure because the NC structures are nanocrystalline and still contain crystalline islands. Nevertheless, the 3C configurations showed a lower maximum, while they were more broadened because they are Zachariasen glasses, which have a continuous random structure, but all atoms are three coordinated.

2.2. Dynamical Matrices

The primary input for our methods is the dynamical matrices obtained with the simulation package based on the finite difference method. Before obtaining dynamical matrices, configurations are finally relaxed with the conjugate gradient algorithm and a force tolerance by $10^{-3}eV/\text{Å}$. We apply periodic boundary conditions in each direction, and the simulation cell length in the transverse direction is 50 Å to prevent interaction between layers. We used optimized Tersoff empirical potential parameters extending the original Tersoff potential to describe interactions.[137–139] Tersoff's potential parameters set provides a more robust fit to experimental graphene phonon dispersion with this extension.

Thus, the most widely used many-body potential parameters for the thermal properties of carbon-based structures are the optimized Tersoff potential parameters.[141–173] To validate our calculations, we reproduce the dispersion shown in the top panel of Fig.2.4. Blue triangles represent the measured values adapted from the Ref.[140]. The reactive empirical bond order(REBO) potential, parametrized for C-H-O systems, is used during the Monte Carlo algorithm. Even though the optimized Tersoff potential parameters are most appropriate for studying the thermal behavior of carbon-based materials, they are insufficient to build an amorphous carbon configuration, especially for the crystallization procedure; it created long carbon chains instead. To compare the Rebo-CHO parameters with optimized Tersoff potential parameters, we also determine the phonon dispersion relation(the bottom panel of Fig.2.4), which agrees with the

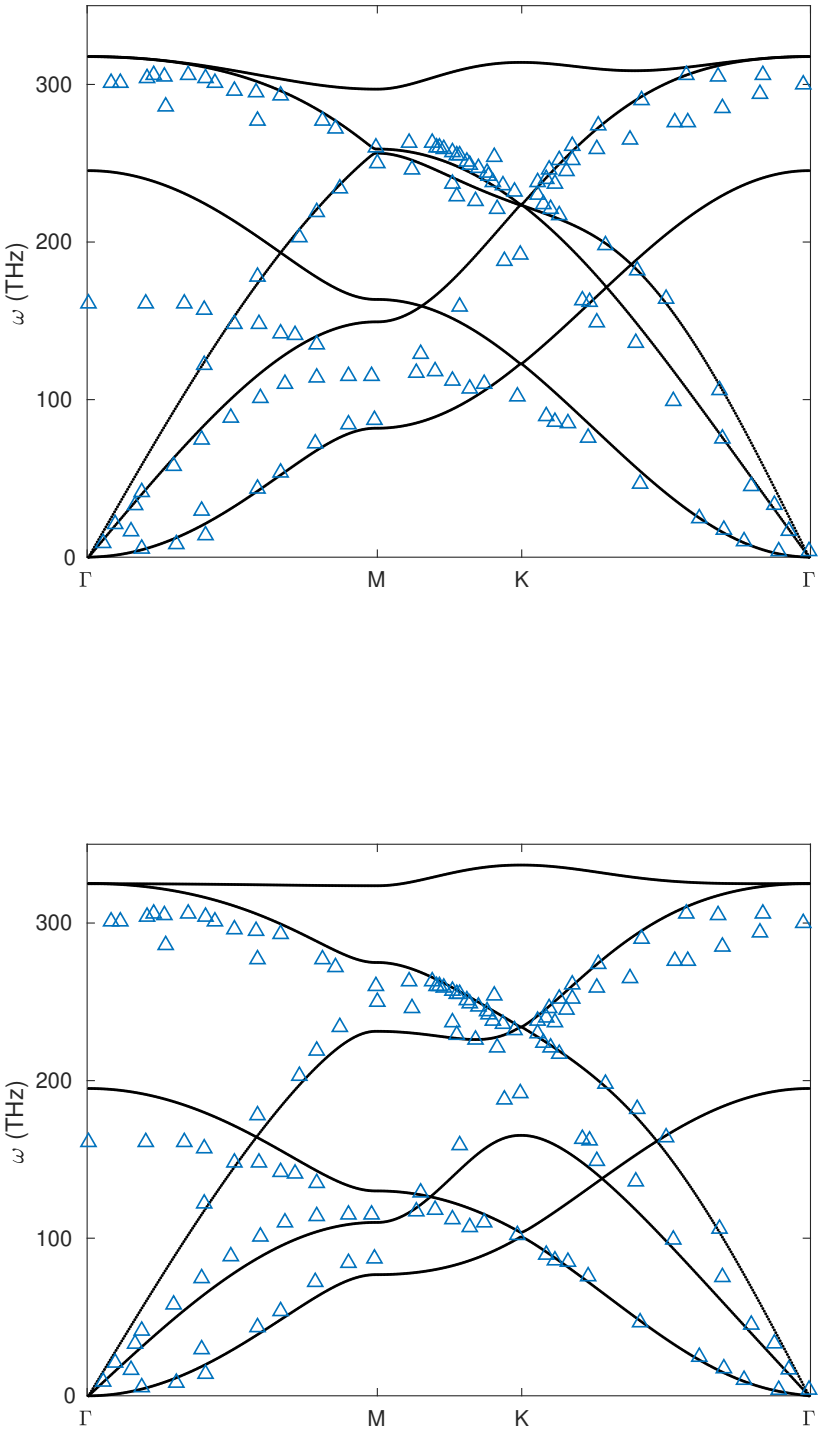

Figure 2.4. Phonon Dispersion relations. Blue triangles represent the measured values adapted from the Ref.[140]. The phonon dispersion relation of graphene was determined with optimized Tersoff potential(top panel) and optimized Rebo-CH potential(bottom panel).

previous calculations.[174, 175] The optimized Tersoff potential parameters capture the graphene's optic phonon modes better than Rebo-CHO potential parameters.

The equation for the dynamical matrix as an output of LAMMPS is following.

$$D = \frac{\Phi_{\alpha\beta}^{kk'}}{\sqrt{m_k m_k'}} \tag{2.5}$$

where m_k indicates the mass of the kth atom; Φ representes the force constant matrix and defined as within the harmonic approximation[88]

$$\Phi_{\alpha\beta}^{kk'} = \frac{\partial^2 U}{\partial u_{k,\alpha} \partial u_{k',\beta}} \tag{2.6}$$

where U represents the interatomic potential energy and u is deviation of atomic coordinates from the equilibrium positions. The $\boldsymbol{q}$-dependent dynamical matrix is

$$D(\boldsymbol{q}) = \frac{1}{\sqrt{m_k m_k'}} \sum_{l'} \Phi_{\alpha\beta}^{0_k, l_k'} e^{i\boldsymbol{q}\cdot\boldsymbol{R}_l'} \tag{2.7}$$

where α and β are Cartesian components, l_k' stands for the kth atom of lth unit cell, $\boldsymbol{R}_l$ is the lattice vector of the lth unit cell. Dispersions are obtained by lattice dynamical calculations. The square root of eigenvalues of the $\boldsymbol{q}$-dependent dynamical matrix gives the dispersion, $\omega(\boldsymbol{q})$.

2.3. Landauer Method and Green's Functions

Green's function technique is an efficient theoretical approach to determine transport properties of nanostructures.[176, 177]. The method enables the determination of the transport properties of complex nanostructures, which can have boundaries, interfaces, scattering regions, and defects. The system must be divided into three fields: scattering region, left and right reservoirs to apply Green's functions. The reservoirs are two semi-infinite crystal lattices, while the scattering region has an arbitrary finite structure. The first step of the formalism is to compute the Green's functions of bulk left- and right-reservoirs. The definition of the Green's function is

$$G(\omega) = \left((\omega^2 + i\eta)\mathbb{1} - D\right)^{-1} \tag{2.8}$$

where D is the dynamical matrix directly constructed from the force constants and masses, and η is a sufficiently small number. Due to the partitioning scheme, the dynamical matrix

becomes

$$D = \begin{pmatrix} D_l & D_{ld} & 0 \\ D_{dl} & D_d & D_{dr} \\ 0 & D_{rd} & D_r \end{pmatrix} \tag{2.9}$$

where $D_{ld} = D_{dl}^{\dagger}$, and $D_{rd} = D_{dr}^{\dagger}$. Here, $l(r)$ and d represent the left(right) reservoir and scattering(device) region, respectively.

$$\begin{pmatrix} (\omega^2 + i\eta)\mathbb{1} - D_l & -D_{ld} & 0 \\ -D_{dl} & (\omega^2 + i\eta)\mathbb{1} - D_d & -D_{dr} \\ 0 & -D_{rd} & (\omega^2 + i\eta)\mathbb{1} - D_r \end{pmatrix}$$

$$\times \begin{pmatrix} G_l(\omega) & G_{ld}(\omega) & G_{lr}(\omega) \\ G_{dl}(\omega) & G_d(\omega) & G_{dr}(\omega) \\ G_{rl}(\omega) & G_{rd}(\omega) & G_r(\omega) \end{pmatrix} = \mathbb{1}$$

If we only consider the product with the 2nd column of the matrix of Green's functions

$$G_l^{-1}(\omega)G_{ld}(\omega) - D_{ld}G_d(\omega) = 0 \tag{2.10}$$

$$-D_{dl}G_{ld}(\omega) + \big((\omega^2 + i\eta)\mathbb{1} - D_d\big)G_d(\omega) - D_{dr}G_{rd}(\omega) = 1 \tag{2.11}$$

$$-D_{rd}G_d(\omega) + G_r^{-1}(\omega)G_{rd}(\omega) = 0 \tag{2.12}$$

where $G_{l(r)}^{-1}(\omega) = \big((\omega^2 + i\eta)\mathbb{1} - D_{l(r)}\big)$. Rearranging Eq.2.10 gives

$$G_{ld}(\omega) = G_l(\omega)D_{ld}G_d(\omega) \tag{2.13}$$

. And, similarly Eq.2.12 becomes $G_{rd}(\omega) = G_r(\omega)D_{rd}G_d(\omega)$. Substituing into Eq.2.11

$$\big((\omega^2 + i\eta)\mathbb{1} - D_d\big) - D_{dl}G_l(\omega)D_{ld} - D_{dr}G_r(\omega)D_{rc}\big)G_d(\omega) = 1 \tag{2.14}$$

Now we can define self-energies, which measures the interactions between the scattering region and each reservoir

$$\Sigma_{l(r)}(\omega) = D_{dl(dr)}G_{l(r)}(\omega)D_{ld(rd)} \tag{2.15}$$

After taking into account the interactions, the Green's function of the scattering region, Eq.2.14, becomes

$$G_d(\omega) = \left[\left((\omega^2 + i\eta)\mathbb{1} - D_d\right) - \Sigma_l - \Sigma_r\right]^{-1} \tag{2.16}$$

Finally, phonon transmission is calculated by

$$\Xi(\omega) \;=\; \mathrm{Tr}\left[\Gamma_l G_d(\omega)\Gamma_r G_d^{\dagger}(\omega)\right] \tag{2.17}$$

where the broadening function is $\Gamma_{l(r)} = -2\mathrm{Im}(\Sigma_{l(r)})$. Assuming that $\Delta T \to 0$, namely equilibrium transport, conductance is defined as we defined in the introduction chapter

$$G = \frac{J}{\Delta T} \;=\; \frac{1}{2\pi}\int d\omega\; \hbar\omega\; \Xi(\omega)\; \frac{\partial f}{\partial T} \tag{2.18}$$

where f is the distribution function, we calculated thermal conductivities with two different distribution functions: Bose-Einstein and Maxwell-Boltzman distributions. All other parts of the method apply to both mechanics. The transmission function obtained by Green's functions method remains the same for both quantum and classical mechanics in the harmonic limit. Only the distribution function makes the difference here. Thus, we can only see the effect of phonon occupancy factors on thermal conduction, independent of all other parameters.

To obtain the Maxwell-Boltzman distribution function, consider a solid consisting of harmonic oscillators, which have a range of frequencies, $g(\epsilon)$. Assume there is no quantization, i.e., $E(\eta, \epsilon) = \eta\,\epsilon$, where η is not restricted to having discrete integer values, but it is continuous. Then, the single-particle partition function is

$$Z = \int d\epsilon\; g(\epsilon) \int d\eta\; e^{-\beta\,\epsilon\,\eta} = \frac{1}{\beta}\int d\epsilon\; g(\epsilon)\; \epsilon \tag{2.19}$$

We know the density of states, $\int d\epsilon\; g(\epsilon)\; \epsilon$, is equal to a finite value; let us say I. Then, the partition function becomes

$$Z = \frac{1}{\beta} I \tag{2.20}$$

Hence, the average energy is $U = -\frac{1}{Z}\frac{\partial Z}{\partial \beta} = k_B T$. For a solid with N independent atoms $Z_{3D} = Z^{3N}$, so $U = 3Nk_BT$. One can rewrite the energy as

$$U = \int d\epsilon \; g(\epsilon) \; \epsilon f(\beta, \epsilon) \tag{2.21}$$

Remember quantum mechanically, $f_{be}(\beta, \omega) = 1/(e^{\beta\hbar\omega} - 1)$. Classically, one finds by comparison

$$f_{cl}(\beta, \omega) = \frac{1}{\beta\epsilon}. \tag{2.22}$$

With this distribution, we compute Boltzmann-Landauer conductivities. The weight factor, $(\epsilon/k_B)\partial_T f$ (quantum mechanically $\epsilon = \hbar\omega$), which determines the contribution of vibrational modes to conductivity, is plotted in Fig.2.5 for both distribution functions.

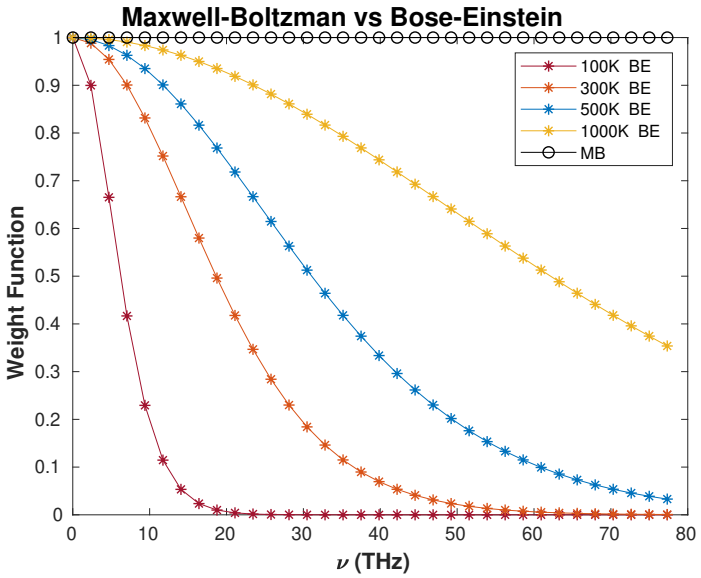

Figure 2.5. The comparision of the weigth factors with f indicates the distribution function. Weight factors are obtained at three different temperatures by using either the Maxwell-Boltzmann distribution function(MB) or the Bose-Einstein distribution function(BE).

The calculations are performed at different temperatures. Results show that the Maxwell-Boltzmann weight factor is independent of temperature, and all frequencies are equally probable. The dotted-black line on Fig.2.5 stands for Maxwell-Boltzmann weight factor. On the contrary, at lower temperatures, the considerable contribution comes from the lower energy states when the distribution function is the Bose-Einstein. The contri-

bution from the higher energy levels increases with the temperature rise. In Fig.2.5; red, orange, blue, and yellow starred lines indicate Bose-Einstein weight factor at 100 K, 300 K, 500 K, and 1000 K, respectively. The difference between Maxwell-Boltzmann and Bose-Einstein weight factors vanishes at sufficiently high temperatures. This behavior is very similar to heat capacity. In the classical limit, all the modes contribute to tunneling, while low energetic modes contribute at low temperatures.

2.3.1. Renormalization-Decimation Algorithm

The thermal reservoirs are perfect semi-infinite crystals. So now we are dealing with semi-infinite dynamical matrices. An efficient iterative algorithm for obtaining the surface Green's functions was developed by M.P. López Sancho, J.M. López Sancho and J Rubio[178]. The equivalent algorithm was proposed by F. Guinea et al.[179], and they studied two-dimensional Hamiltonians at surfaces. Moreover, Nardalli also used the method to study the electronic properties of carbon nanotubes.[180]. The algorithm is suitable for any dynamical matrix that can be expressed on a localized basis. Again, the system is divided into layers that are large enough so that just neighboring layers interact. Consequently, the dynamical matrix is in the following form:

$$D = \begin{pmatrix} D_{00} & D_{01} & & & & & \\ D_{10} & D_{00} & D_{01} & & & & \\ & \ddots & \ddots & \ddots & & & \\ & & \ddots & \ddots & \ddots & & \\ & & & \ddots & \ddots & \ddots & \\ & & & & & & \end{pmatrix} \text{ or } \begin{pmatrix} \ddots & \ddots & \ddots & & & & \\ & \ddots & \ddots & \ddots & & & \\ & & \ddots & \ddots & \ddots & & \\ & & & & D_{10} & D_{00} & D_{01} \\ & & & & & D_{10} & D_{00} \end{pmatrix}$$

where D_{00} represents the intralayer interactions, and D_{01} indicates the interactions between neighbouring layers. What we are interested in here is obtaining the surface green function of reservoirs.

The procedure starts with

$$t_0 = \left((\omega^2 + i\eta)\mathbb{1} - D_{00}\right)^{-1} D_{01}^{\dagger}$$
$$\tilde{t_0} = \left((\omega^2 + i\eta)\mathbb{1} - D_{00}\right)^{-1} D_{01}$$

and continue with

$$t_n = (\mathbb{1} - t_{n-1}\tilde{t}_{n-1} - \tilde{t}_{n-1}t_{n-1})^{-1} t_{n-1}^2$$
$$\tilde{t}_n = (\mathbb{1} - t_{n-1}\tilde{t}_{n-1} - \tilde{t}_{n-1}t_{n-1})^{-1} \tilde{t}_{n-1}^2$$

The iteration continues until $t_n, \tilde{t}_n \geq \sigma$, where σ is arbitrarly small. Then, each iteration was joined to the existing one

$$T = t_0 + \tilde{t}_0 t_1 + \tilde{t}_0 \tilde{t}_1 t_2 + \ldots$$
$$\tilde{T} = \tilde{t}_0 + t_0 \tilde{t}_1 + t_0 t_1 \tilde{t}_2 + \ldots$$

Finally, the surface Green's functions of reservoirs are determined by

$$G(\omega) = \left((\omega^2 + i\eta)\mathbb{1} - D_{00} - D_{01}T - D_{01}^{\dagger}\tilde{T}\right)^{-1} \tag{2.23}$$

In this study, thermal reservoirs are identical. If not, the calculation process of surface Green's functions shall be slightly different. Finally, while applying Green's functions, one to two blocks of crystal reservoirs to the left and right of the scattering region should be included so that the interaction matrices($D_{ld(rd)}$) are also constructed from the $D_{01(10)}$ matrices.

2.3.2. Decimation Technique

When systems extend, Green's functions technique faces computational power problems. We have overcome these problems using the decimation technique, an effective tool to handle while working with extended systems.[178–180] The decimation method

is a numerical approach to reduce input matrix size; thus, the technique reduces both memory consumption and computing time.[181, 182] The Green's function method is an order N^2 in memory and due to matrix inversion order N^3 in operation time. With the decimation algorithm, Green's functions method shall gain memory and time since the decimation method is an order N method.

To derive the elemental equation of decimation, consider a dynamical matrix of a bipartite system, all elements of which are themselves invertible matrices

$$D = \begin{pmatrix} D_{11} & D_{12} \\ D_{21} & D_{22} \end{pmatrix} \tag{2.24}$$

where $D_{\alpha\beta} = D^{\dagger}_{\beta\alpha}$. The relevant Green's function of the system

$$G(\omega) = \left((\omega^2 + i\eta)\mathbb{1} - D\right)^{-1} \tag{2.25}$$

$$= \begin{pmatrix} G_{11}(\omega) & G_{12}(\omega) \\ G_{21}(\omega) & G_{22}(\omega) \end{pmatrix} \tag{2.26}$$

Rewriting Eq.2.8 in the form $G(\omega)\ [(\omega^2 + i\eta) - D] = \mathbb{1}$, and expanding the equation, we obtain four equations

$$[(\omega^2 + i\eta)\mathbb{1} - D_{11}]\ G_{11}(\omega)\ +\ D_{12}\ G_{21}(\omega)\ =\ 1 \tag{2.27}$$

$$D_{21}\ G_{11}(\omega)\ +\ [(\omega^2 + i\eta)\mathbb{1} - D_{22}]\ G_{21}(\omega)\ =\ 0 \tag{2.28}$$

$$[(\omega^2 + i\eta)\mathbb{1} - D_{11}]\ G_{12}(\omega)\ +\ D_{12}\ G_{22}(\omega)\ =\ 0 \tag{2.29}$$

$$D_{21}\ G_{12}(\omega)\ +\ [(\omega^2 + i\eta)\mathbb{1} - D_{22}]\ G_{22}(\omega)\ =\ 1 \tag{2.30}$$

Rearranging Eq.2.27 as

$$G_{21}(\omega)\ =\ -[(\omega^2 + i\eta)\mathbb{1} - D_{22}]^{-1}\ D_{21}\ G_{11}(\omega) \tag{2.31}$$

and substituting into Eq.2.28 gives

$$\Big([(\omega^2 + i\eta) - D_{11}] \; - \; D_{12} \, [(\omega^2 + i\eta)\mathbb{1} - D_{22}]^{-1} \, D_{21} \Big) \, G_{11}(\omega) \; = \; \mathbb{1} \tag{2.32}$$

Finally, we obtain the elemental equation of decimation:

$$G_{11}(\omega) \; = \; \Big([(\omega^2 + i\eta)\mathbb{1} - D_{11}] \; - \; D_{12} \, [(\omega^2 + i\eta) - D_{22}]^{-1} \, D_{21} \Big)^{-1} \tag{2.33}$$

Remember, $G_{22}(\omega) = \big((\omega^2 + i\eta)\mathbb{1} - D_{22}\big)^{-1}$ So, the elemental equation becomes

$$G_{11}(\omega) \; = \; \Big([(\omega^2 + i\eta)\mathbb{1} - D_{11}] \; - \; D_{12} \, G_{22}(\omega) \, D_{21} \Big)^{-1} \tag{2.34}$$

Consequently, the effective dynamical matrix of the system 1:

$$D_{11}^{\text{eff}} \; = \; D_{11} \; + \; D_{12} \, G_{22}(\omega) \, D_{21} \tag{2.35}$$

one can similarly derive the other parts.

To demonstrate an application, now begin with the dynamical matrix of a tripartite system

$$D \; = \; \begin{pmatrix} D_{11} & D_{12} & D_{13} \\ D_{21} & D_{22} & D_{23} \\ D_{31} & D_{32} & D_{33} \end{pmatrix} \tag{2.36}$$

The corresponding Green's function is

$$G(\omega) \; = \; \big((\omega^2 + i\eta)\mathbb{1} - D\big)^{-1} \tag{2.37}$$

$$= \begin{pmatrix} G_{11}(\omega) & G_{12}(\omega) & G_{13}(\omega) \\ G_{21}(\omega) & G_{22}(\omega) & G_{23}(\omega) \\ G_{31}(\omega) & G_{32}(\omega) & G_{33}(\omega) \end{pmatrix} \tag{2.38}$$

We are only interested in the first and third systems, not the second one. So, decimating

out the central system gives

$$\begin{pmatrix} D_{11}^{\text{eff}} & D_{12}^{\text{eff}} \\ D_{21}^{\text{eff}} & D_{22}^{\text{eff}} \end{pmatrix} = \begin{pmatrix} D_{11} + D_{12}G_{22}(\omega)D_{21} & D_{13} + D_{12}G_{22}(\omega)D_{23} \\ D_{13} + D_{32}G_{22}(\omega)D_{23} & D_{33} + D_{32}G_{22}(\omega)D_{23} \end{pmatrix} \tag{2.39}$$

The Green's function can now be determined by

$$\begin{pmatrix} G_{11}(\omega) & G_{13}(\omega) \\ G_{31}(\omega) & G_{33}(\omega) \end{pmatrix} = \left((\omega^2 + i\eta)\mathbb{1} - \begin{pmatrix} D_{11}^{\text{eff}} & D_{12}^{\text{eff}} \\ D_{21}^{\text{eff}} & D_{22}^{\text{eff}} \end{pmatrix} \right)^{-1} \tag{2.40}$$

Lastly, to reveal the general procedure, consider the dynamical matrix of an extended system

$$D = \begin{pmatrix} D_{11} & D_{12} & & & & & \\ D_{21} & D_{22} & D_{23} & & & & \\ & \ddots & \ddots & \ddots & & & \\ & & \ddots & \ddots & \ddots & & \\ & & & D_{N-1,N-2} & D_{N-1,N-1} & D_{N-1,N} \\ & & & & D_{N,N-1} & D_{N,N} \end{pmatrix} \tag{2.41}$$

Decimating out the second cell of the input matrix

$$\begin{pmatrix} D_{11}^{(1)} & D_{12}^{(1)} & & & & \\ D_{21}^{(1)} & D_{22}^{(1)} & D_{23}^{(1)} & & & \\ & \ddots & \ddots & \ddots & & \\ & & & & D_{N-1,N-1}^{(1)} \end{pmatrix} =$$

$$= \begin{pmatrix} D_{11}^{(0)} + D_{12}^{(0)}G_{22}^{(0)}(\omega)D_{21}^{(0)} & D_{12}^{(0)}G_{22}^{(0)}(\omega)D_{23}^{(0)} & \dots & \dots & 0 \\ D_{32}^{(0)}G_{22}^{(0)}(\omega)D_{21}^{(0)} & D_{33}^{(0)} + D_{32}^{(0)}(\omega)G_{22}^{(0)}D_{23}^{(0)} & D_{34}^{(0)} & & \\ 0 & D_{43}^{(0)} & D_{44}^{(0)} & \ddots & \\ \vdots & & \ddots & \ddots & \\ 0 & & \dots & \dots & D_{N,N}^{(0)} \end{pmatrix}$$

where $G_{22}^{(0)}(\omega) = \left((\omega^2 + i\eta)\mathbb{1} - D_{22}\right)^{-1}$, and $D_{ij}^{(0)} = D_{ij}$. And again, decimating out the

second cell of the once-decimated matrix gives

$$\begin{pmatrix} D_{11}^{(2)} & D_{12}^{(2)} & & & & \\ D_{21}^{(2)} & D_{22}^{(2)} & D_{23}^{(2)} & & & \\ & & \ddots & \ddots & \ddots & \\ & & & & & D_{N-2,N-2}^{(2)} \end{pmatrix} =$$

$$= \begin{pmatrix} D_{11}^{(1)} + D_{12}^{(1)} G_{22}^{(1)}(\omega) D_{21}^{(1)} & D_{12}^{(1)} G_{22}^{(1)}(\omega) D_{23}^{(1)} & \dots & \dots & 0 \\ D_{32}^{(1)} G_{22}^{(1)}(\omega) D_{21}^{(1)} & D_{33}^{(1)} + D_{32}^{(1)} G_{22}^{(1)}(\omega) D_{23}^{(1)} & D_{34}^{(1)} & & \\ 0 & D_{43}^{(1)} & D_{44}^{(1)} & \ddots & \\ \vdots & & \ddots & \ddots & \\ 0 & & \dots & \dots & D_{N-1,N-1}^{(1)} \end{pmatrix}$$

where $G_{22}^{(1)}(\omega) = \left((\omega^2 + i\eta)\mathbb{1} - D_{22}^{(1)}\right)^{-1}$. The algorithm continues in this manner. We can deduce a general formulation since only the neighboring elements of the decimated cell are affected at each decimation step.

$$\begin{aligned} G_{22}^{(n)}(\omega) &= \left((\omega^2 + i\eta)\mathbb{1} - D_{22}^{(n)}\right)^{-1} \\ D_{11}^{(n+1)} &= D_{11}^{(n)} + D_{12}^{(n)} G_{22}^{(n)}(\omega) D_{21}^{(n)} \\ D_{12}^{(n+1)} &= D_{12}^{(n)} G_{22}^{(n)}(\omega) D_{23}^{(n)} \\ D_{21}^{(n+1)} &= D_{32}^{(n)} G_{22}^{(n)}(\omega) D_{23}^{(n)} \\ D_{22}^{(n+1)} &= D_{33}^{(n)} + D_{32}^{(n)} G_{22}^{(n)}(\omega) D_{23}^{(n)} \end{aligned}$$

Finally, we obtain the effective dynamical matrix

$$\begin{pmatrix} D_{11}^{\text{eff}} & D_{12}^{\text{eff}} \\ D_{21}^{\text{eff}} & D_{22}^{\text{eff}} \end{pmatrix} = \begin{pmatrix} D_{11}^{(N-2)} & D_{12}^{(N-2)} \\ D_{21}^{(N-2)} & D_{22}^{(N-2)} \end{pmatrix}$$

Also, we print the algorithm of the procedure.

Consider a carbon nanotube's tripartite dynamical matrix for a practical application. The entire tube can be divided into blocks, which are extensive enough that there is just interaction between neighboring blocks. So, the relevant matrix is a finite block

Algorithm: Decimation Technique

Input : $D,\ \omega(\eta)$

$d\_oo \leftarrow D(1,1); \quad d\_on \leftarrow D(1,2)$

$d\_no \leftarrow D(2,1); \quad d\_nn \leftarrow D(2,2)$

while $i \leftarrow 3 : N$ **do** ▷ where N is the number of blocks

  $g \leftarrow (\omega(\eta)\mathbb{1} - d\_nn)^{-1}$

  $d\_oo \leftarrow d\_oo + d\_on * g * d\_no$

  $d\_on \leftarrow d\_on * g * D(i-1,\ i)$

  $d\_no \leftarrow D(i,\ i-1) * g * d\_no$

  $d\_nn \leftarrow d\_nn + D(i,\ i-1) * g * D(i-1,\ i)$

$D^{\text{eff}} \leftarrow [[d\_oo, d\_on], [d\_no, d\_nn]]$

out $\leftarrow D^{\text{eff}}$

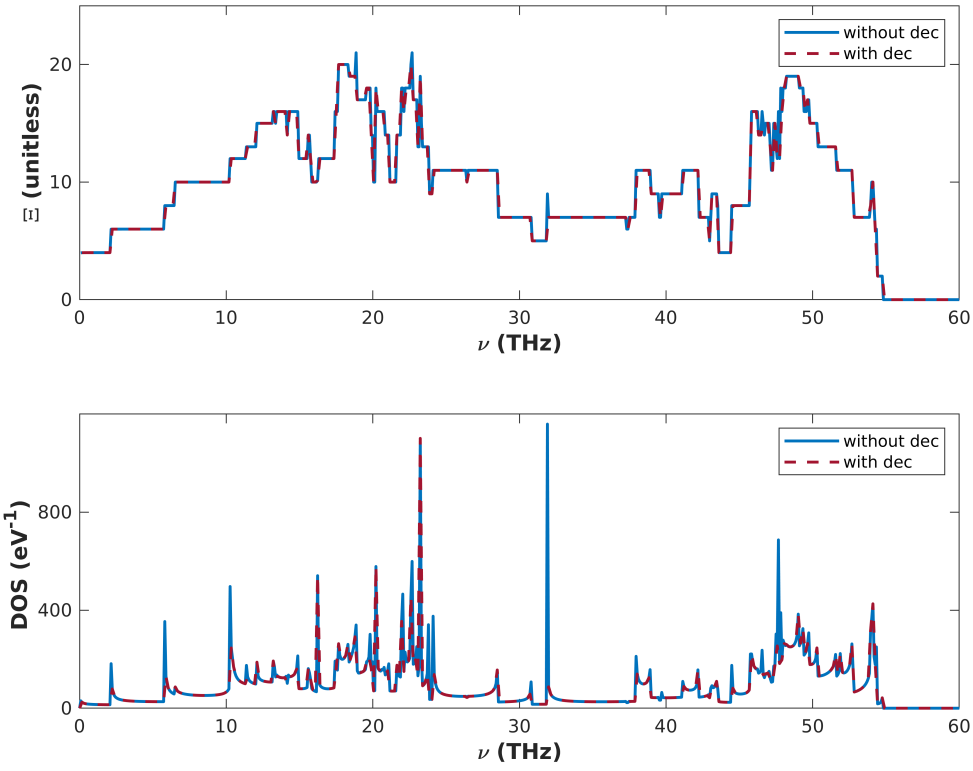

Figure 2.6. (5,5) Armchair carbon nanotube transmission and density of states, calculated with and without decimation technique to validate decimation technique.

tridiagonal form. 2Nx2N effective dynamical matrix is obtained by applying the decimation algorithm recursively to the input matrix, where N is the total number of degrees of freedom in a block. Applying the algorithm should not change any numerical result, as seen in Fig.2.6. We apply this method to one-dimensional atom chains for the tunneling work where chains' lengths can be extended to 120000 atoms long.

2.4. Kubo-Greenwood Method

Kubo-Greenwood is an efficient method to handle disordered, glass-like, amorphous nanostructures. The method includes quantum mechanical effects intrinsically and is based on a real-time propagation of an initial wave packet.[182–184] Basically, the Kubo-Greenwood method superimposes a random phase vector on the system, tracks how it evolves, and extracts a propagation feature. The propagation properties are averaged over multiple random vectors. As a result, thermal properties are deduced. Nonequilibrium Green's function method is an efficient alternative theory that also contains quantum mechanical effects. However, by definition, thermal reservoirs are perfectly ordered bulk crystals, creating interfaces between reservoirs and amorphous device regimes. Besides, the Kubo-Greenwood method can handle larger systems than the nonequilibrium Green functions scheme without any spatial limitations. Most importantly, the Kubo-Greenwood scheme's computational cost is linearly dependent on the number of degrees of freedom, i.e., an order-N method.

The vibrational Hamiltonian within harmonic approximation is defined as

$$H = \sum_i \frac{\hat{p}_i^2}{2M_i} + \sum_{ij} \Phi_{ij} \hat{u}_i \hat{u}_j \tag{2.42}$$

with $\hat{u}_i$ and $\hat{p}_i$ being the displacement and momentum operators of the ith degrees of freedom, respectively. Φ indicates the force contant tensor, and M_i is the mass. Kubo's formula relates the phonon conductivity, σ, along the x direction to the current-current correlation function.

$$\kappa = \Omega T^{-1} \lim_{\omega \to 0} \lim_{\eta \to 0} \int_0^\beta d\lambda \int_0^\infty dt e^{i(\omega + i\eta)t} \langle \hat{J}^x(-i\hbar\lambda) \hat{J}^x(t) \rangle \tag{2.43}$$

where T and Ω are temperature and volume, respectively. The x component of energy

flux operator, $\hat{J^x}$, is defined as

$$\hat{J^x} = 1/2\Omega \sum_{ij} (\hat{X}_i - \hat{X}_j)\Phi_{ij}\hat{u}_i\hat{v}_j \tag{2.44}$$

with velocity operator, $\hat{v}_j$, and equilibrium position of ith degrees of freedom, $\hat{X}_j$. $\hat{J^x}$ can be expressed in annihilation and creation operators, $\hat{J^x} = \sum_{m,n} J^x_{mn}\hat{a}_m \dagger \hat{a}_n$, with

$$J^x = \sum_{m,n} J^x_{mn}\left(\sqrt{\frac{\omega_m}{\omega_n}} + \sqrt{\frac{\omega_n}{\omega_m}}\right)\langle m|[X, D]|n\rangle \tag{2.45}$$

where D indicates mass-normalized dynamical matrix, and X demonstrates the diagonal matrix of equilibrium positions. Allen and Feldman demonstrated that the phonon conductivity can be expressed as

$$\kappa = \frac{\pi\Omega}{\hbar T}\sum_{m,n}\frac{\partial f_b}{\partial\omega_m}J^x_{mn}J^x_{nm}\delta(\omega_m - \omega_n) \tag{2.46}$$

with f_b being the Bose-Einstein distribution function. Defining $V_x = -i[X, D]$, the thermal conductivity of a one-dimensional system can be written as

$$\kappa = -\frac{\pi}{\Omega}\int_0^\infty d\omega\frac{\hbar}{4\omega}\frac{\partial f_b}{\partial T}\,\mathrm{Tr}\{V_x\delta(w - \sqrt{D})V_x(\omega - \sqrt{D})\} \tag{2.47}$$

where $\sqrt{D} = \sum_n \omega_n|n\rangle\langle n|$, and $\mathrm{Tr}\{...\}$ is the trace operator. When comparing the Landauer formula (recall Eq.1.2), we deduce transmission function as

$$\Xi(\omega) = \frac{2\pi^2}{L^2}\,\mathrm{Tr}\{V_x\delta(w - \sqrt{D})V_x(\omega - \sqrt{D})\} \tag{2.48}$$

In diffusion regime, transmission coefficient can be expressed in terms of diffusion coefficient, $\mathcal{D}$,

$$\Xi(\omega) = \frac{2\omega\pi}{L^2}\,\mathrm{Tr}\{\delta(w^2 - D)\}\mathcal{D}_{max}(\omega) \tag{2.49}$$

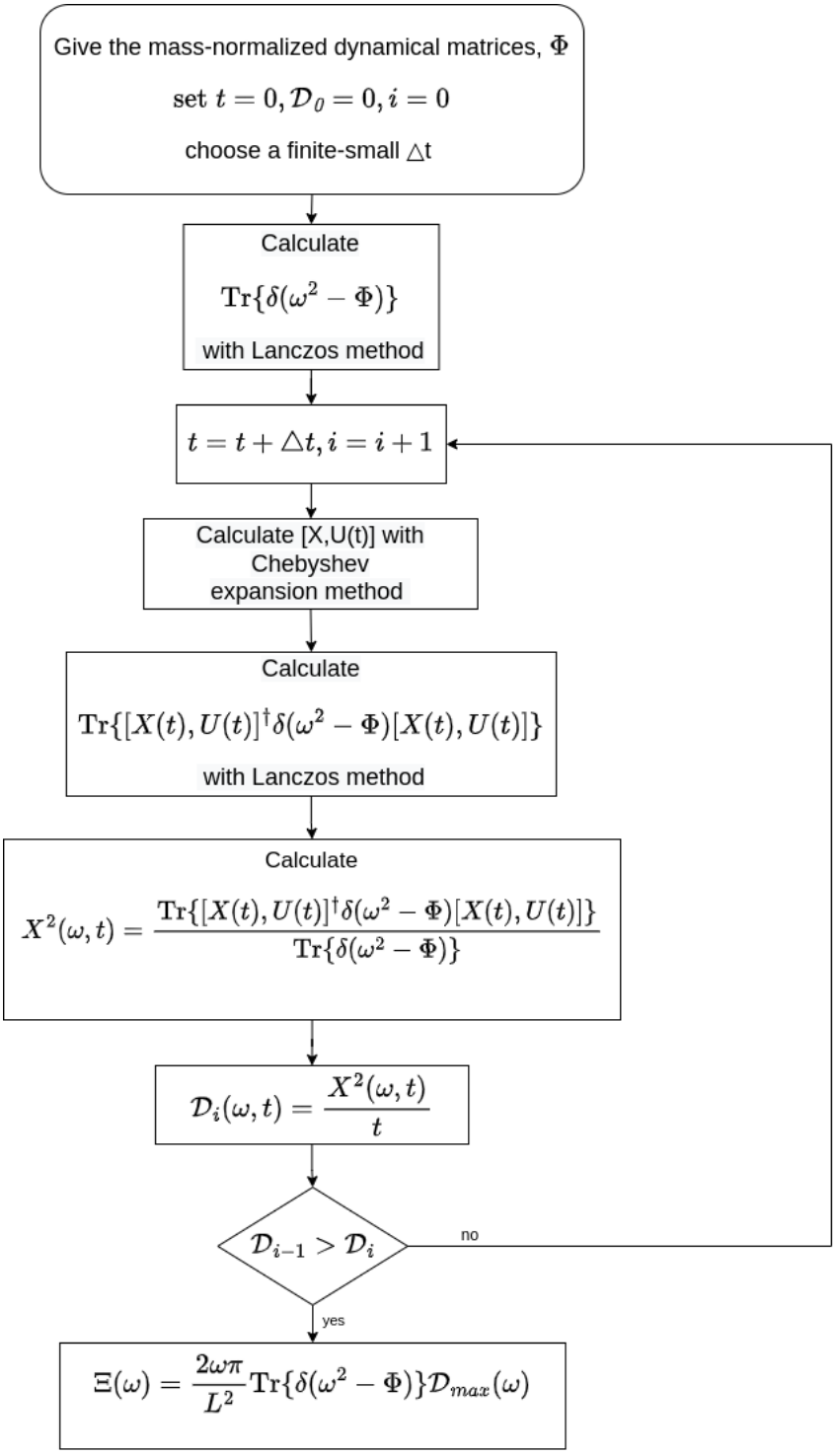

Figure 2.7. The flowchart of the Kubo-Greenwood method.

where $\mathcal{D} = X^2/t$. The definition of the mean square displacement is

$$\chi^2(\omega, t) = \frac{\mathrm{Tr}\{[X, U(t)]^\dagger \delta(\omega^2 - \sqrt{D})[X, U(t)]\}}{\mathrm{Tr}\{\delta(\omega^2 - \sqrt{D})\}} \tag{2.50}$$

The mean square displacement, X^2, is the central quantity in the Kubo-Greenwood scheme. The flowchart for the implementation procedure of the Kubo-Greenwood scheme is illustrated in Fig.2.7. The only input is the mass-normalized dynamical matrix. The mean-square displacement can be computed using Lanczos tridiagonalization, continued fraction method, and Chebyshev expansion polynomials. Bra-kets are calculated using the Lanczos and continued fraction methods. The Lancoz technique enables the simulation of large systems by avoiding matrix inversions. It is an iterative method to solve the eigenvalue problem of linear integral and differential operators. The use of Chebyshev expansion computes time evaluation. The numerator of mean square displacement is determined for each iteration, and the diffusion constant is calculated from the mean square displacement. The Kubo-Greenwood iteration continues until the maximum diffusion coefficient is reached. $\mathrm{Tr}\{[X, U(t)]^\dagger \delta(\omega^2 - \sqrt{D})[X, U(t)]\}$ are averaged over certain number of random vectors.

One essential feature of thermal properties is mean free path, which barry information about how disorder limits the thermal conductivity; and, mean free path is extracted via

$$\mathrm{mfp}(\omega) = \frac{\mathcal{D}_{max}(\omega)}{2\upsilon(\omega)} \tag{2.51}$$

where $\upsilon(\omega)$ is the avarage group velocity. In this study, all phonon group velocities are obtained by PHONOPY package.[185, 186]

2.4.1. Lanczos and continued fraction method

The Lanczos method used to tridiagonalize the dynamical matrix is robust for defect-associated problems.[187] The process is followed by the continued fraction expansion, which computes Green's functions matrix elements and the total density of states.[182–184, 188]

$$\mathrm{Tr}\big\{\{\delta(\omega^2 - D)\}\big\} = \sum_{i=1}^{N_d} \langle\psi_i\big|\delta(\omega^2 - D)\big|\psi_i\rangle = \frac{N_d}{N_{rp}} \times \sum_{J=1}^{N_{rp}} \langle\psi_{rp}^J\big|\delta(\omega^2 - D)\big|\psi_{rp}^J\rangle \tag{2.52}$$

$$\big|\psi_{rp}\rangle = \frac{1}{\sqrt{N_d}} \sum_{i=1}^{N_d} e^{i2\pi\theta_i} \big|\psi_i\rangle \tag{2.53}$$

The process starts with a normalized random phase vector $\big|\psi_1\rangle = \big|\psi_{rp}\rangle$:

$$a_1 = \langle\psi_1\big|D\big|\psi_1\rangle \tag{2.54}$$

$$\big|\tilde{\psi}_2\rangle = D\big|\psi_1\rangle - a_1\big|\psi_1\rangle \tag{2.55}$$

$$b_1 = \sqrt{\langle\tilde{\psi}_2\big|\tilde{\psi}_2\rangle} \tag{2.56}$$

$$\big|\psi_2\rangle = \frac{1}{b_1}\big|\tilde{\psi}_2\rangle \tag{2.57}$$

and $n > 1$ recursion steps:

$$a_n = \langle\psi_n\big|D\big|\psi_n\rangle \tag{2.58}$$

$$\big|\tilde{\psi}_{n+1}\rangle = D\big|\psi_n\rangle - a_n\big|\psi_n\rangle - b_{n-1}\big|\psi_{n-1}\rangle \tag{2.59}$$

$$b_n = \sqrt{\langle\tilde{\psi}_{n+1}\big|\tilde{\psi}_{n+1}\rangle} \tag{2.60}$$

$$\big|\psi_{n+1}\rangle = \frac{1}{b_1}\big|\tilde{\psi}_{n+1}\rangle \tag{2.61}$$

The coefficients a_n and b_n are diagonal and off-diagonal matrix elements of the tridiagonalized dynamical matrix and named recursion coefficients. Now, our dynamical matrix in the Lanczos basis is as follows:

$$\tilde{D} = \begin{pmatrix} a_1 & b_1 & & & \\ b_1 & a_2 & b_2 & & \\ & b_2 & \ddots & \ddots & \\ & & \ddots & \ddots & b_n \\ & & & b_n & a_n \end{pmatrix} \tag{2.62}$$

Here, the dynamical matrix is based on the tight binding. The total density of states can be deduced as a continued fraction.

$$\langle\psi_{rp}\big|\delta(\omega^2 - D)\big|\psi_{rp}\rangle = \lim_{n\to 0} -\frac{1}{\pi}\mathrm{Im}\Big(\langle\psi_{rp}\big|\frac{1}{\omega^2 + i\eta - D}\big|\psi_{rp}\rangle\Big) \tag{2.63}$$

$$\langle\psi_{rp}\big|\frac{1}{\omega^2 + i\eta - D}\big|\psi_{rp}\rangle = \cfrac{1}{\omega^2 + i\eta - a_1 - \cfrac{b_1^2}{\omega^2 + i\eta - a_2 - \cfrac{b_2^2}{\omega^2 + i\eta - a_3 - \cfrac{b_3^2}{\ddots}}}} \tag{2.64}$$

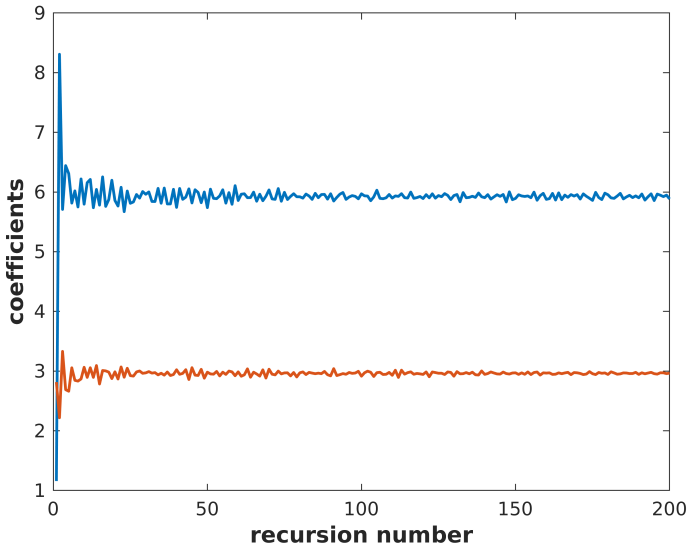

Figure 2.8. Recursion coefficients for pristine (5,5) armchair carbon nanotube. The blue line represents the coefficient a_n, and the red is the coefficient b_n.

$$G_1(\omega) = \cfrac{1}{\omega^2 + i\eta - a_1 - \cfrac{b_1^2}{\omega^2+i\eta-a_2-\cfrac{b_2^2}{\omega^2+i\eta-a_3-\cfrac{b_3^2}{\ddots}}}} \tag{2.65}$$

$$G_1(\omega) = \frac{1}{\omega^2 + i\eta - a_1 - b_1^2 G_2} \tag{2.66}$$

$$G_N(\omega) = \frac{1}{\omega^2 + i\eta - a_N - b_N^2 G_{N+1}} \tag{2.67}$$

The subspace of Lanczos is finite because recursion coefficients a_n and b_n oscillate around their average a and b value and tend quickly generally within a few hundred of the recursion step which depends on the complexity of phononic spectrum, see Fig.2.8. Then,

$$G_N(\omega) = \frac{1}{\omega^2 + i\eta - a_N - b_N^2 G_N} = \frac{1}{\omega^2 + i\eta - a_N - b_N^2 \Sigma(\omega)} \tag{2.68}$$

The termination is

$$\Sigma(\omega) = \frac{\omega^2 + i\eta - a - i\sqrt{(2b)^2 - (\omega^2 + i\eta - a)^2}}{2b^2} \tag{2.69}$$

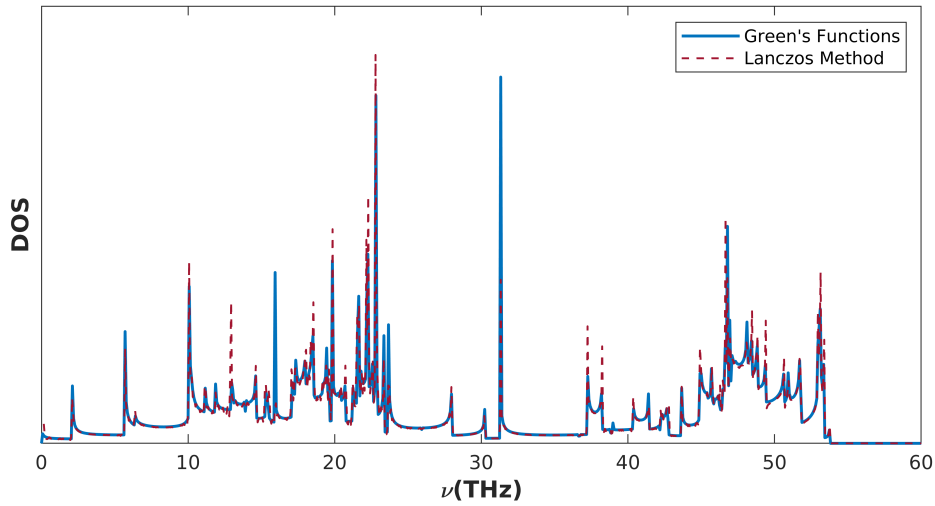

Figure 2.9. The total density of states for pristine (5,5) armchair carbon nanotube. The red dashed line is computed using Lanczos and continued fraction expansion. The blue line is calculated with Green's functions.

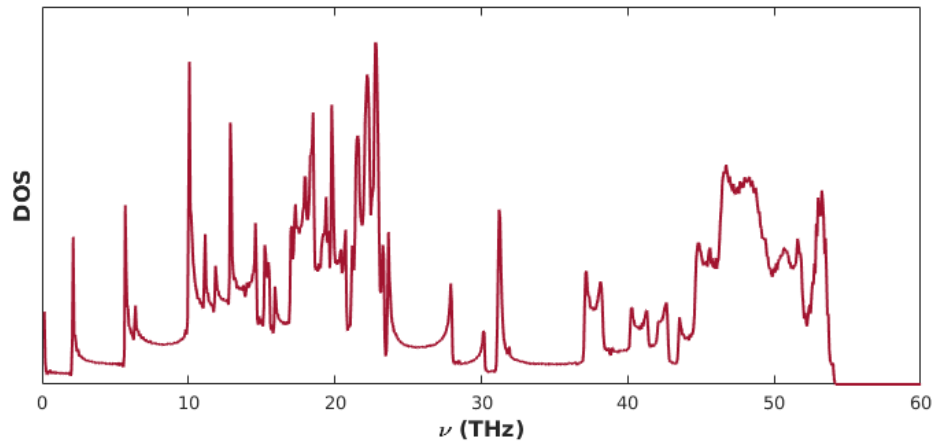

Figure 2.10. The total density of states for 50% isotopic mass-disordered (5,5) armchair carbon nanotube computed with Lanczos and continued fraction expansion.

Density of states are averaged over a certain number of random vectors. For a more detailed description, see Ref.[184]. The total density of states for pristine (5,5) armchair carbon nanotube is plotted in Fig.2.9 to validate the Lanczos method with Green's functions. Mass-disordered one is determined to advance Chebychev polynomial expansion because the rest of this method does not work for perfect, pristine systems(Fig.2.10).

2.4.2. Chebyshev Expansion of The Time Evolution Operator

Our method to determine the quantum-mechanical-thermal transport properties of amorphous graphene is Kubo-Greenwood. The central quantity to be calculated is the mean square displacement

$$\chi^2(\omega,t) = \frac{\mathrm{Tr}\{[X,U(t)]^\dagger \delta(\omega^2-\sqrt{D})[X,U(t)]\}}{\mathrm{Tr}\{\delta(\omega^2-\sqrt{D})\}} \tag{2.70}$$

where X is the position operator. The time development is determined with Chebyshev Expansion of $U(\triangle t)$. Any function of an operator can be expanded as

$$f(x) = \sum_{k=0}^{\infty} a_k T_k(x) \tag{2.71}$$

where $T_k(x) = \cos(k(\arccos\ x))$ is the kth Chebyshev polynomial, k is a nonnegative integer, and the definition of the Chebyshev coefficient, a_k

$$a_k = (2-\delta_{k0})\frac{1}{\pi}\int_{-1}^{1} f(x)T_k(x)\frac{dx}{\sqrt{(1-x^2)}} \tag{2.72}$$

where δ is the Kronecker-Delta function. An important property of Chebyshev polynomials [189–191]

$$\begin{aligned} T_0(x) &= 1 \\ T_1(x) &= x \\ T_k(x) &= 2xT_{k-1} - T_{k-2} \quad \text{where } k \geq 2 \end{aligned} \tag{2.73}$$

The electronic time evolution operator is the following

$$f(x) = U(\triangle t) = e^{-ix\triangle t} = \cos(x \triangle t) - i\sin(x \triangle t) \tag{2.74}$$

where x mimics the function of Hamiltonian in the time evolution operator. Just consider the real part of the operator

$$f(x) = \cos(x \triangle t) = \sum_{k=0}^{\infty} a_k T_k(x) \tag{2.75}$$

$$a_k = (2 - \delta_{k0})\frac{1}{\pi}\int_{-1}^{1} \cos(x \triangle t) T_k(x) \frac{dx}{\sqrt{(1-x^2)}} \tag{2.76}$$

let $x = \cos\phi$; then $T_k(\cos\phi) = \cos(k\phi)$. Then the coefficient formula of the real part becomes

$$a_k = (2 - \delta_{k0})\frac{1}{\pi}\int_{0}^{\pi} \cos(\triangle t \cos\phi)\cos(k\phi) d\phi \tag{2.77}$$

Similarly, for the imaginary part, $f(x) = \sin(x \triangle t)$

$$f(x) = \sin(x \triangle t) = \sum_{k=0}^{\infty} a_k T_k(x) \tag{2.78}$$

$$a_k = (2 - \delta_{k0})\frac{1}{\pi}\int_{-1}^{1} \sin(x \triangle t) T_k(x) \frac{dx}{\sqrt{(1-x^2)}} \tag{2.79}$$

let $x = \cos\phi$. Then the coefficient formula for the imaginary part becomes

$$a_k = (2 - \delta_{k0})\frac{1}{\pi}\int_{0}^{\pi} \sin(\triangle t \cos\phi)\cos(k\phi) d\phi \tag{2.80}$$

The Jacobi-Anger identity[192]

$$e^{ix\sin\phi} = J_0(x) + 2iJ_1(x)\sin\phi + 2J_2(x)\cos(2\phi) + 2iJ_3(x)\sin(3\phi) + 2J_4(x)\cos(4\phi) + ... \tag{2.81}$$

where $J_k(x)$ is the kth-order Bessel function of first kind. Equating the real and imaginary parts of the Jacobi-Anger identity gives

$$\cos(x\sin\phi) = J_0(x) + 2J_2(x)\cos(2\phi) + 2J_4(x)\cos(4\phi) + ...$$
$$\sin(x\sin\phi) = 2J_1(x)\sin\phi + 2J_3(x)\sin(3\phi) + 2J_5(x)\sin(5\phi) + ...$$

Change ϕ into $(\pi/2 - \phi)$, hence

$$\cos(x\cos\phi) = J_0(x) - 2J_2(x)\cos(2\phi) + 2J_4(x)\cos(4\phi) - .....$$
$$\sin(x\cos\phi) = 2J_1(x)\cos\phi - 2J_3(x)\cos(3\phi) + 2J_5(x)\cos(5\phi) - .....$$

Multiply the above formulas by $\cos k\phi$ and integrate from 0 to π

$$\int_0^\pi \cos k\phi\cos(x\cos\phi)d\phi = \int_0^\pi \Big\{ J_0(x) - 2J_2(x)\cos^2 2\phi + 2J_4(x)\cos^2 4\phi - .....\Big\}d\phi$$
$$\int_0^\pi \cos k\phi\sin(x\cos\phi)d\phi = \int_0^\pi \Big\{ 2J_1(x)\cos^2\phi - 2J_3(x)\cos^2(3\phi) + 2J_5(x)\cos^2(5\phi) - ..\Big\}d\phi$$

$$\int_0^\pi \cos k\phi\cos(x\cos\phi)d\phi = \frac{\pi}{2}\big\{1 + (-1)^k\big\}(-1)^{k/2}J_k(x)$$
$$\int_0^\pi \cos k\phi\sin(x\cos\phi)d\phi = \frac{\pi}{2}\big\{1 + (-1)^k\big\}(-1)^{(k-1)/2}J_k(x)$$

Finally,

$$\cos(x\triangle t) = \sum_{k=0}^{\infty}(2-\delta_{k0})\ \frac{1}{2}\ \big\{1 + (-1)^k\big\}(-1)^{k/2}J_k(\triangle t)T_k(x)$$
$$\sin(x\triangle t) = \sum_{k=0}^{\infty}(2-\delta_{k0})\ \frac{1}{2}\ \big\{1 + (-1)^k\big\}(-1)^{(k-1)/2}J_k(\triangle t)T_k(x)$$

We have plotted the real and imaginary parts of the electronic time evolution oper-

ator, computed numerically(marked) or analytically(dashed) in Fig.2.11. Each part converges in its corresponding analytic value quickly; this demonstrates the numerical stability of the Chebyshev expansion method.

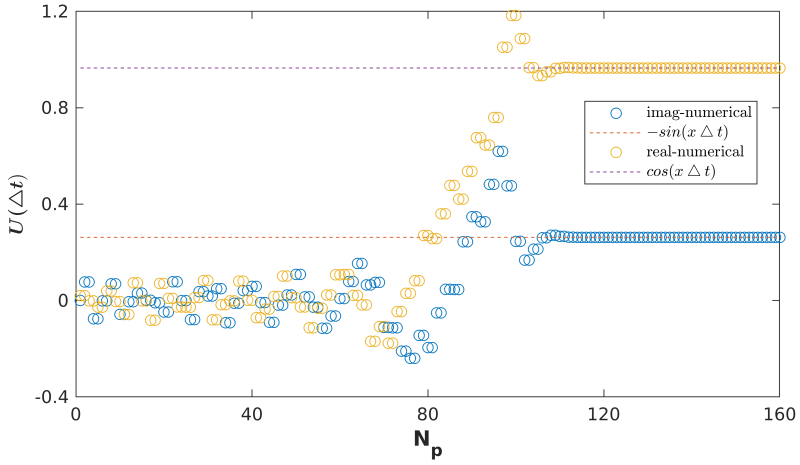

Figure 2.11. Illustration of the efficiency of Chebyshev expansion. The parameters have been chosen as $x = 0.5, \triangle t = 100$. x mimics the Hamiltonian role in the time evolution operator. So, this demonstrates the numerical stability of the expansion.

Algorithms for both Lanczos method and Chebyshev expansion are following

Algorithm: Lanczos tridiagonalization

Input : Φ

Starts with a normalized seed vector $|\psi_1\rangle$
$b_0 \leftarrow 0$
$|\psi_0\rangle \leftarrow 2$ ▷ it does not matter, since it will be multiplied by $b_0 = 0$
while $n \leftarrow 1 : N$ **do**
    $a_n \leftarrow \langle\psi_n|\Phi|\psi_n\rangle$
    $|\psi'_{n+1}\rangle \leftarrow \Phi|\psi_n\rangle - a_n|\psi_n\rangle - b_{n-1}|\psi_{n-1}\rangle$
    $b_n \leftarrow \sqrt{\langle\psi'_{n+1}|\psi'_{n+1}\rangle}$
    $\psi_{n+1} \leftarrow \frac{1}{b_n}|\psi'_{n+1}\rangle$

Algorithm: Chebyshev Polynomial expansion

Inputs : $\Phi, |\psi\rangle$

$|\alpha_0\rangle \leftarrow 0$
$|\alpha_1\rangle \leftarrow \Phi'|\psi\rangle$
$|\beta_0\rangle \leftarrow 0$
$c_1 \leftarrow 2(-i)^1 J_1(2b \triangle t)$ ▷ J_n: m_{th}-order Bessel function of first order
$|\beta_1\rangle \leftarrow [X, \Phi']|\psi\rangle$
out $\leftarrow c_1|\beta_1\rangle$
while $n \leftarrow 1 : N_{poly}$ **do**
    $|\alpha_{n+1}\rangle \leftarrow 2\Phi'|\alpha_n\rangle - |\alpha_{n-1}\rangle$
    $|\beta_{n+1}\rangle \leftarrow |\beta_n\rangle + 2[x, \Phi']|\alpha_n\rangle - |\beta_{n-1}\rangle$
    $c_n \leftarrow 2(-i)^n J_n(2b \triangle t)$
    $out \leftarrow out + c_n|\beta_{n+1}\rangle$
    $|\alpha_{n-1}\rangle \leftarrow |\alpha_n\rangle$
    $|\beta_{n-1}\rangle \leftarrow |\beta_n\rangle$
    $|\alpha_n\rangle \leftarrow |\alpha_{n+1}\rangle$
    $|\beta_n\rangle \leftarrow |\beta_{n+1}\rangle$
out $\leftarrow [X, U(\triangle t)]|\psi\rangle$

2.4.3. Chebyshev Expansion of the Time Evoluation Operator with Dynamical Matrix

Now, our matrix is not an electronic Hamiltonian; indeed, it is a dynamical matrix that is relevant to the vibrational properties of systems. Due to the fact that $Du = \omega^2 u$, the square root of the eigenvalues belonging to the dynamical matrix gives us the frequency of the normal modes of the corresponding system. The time evolution operator for the vibrational dynamics of the system is the following

$$U_D(\triangle t) = \exp\Big(-i \triangle t\sqrt{D}\Big) \tag{2.82}$$

First, one needs to scale dynamical matrices, $D' = (D - a)/2b$ (where a is midfrequency and $4b$ is the spectral range), since the Chebyshev polynomials' domain is in the range $[-1, 1]$.

$$\begin{aligned} e^{-i\triangle t\sqrt{x}} &= \sum_k a_k T_k(x') \\ &= \sum_k \left\{ \frac{2 - \delta_{k0}}{\pi} \int_{-1}^{1} dx' \ \frac{e^{-i\triangle t\sqrt{2bx'+a}} \ T_k(x')}{\sqrt{1 - x'^2}} \right\} T_k(x') \end{aligned}$$

The expansion coefficients are determined numerically with the Chebyshev-Gauss quadrature.

$$x' = \cos\left(\frac{\pi(n+\frac{1}{2})}{N}\right), \quad n = 0, 1, 2, ..., N-1 \tag{2.83}$$

These abscissas are the N zeros of the Chebyshev polynomial T_N. And the corresponding quadrature relation

$$\int_{-1}^{1} \frac{f(x')}{\sqrt{1-x'^2}}\, dx' = \frac{\pi}{N} \sum_{n=0}^{N-1} f(x') \tag{2.84}$$

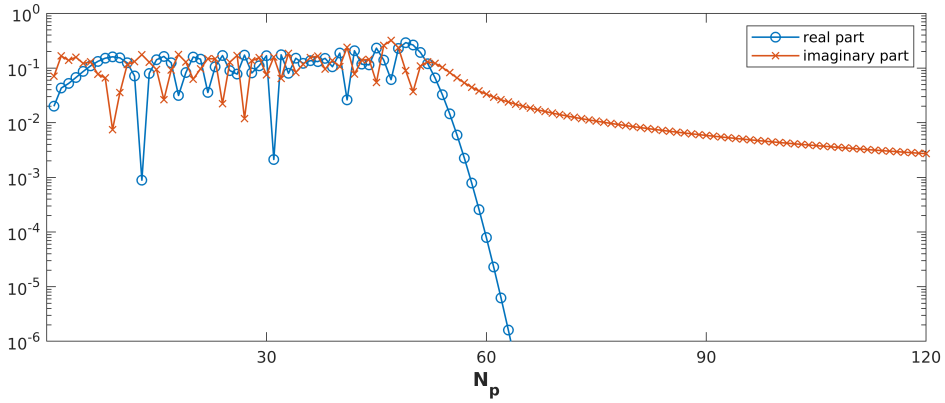

Figure 2.12. The absolute value of the real and imaginary part of Chebyshev expansion coefficients that are computed on a Chebyshev-Gauss grid.

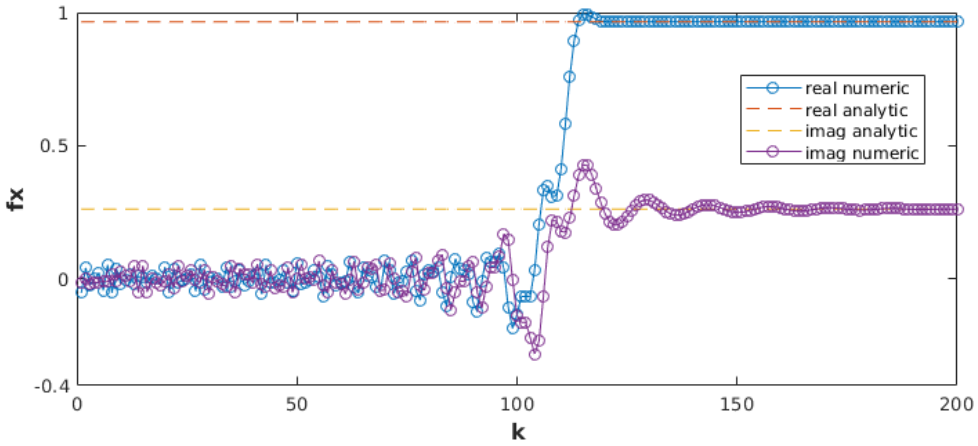

Figure 2.13. Real and imaginary parts of both numeric and analytic values of the function, $f(x) = e^{-i\sqrt{x}}$ for the x value of 2500 within the range $[0, 5\text{x}10^5]$.

The computed expansion coefficients are demonstrated in Fig.2.12 and are consistent with the existing literature.[183] Both the real and imaginary parts of the coefficients decay quickly with the number of Chebyshev polynomials, as expected, the condition for expansion convergence.Also, how the real and imaginary parts of the phononic time evolution operator quickly converge to their analytical value is shown in Fig.2.13.

2.4.4. Time Iteration

The commutator is in the following form

$$[X, U(t)]|\psi\rangle = \sum_k a_k(t)[X, T_k(\Phi)]|\psi\rangle \tag{2.85}$$

Under the Eq.2.73, commutator becomes

$$[X, T_{k+1}(D')] = 2[X, D'T_k(D')] - [X, T_{k-1}(D')] \tag{2.86}$$

Implying $|\alpha_k\rangle = T_k(D')|\psi\rangle$ and $|\beta_k\rangle = [X, T_k(D')]|\psi\rangle$ one can write

$$|\beta_{k+1}\rangle = 2D'|\beta_k\rangle + 2[X, D']|\alpha_k\rangle - |\beta_{k-1}\rangle \tag{2.87}$$

where $|\beta_0\rangle = 0$ and $|\beta_1\rangle = [X, D']|\psi\rangle$ by definition. To compute $|\beta_k\rangle$, $|\alpha_k\rangle$ are needed. They satisfy the following relation via the Chebyshev polynomial relation, Eq.2.73

$$\begin{aligned} |\alpha_{k+1}\rangle &= T_{k+1}(D')|\psi\rangle \\ &= 2D'|\alpha_k\rangle - |\alpha_{k-1}\rangle \end{aligned}$$

where $|\alpha_0\rangle = |\psi\rangle$ and $|\alpha_1\rangle = D'|\psi\rangle$. Finally, the time evolution operator and commutator can be computed via

$$U(\triangle t)|\psi\rangle = \sum_{k}^{N_{poly}} a_k(\triangle t)|\alpha_k\rangle$$
$$[X, U(\triangle t)]|\psi\rangle = \sum_{k}^{N_{poly}} a_k(\triangle t)|\beta_k\rangle$$

N_{poly} depends on the bandwidth and the spectrum complexity.

Once the vectors $[X, U(\triangle t)]|\psi\rangle$ and $U(\triangle t)|\psi\rangle$, the time evolution can be computed as

$$\begin{aligned} U((m+1)\triangle t)\,|\psi\rangle &= e^{-i(1+m)\sqrt{D}\triangle t}\,|\psi\rangle \\ &= e^{-i\sqrt{D}\triangle t}\,e^{-im\sqrt{D}\triangle t}\,|\psi\rangle \\ &= U(\triangle t)\,U(m\triangle t)\,|\psi\rangle \end{aligned}$$

$$\begin{aligned} [X,\ U((m+1)\triangle t)] &= [X,\ e^{-i\sqrt{D}\triangle t}e^{-im\sqrt{D}\triangle t}]\,|\psi\rangle \\ &= [X,\ e^{-i\sqrt{D}\triangle t}]\,e^{-im\sqrt{D}\triangle t} + e^{-i\sqrt{D}\triangle t}[X,\ e^{-im\sqrt{D}\triangle t}]\,|\psi\rangle \\ &= [X,\ U(\triangle t)]U(m\triangle t) + U(\triangle t)[X,\ U(m\triangle t)]\,|\psi\rangle \end{aligned}$$

where $[A, BC] = [A, B]C + B[A, C]$.

2.4.5. Test Case: CNT(5,5) with isotop disorder

As a test case, we applied the method to the (5,5) a-CNT with 30% ^{14}C isotope disorder since the analytical formula for elastic mean free paths of a isotope disordered CNT can be also obtained by[88, 182, 183, 193]

$$\text{mfp}(\omega) = \frac{12\ a\ N_{uc}\ N_{ch}(\omega)}{\pi^2\ f\ \left|\frac{\triangle M}{M}\right|^2\ \rho_{uc}^2(\omega)\ \omega^2} \tag{2.88}$$

where a is the lattice vector in the translational direction, N_{uc} is the number of atoms in the unit cell, $N_{ch}(\omega)$ is the number of channels per unit cell, f is the percentage of the isotopic impurity, $\triangle M$ is the mass difference, M is the avarage mass, and $\rho(\omega)$ is the density of states per unit cell.

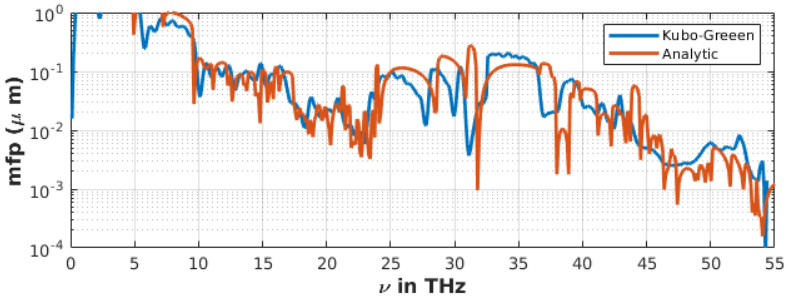

Figure 2.14. Mean free paths of (5,5) armchair carbon nanotube with 30% ^{14}C isotope disorder.

The analytic and numeric mean free paths are plotted in Fig.2.14. The numeric result is quite approximate to the analytic one. But, thermal conductivity values are in good agreement; see Fig.2.15, in which we have plotted the normalized thermal conductivities. The conductivity values are determined within the Landauer scheme, and the transmission values are calculated via $\Xi(\omega) = N_{ch}(\omega)/(1 + L/\text{ mfp}(\omega))$. The considerable reduction in conductivity is expected.[194] Here, the carbon nanotube length is $2.86\ \mu m$.

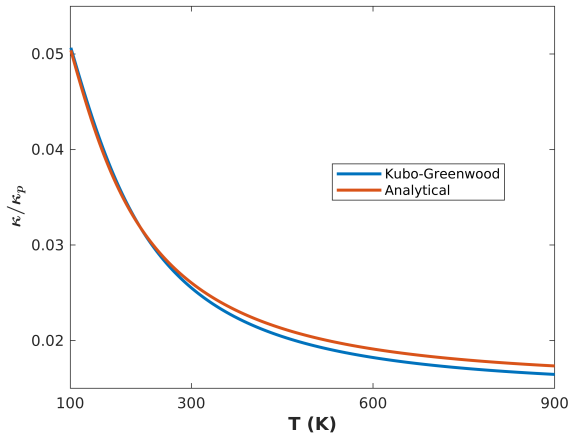

Figure 2.15. Normalized thermal conductivity of (5,5) armchair carbon nanotube with 30% ^{14}C isotope disorder.

CHAPTER 3

PHONON TUNNELING

In this study, by phonon tunneling, we mean the leakage of vibrational energy through a phononic gap system, which stops the propagation of vibrational modes that coincide with the frequency gap of its phononic spectrum. Hence, the system acts as a barrier to incoming phonons. In order to describe phonon tunneling principally, the symmetrical case, where the same material dwells on both sides of a barrier to act as thermal reservoirs, is examined in detail. For this case, the reservoirs are identical semi-infinite monoatomic chains, and the barrier, i.e., scattering region, is a finite diatomic chain with a gap in its phononic spectrum. Due to finite structure, the diatomic chain has a discrete spectrum; see middle plot of Fig.3.1. Also, in the figure, the right and left plots demonstrate the density of states of the semi-infinite chains, which are determined within NEGF formalism. All chains are one-dimensional for simplicity.

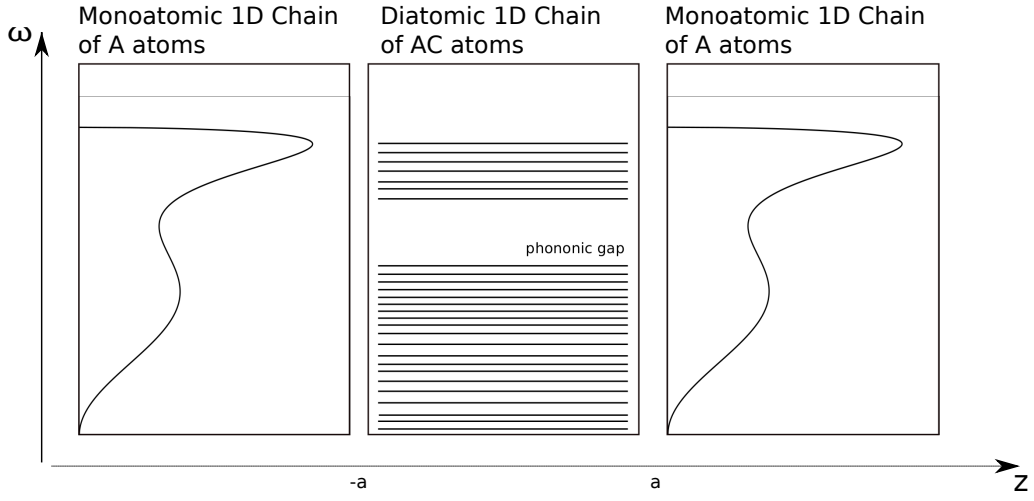

Figure 3.1. Schematic illustration of the reservoir-barrier-reservoir system. The left and right plots demonstrate the density of states of semi-infinite monoatomic chains. The middle demonstrates an exemplary discrete spectrum of a finite diatomic chain with a phononic gap.

Phonons are described by their dispersion relations that link the frequency to the wavevector, $\omega(\boldsymbol{q})$. In order to reveal the individual phononic properties of both monoatomic and diatomic chains, their phonon dispersion relations are determined. The

chains are modeled as coupled harmonic oscillators by considering the first nearest neighbors' interactions within the harmonic approximation; the elastic response is a quadratic function of small displacements of atoms around their equilibrium positions. An ordinary interatomic potential between two atoms can be considered parabolic near its minimum. The equation of motion, which is constructed by integrating Hooke's law into Newton's first law, is given for the monoatomic chain as[195–197]

$$m\ \ddot{u}_n = \mathbf{\Phi}\ (u_{n+1} - u_n) + \mathbf{\Phi}\ (u_n - u_{n-1}) \tag{3.1}$$

where $\mathbf{\Phi}$, m, and u denote force-constants, masses, and the displacements of atoms around their equilibrium condition, respectively. Plane waves solve the equation of motion.

$$u_n = \epsilon\ e^{i(\boldsymbol{q}z - \omega t)} = \epsilon\ e^{i(\boldsymbol{q}nd - \omega t)} \tag{3.2}$$

where ϵ, $\boldsymbol{q}$, and d refer to the amplitude of the motion of nth atom, the wave vector, and the atomic spacing of the chain, respectively. Since all atoms dwell in the same environment, one can adopt the periodic boundary condition

$$\begin{aligned} u_{N+1} &= u_1 \\ \epsilon\ e^{i[\boldsymbol{q}(N+1)d - \omega t]} &= \epsilon\ e^{i[\boldsymbol{q}d - \omega t]} \\ e^{i\boldsymbol{q}Nd} &= 1 \\ \boldsymbol{q} &= \frac{2\pi n}{Nd},\ n \in [0, 1, 2, 3, ..., N-1] \end{aligned}$$

Here, N is the number of atoms in the chain. Substitution of both the second derivative and definition of plane waves into the equation of motion gives

$$-m\omega^2 \epsilon\ e^{i(\boldsymbol{q}nd - \omega t)} = [\mathbf{\Phi}(\ e^{i\boldsymbol{q}d} - 1) + \mathbf{\Phi}(\ e^{-i\boldsymbol{q}d} - 1)]\epsilon\ e^{i(\boldsymbol{q}nd - \omega t)} \tag{3.3}$$

The arrangement of the above equation results in the dispersion relation of the monoatomic chain

$$\omega(\boldsymbol{q}) = \sqrt{\frac{4\mathbf{\Phi}}{M}} \left| \sin\left(\frac{1}{2}\boldsymbol{q}d\right) \right| \tag{3.4}$$

Each $\boldsymbol{q}$ value represents a normal mode. Dispersion of the monoatomic chain has translational symmetry with period $2\pi/d$.

The phonon dispersion relation of the diatomic chain can be determined by con-

sidering the chain with a basis of two non-equivalent atoms. Each atom is assumed to interact only with its first neighbors. The equations of motion for both types are

$$m_a\ \ddot{u}_s = \mathbf{\Phi}_{ac}\ (u_{s+1} - u_s) + \mathbf{\Phi}_{ac}\ (u_{s-1} - u_s)$$
$$m_c\ \ddot{u}_l = \mathbf{\Phi}_{ac}\ (u_{l+1} - u_l) + \mathbf{\Phi}_{ac}\ (u_{l-1} - u_l)$$

Assuming solutions have the form of traveling waves with different amplitudes on alternate planes, $u_s = \epsilon_s\ e^{i(\boldsymbol{Q}z - \omega t)}$, and $u_l = \epsilon_l\ e^{i(\boldsymbol{Q}z - \omega t)}$. The replacement of solutions to their corresponding equations of motion concludes in the following homogeneous linear equation

$$m_a m_c \omega^4 - 2\mathbf{\Phi}_{ac}(m_a + m_c)\omega^2 + 2\mathbf{\Phi}_{ac}^2(1 - \cos \boldsymbol{Q}d) = 0 \tag{3.5}$$

The roots of the equation provide the exact solutions of the dispersion of the diatomic chain

$$\omega(\boldsymbol{Q}) = \sqrt{\mathbf{\Phi}_{ac}(\frac{m_a + m_c \pm \sqrt{m_a^2 + m_c^2 + 2m_a m_c \cos \boldsymbol{Q}d}}{m_a m_c})} \tag{3.6}$$

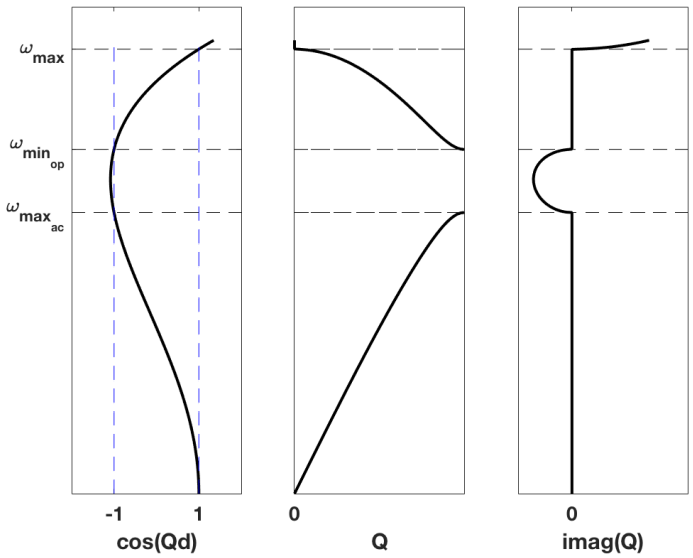

Figure 3.2. The dispersion relation of the diatomic chain. The wavevectors have imaginary values for the modes that fall inside the phononic gap. $\omega_{min_{op}}$, $\omega_{max_{ac}}$ stand for the minimum frequency of the optical band and maximum frequency of the acoustic band, respectively. $\omega_{min_{op}} = \sqrt{2\mathbf{\Phi}_{ac}/m_{light}}$, and $\omega_{max_{ac}} = \sqrt{2\mathbf{\Phi}_{ac}/m_{heavy}}$.

There are two dispersion branches, i.e., the optic and acoustic branches. For the acoustic branch, atoms oscillate in phase with each other, while for the optic branch, atoms perform out-of-phase movements. The middle graph of Fig.3.2 shows the dispersion relation of the diatomic chain. The acoustic branch ranges from 0 to $\omega_{max_{ac}} = \sqrt{2\mathbf{\Phi}_{ac}/m_{heavy}}$, while optic one ranges from $\omega_{min_{op}} = \sqrt{2\mathbf{\Phi}_{ac}/m_{light}}$ to $\omega_{max} = \sqrt{2\mathbf{\Phi}_{ac}(1/m_a + 1/m_c)}$. The dispersion relation of the diatomic chain has a distinct feature: phononic gap, which extends from $\omega_{max_{ac}}$ to $\omega_{min_{op}}$. The vibrational modes can not propagate inside the phononic gap, and the wavevectors, $\boldsymbol{Q}$, have imaginary values.[198] To illustrate this circumstance, an imaginary part of the dispersion is plotted on the right side of Fig.3.2. The solution of the equation of motion for the vibrational modes that fall inside the gap is in the form of

$$u(z) = \epsilon e^{\boldsymbol{Q}z} \tag{3.7}$$

and here we consider a time-independent situation and removed the $\exp(-i\omega t)$ factor.

After analyzing the phonon dispersion relations of individual chain, the reservoir-barrier-reservoir system can be discussed. Inside the band, oscillations are allowed, and the solutions are normal modes

$$u_i(z) = A_{r_i} e^{i\boldsymbol{q}z} + A_{l_i} e^{-i\boldsymbol{q}z} \tag{3.8}$$

where A_{r_i} and A_{l_i} represent coefficients of the waves propagating to the right and the left, respectively. i runs over the left reservoir, the barrier, and the right reservoir. For the modes that fall inside the phononic bands, the solution is in the form of

$$u(z) = \begin{cases} A_{r_l} e^{i\boldsymbol{q}z} + A_{l_l} e^{-i\boldsymbol{q}z}, & \text{if } x < -a. \\ A_{r_b} e^{i\boldsymbol{Q}z} + A_{l_b} e^{-i\boldsymbol{Q}z}, & \text{if } -a < x < x. \\ A_{r_r} e^{i\boldsymbol{q}z}, & \text{if } a < x. \end{cases} \tag{3.9}$$

where the capital symbol represents the wave vectors of the barrier region, $\boldsymbol{Q}$, to distinguish from the wave vectors of the reservoirs. The solutions with the amplitudes A_r, A_l, and A_r can be considered as the solutions of incident, reflected and transmitted waves,

respectively. For the modes that fall inside the phononic gap:

$$u(z) = \begin{cases} A_{r_l} e^{i\boldsymbol{q}z} + A_{l_l} e^{-i\boldsymbol{q}z}, & \text{if } x < -a. \\ A_{r_b} e^{-\boldsymbol{Q}z} + A_{l_b} e^{\boldsymbol{Q}z}, & \text{if } -a < x < a. \\ A_{r_r} e^{i\boldsymbol{q}z}, & \text{if } a < x. \end{cases} \tag{3.10}$$

The inverted dispersion relations determine the wave vectors $\boldsymbol{q}$ and $\boldsymbol{Q}$.

$$\boldsymbol{q} = \frac{2\arcsin\left(\omega\sqrt{\frac{m_a}{4\boldsymbol{\Phi}_{aa}}}\right)}{d_{aa}}$$

$$\boldsymbol{Q} = \frac{\arccos(m_a m_c/2\Phi_{ac}^2\,\omega^4 - ((m_a+m_c)/\boldsymbol{\Phi}_{ac}\omega^2) + 1)}{d_{ac}}$$

where $d_{aa}(d_{ac})$ is the repeating distance of the monoatomic(diatomic chains). The following step is to implement the continuity condition at boundaries.

Continuity of u at -a : $A_{r_l} e^{-i\boldsymbol{q}a} + A_{l_l} e^{i\boldsymbol{q}a} = A_{r_b} e^{\boldsymbol{Q}a} + A_{l_b} e^{-\boldsymbol{Q}a}$

Continuity of $\partial u/\partial z$ at -a : $i\boldsymbol{q}(A_{r_l} e^{-i\boldsymbol{q}a} + A_{l_l} e^{i\boldsymbol{q}a}) = \boldsymbol{Q}(A_{r_b} e^{\boldsymbol{Q}a} + A_{l_b} e^{-\boldsymbol{Q}a})$

$$2A_{r_l} e^{-i\boldsymbol{q}a} = (1 - i\frac{\boldsymbol{Q}}{\boldsymbol{q}})A_{r_b} e^{\boldsymbol{Q}a} + (1 + i\frac{\boldsymbol{Q}}{\boldsymbol{q}})A_{l_b} e^{-\boldsymbol{Q}a} \tag{3.11}$$

Continuity of u at a : $A_{r_b} e^{-\boldsymbol{Q}a} + A_{l_b} e^{\boldsymbol{Q}a} = A_{r_r} e^{i\boldsymbol{q}a}$

Continuity of $\partial u/\partial z$ at a : $-\boldsymbol{Q}(A_{r_b} e^{-\boldsymbol{Q}a} + A_{l_b} e^{\boldsymbol{Q}a}) = i\boldsymbol{q}(A_{r_r} e^{i\boldsymbol{q}a})$

$$A_{l_b} e^{\boldsymbol{Q}a}(1 + i\frac{\boldsymbol{q}}{\boldsymbol{Q}}) = A_{r_r} e^{i\boldsymbol{q}a} \;\;\&\;\; A_{r_b} e^{-\boldsymbol{Q}a} = (1 - i\frac{\boldsymbol{q}}{\boldsymbol{Q}})A_{r_r} e^{i\boldsymbol{q}a} \tag{3.12}$$

$$
\begin{aligned}
2A_{r_l}e^{-i\boldsymbol{q}a} &= (1-\frac{i\boldsymbol{Q}}{\boldsymbol{q}})(1+\frac{i\boldsymbol{q}}{\boldsymbol{Q}})A_{r_r}e^{i\boldsymbol{q}a}\frac{e^{-2\boldsymbol{Q}a}}{2} + (1+\frac{i\boldsymbol{Q}}{\boldsymbol{q}})(1-\frac{i\boldsymbol{q}}{\boldsymbol{Q}})A_{r_r}e^{i\boldsymbol{q}a}\frac{e^{2\boldsymbol{Q}a}}{2} \\
&= \frac{A_{r_r}e^{i\boldsymbol{q}a}}{2}\Big\{\Big[1+i\Big(\frac{\boldsymbol{q}}{\boldsymbol{Q}}-\frac{\boldsymbol{Q}}{\boldsymbol{q}}\Big)+1\Big]e^{-2\boldsymbol{Q}a} + \Big[1+i\Big(\frac{\boldsymbol{Q}}{\boldsymbol{q}}-\frac{\boldsymbol{q}}{\boldsymbol{Q}}\Big)+1\Big]e^{2\boldsymbol{Q}a}\Big\} \\
&= \frac{A_{r_r}e^{i\boldsymbol{q}a}}{2}\Big[2\big(e^{-2\boldsymbol{Q}a}+e^{2\boldsymbol{Q}a}\big)+i\frac{(\boldsymbol{Q}^2-\boldsymbol{q}^2)}{\boldsymbol{Q}\boldsymbol{q}}\big(e^{2\boldsymbol{Q}a}+e^{-2\boldsymbol{Q}a}\big)\Big] \\
&= \frac{A_{r_r}e^{i\boldsymbol{q}a}}{2}\Big[4\cosh(2\boldsymbol{Q})+i\frac{(\boldsymbol{Q}^2-\boldsymbol{q}^2)}{\boldsymbol{Q}\boldsymbol{q}}2\sinh(2\boldsymbol{Q}a)\Big] \\
&= 2A_{r_r}e^{i\boldsymbol{q}a}\Big[\cosh(2\boldsymbol{Q})+i\frac{(\boldsymbol{Q}^2-\boldsymbol{q}^2)}{2\boldsymbol{Q}\boldsymbol{q}}\sinh(2\boldsymbol{Q}a)\Big]
\end{aligned}
$$

Transmission coefficient, Ξ, can be determined by taking the ratio, A_{r_r}/A_{r_l}, and similarly reflection coefficient is defined as A_{l_l}/A_{r_l}. For the frequency range in which the barrier has no propagating vibrational mode, the transmission coefficient is found

$$
\Xi = \left|\frac{A_{r_r}}{A_{r_l}}\right|^2 = \frac{1}{\cosh^2(2\boldsymbol{Q}a)+\frac{(\boldsymbol{Q}^2-\boldsymbol{q}^2)^2}{(2\boldsymbol{Q}\boldsymbol{q})^2}\sinh^2(2\boldsymbol{Q}a)} \tag{3.13}
$$

In order to determine the transmission coefficient for the modes that fall inside the bands, one can follow the receipt that is applied above starting with solutions, Eq.3.9. The result is

$$
\Xi = \left|\frac{A_{r_r}}{A_{r_l}}\right|^2 = \frac{1}{\cos^2(2\boldsymbol{Q}a)+\frac{(\boldsymbol{Q}^2+\boldsymbol{q}^2)^2}{(2\boldsymbol{Q}\boldsymbol{q})^2}\sin^2(2\boldsymbol{Q}a)} \tag{3.14}
$$

Fig.3.3 presents the transmission coefficients in logarithmic scale as a function of barrier length. Inside the gap, the transmission coefficient decays exponentially. The exponential decay with barrier thickness is evidence of the tunneling effect. When the barrier chain is long enough to prevent tunneling, the vibrational modes within the gap can not be transmitted via the barrier. Otherwise, these modes can tunnel through the barrier by virtue of imaginary solutions. Outside the phononic gap, the transmission coefficient of allowed modes oscillates with the barrier length. Phonons inside the barrier region are repeatedly reflected from interfaces. Back-reflected phonons constructively or destructively interfere with each other. Inside barriers with different thicknesses, different phase shifts occur. Hence, various interference patterns are formed. This mechanism is well-known for Fabry-Perot interference.[199–201] In this way, the transmission coefficient oscillates with the thickness of the barrier region due to the phase difference.

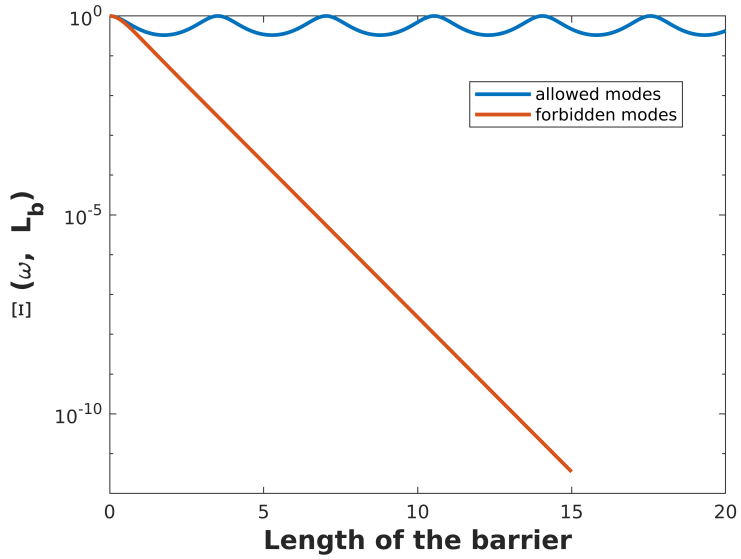

Figure 3.3. The transmission coefficients in logarithmic scale as a function of barrier length. While the transmission coefficient of the forbidden mode decays exponentially, the transmission coefficient of the allowed mode oscillates.

The organized version of the eq.3.14 is $\Xi = [1+((\boldsymbol{Q}^2-\boldsymbol{q}^2)/2\boldsymbol{Q}\boldsymbol{q})^2 \sin^2(2\boldsymbol{Q}a)]^{-1}$. The amplitude of oscillation that depends on the length of the barrier system is determined by the wavevectors of either the barrier or the reservoir while the oscillation period changes with both the length, a, and the wave vector of the barrier, $\boldsymbol{Q}$. In Fig.3.3, the transmission coefficients of two different modes are plotted. The allowed mode has a frequency that does not coincide with the phononic gap, while the forbidden mode propagates with a frequency that coincides with the stop band. While the allowed mode's transmission coefficient oscillates, the forbidden mode's transmission coefficient exponentially decays with the length.

3.1. Phonon Dichromator

The investigation of thermal properties of disordered materials occupies an essential position in phononics, as in other fields, since some characteristics of disordered materials can be desirable.[202, 203] Phonon propagation through disordered materials has been broadly supposed to be restricted due to the localization of the carriers.[204] However, a recent theoretical study uncovered the presence of anomalous transparent vi-

brational state despite disorders.[205] A transparent state appears in a one-dimensional harmonic chain with completely random disorders due to the intrinsic cooperation of force constant and mass disorders. The authors investigated a toy model based on nano-junction geometry where a binary alloy model, $A_{1-x}B_x$, with the impurity concentration x, is placed between two thermal reservoirs made up of monoatomic semi-infinite chains of A atoms. The geometry of nano-junction is illustrated in Fig.3.4. Within a monoatomic system, replacing an impurity atom creates simultaneous changes in the nearest neighboring force constants. When the force constant between the host and impurity atoms is a harmonic average,

$$\mathbf{\Phi}_{ab} = \frac{2\mathbf{\Phi}_{aa}\mathbf{\Phi}_{bb}}{(\mathbf{\Phi}_{aa} + \mathbf{\Phi}_{bb})} \tag{3.15}$$

there exists a common resonant state which gives perfect transmission. Here, $\mathbf{\Phi}_{aa}$, $\mathbf{\Phi}_{bb}$, and $\mathbf{\Phi}_{ab}$ are the force constants among the neighboring pairs of AA, BB, and AB(BA), respectively. According to the results, the phonon propagation through completely random disordered materials branches out into three regimes: I) The full localization regime where all states with high frequency are localized, and the transmission rapidly decays from unity to zero. In Fig.3.5, the red line displays the effect of localization due to simultaneous mass and force constant disorder that does not satisfy the harmonic relation. II) The sub-ballistic regime where a great number of transparent states exist. When a system satisfies the relation, $\mathbf{\Phi}_{aa}m_a = \mathbf{\Phi}_{bb}m_b$, besides the harmonic condition, nearly perfect transmission plateau appears within the low-frequency range, the brown line in Fig.3.5. III) The resonant regime where a common resonant state presents perfect transmission. The disordered systems, represented by the blue and maroon lines in Fig.3.5 exhibit the resonant behavior that exists in favor of the harmonic relation. The common resonant frequency(ω_{crf}) only depends on the intrinsic parameters, i.e., force constants and masses, and can be determined by

$$w_{crf} = 2\sqrt{\frac{\mathbf{\Phi}_{aa}\mathbf{\Phi}_{bb}(m_a\mathbf{\Phi}_{aa} - m_b\mathbf{\Phi}_{bb})}{m_a m_b(\mathbf{\Phi}_{aa}^2 - \mathbf{\Phi}_{bb}^2)}} \tag{3.16}$$

Consequently, it is insensitive to the system's size, impurity concentration, and atomic configuration. The masses of A-type and B-type atoms are represented by m_a and m_b.

The transmission spectrum of a specific long chain has completely random resonance peaks that have no track with the harmonic relation. Transmissions are averaged over 10^5 completely random configurations to remove those peaks. We set both m_a and $\mathbf{\Phi}_{aa}$ to 1.0 for all calculations. Without disorder, all states below the maximum (cut-off)

frequency give perfect transmission, such as the black line in Fig.3.5. The difference, $|\mathbf{\Phi}_{aa}m_a - \mathbf{\Phi}_{bb}m_b|$, gives information about the peaks' isolation. The greater difference means a narrower peak. For instance, the differences for the brown, maroon, and blue lines from Fig.3.5 are calculated as 0.10, 0.18, and 0.67, respectively.

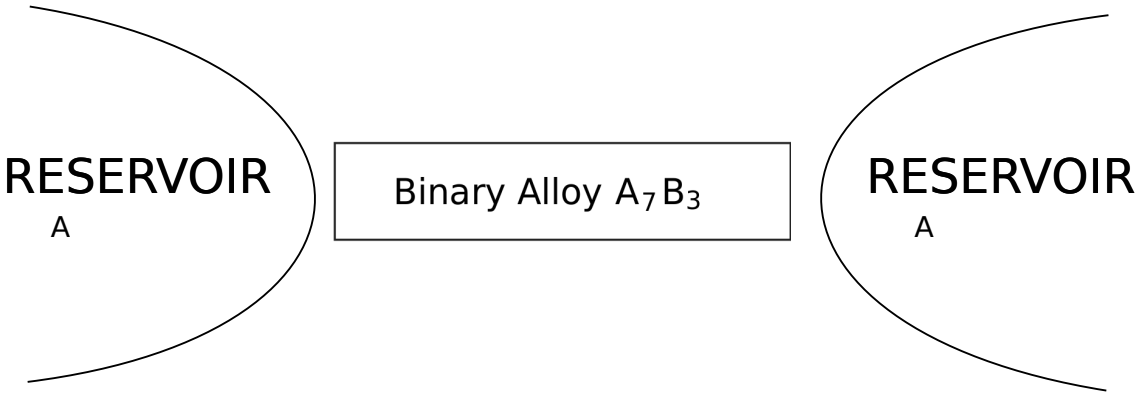

Figure 3.4. A preliminary illustration of a nano-scale junction where the junction is made of thermal dichromator structure.

The binary alloy model, $A_{1-x}B_x$, with the impurity concentration 30%, is used as a dichromator for this work. Specifically, the alloys whose transmission spectra are illustrated with the maroon and brown lines in Fig.3.5 are chosen. The calculated common resonant frequencies of the brown and maroon lines are 12.6742 THz and 8.0583 THz, respectively. In order to both filter random resonant peaks and suppress the contribution of the low-frequency modes to the conductivity, the alloy sizes are extended to 120000 atoms long. For extremely long chains, the perfect transmission peak of the common resonant frequency can deteriorate or completely disappear. In the sub-ballistic region, peaks are more robust to scatter than those of the resonant regime. So, our chosen dichromators have adequately sub-ballistic character. Our chromators select a small portion of the transmission spectrum. The disordered chains block all frequencies except the zero frequency, the common resonant frequency, and their neighbors. For each type of chromator, five distinct atomic configurations whose zero-frequency and the standard resonant frequency give approximately the same contribution to the conductivity are selected to comprehend the barrier effect on ω_{crf} obviously.

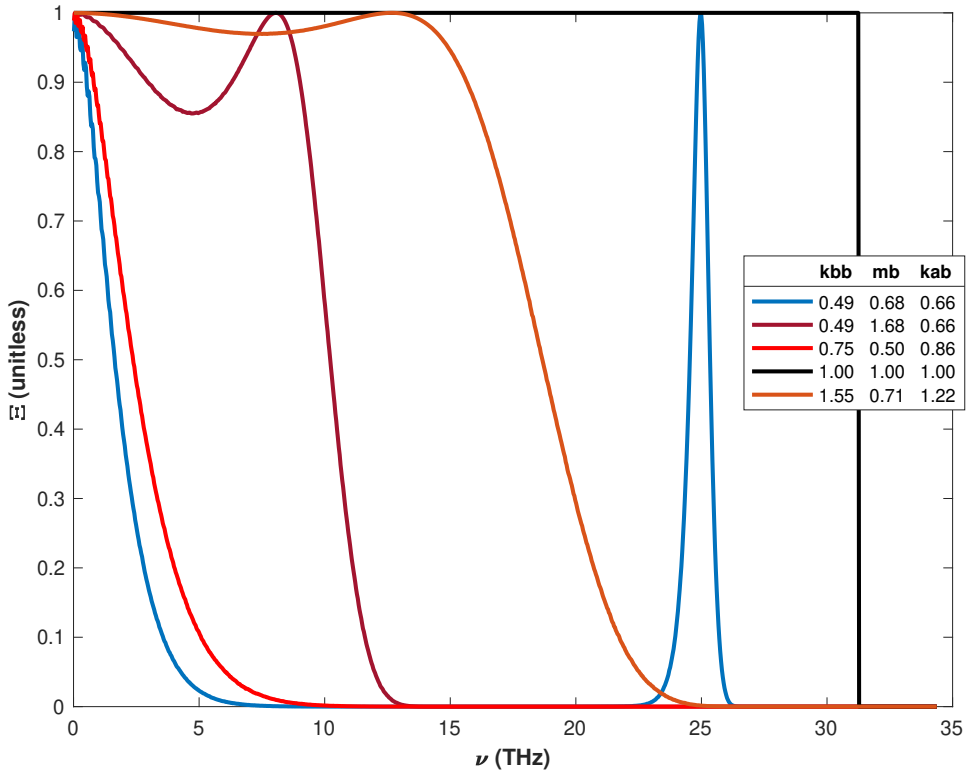

Figure 3.5. The transmissions as a function of frequency for distinctly tuned force constant and masses disorder combinations. Both m_a and Φ_{aa} are equal to 1.0 for all cases. The length of binary alloys is 1000 atoms long, and the impurity concentration is 30%. Transmissions are averaged over 10^5 atomic configurations.

3.2. Numerical Findings

One of the dichromatic systems is adjoined to a phononic gap system and placed between two macroscopic thermal reservoirs to build a tunneling device. The schematic illustration of the device is shown in Fig.3.6. Since the supplement of A atoms at the ends of our chains does not change their transmission, few are placed between the barriers and dichromators to prevent B and C atoms from becoming neighbors. The parameters of barrier systems are selected so that the common resonant frequencies of corresponding dichromators fall inside the phononic gaps of their barriers. The transmissions of the systems are calculated with the NEGF, and the non-linear phonon-phonon interactions are not considered. The transmission spectrums of the dichromator, whose common reso-

nant frequency is 12.6742 THz, and its corresponding phononic gap system are shown in Fig.3.7 to illustrate how their spectra coincidence with each other. The parameters, $\mathbf{\Phi}_{ac}$ and m_c, are set to $0.285\ eV/\text{Å}^2$ and $0.619\ amu$, respectively. The gap extends from 11.8 THz to 15.0 THz. This barrier blocks all the modes within this frequency range. On the other hand, the dichromator gives nominal transmission at all vibrational modes except neighbors of either zero-frequency or its common resonant frequency. Hence, only the lower energy states are common for dichromator and phononic gap systems. The length of the barrier system whose transmission spectrum is shown at the bottom of Fig.3.7 is sufficiently long to open the gap. Compared to entirely random configurations of dichromators, barriers are one-dimensional lattices with a unit cell consisting of one pair of A and C atoms. The discrete levels of the diatomic chain are broadened due to the interactions with reservoirs.

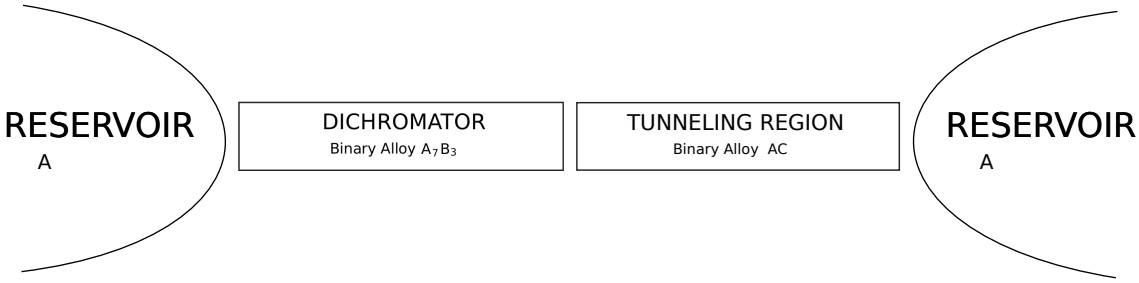

Figure 3.6. Schematic illustration of the phonon tunneling device.

The dependence of transmissions and conductivities on the length of barriers is investigated since evanescent solutions decay with length. Tunneling occurs when the barrier length is sufficiently short to allow penetration of evanescent waves. Placement of the barriers starts with placing one unit cell of the barrier system and continues with adding one unit cell at a time. For each step, we determined the transmission coefficient. As we mentioned before, for each type of dichromator, five different atomic configurations are selected in which the contributions of the zero-frequency and the common resonant frequency to the conductivity are approximately the same. Accordingly, the conductivity values should drop to approximately half above a specific temperature.

The phononic transmission spectrum that belongs to one of the tunneling devices is demonstrated in Fig.3.8 in order to observe the filtering effect that is applied by both dichromators and phononic gap systems to each other. The present dichromator's common resonant frequency is 8.0583 THz, and the corresponding phononic gap falls be-

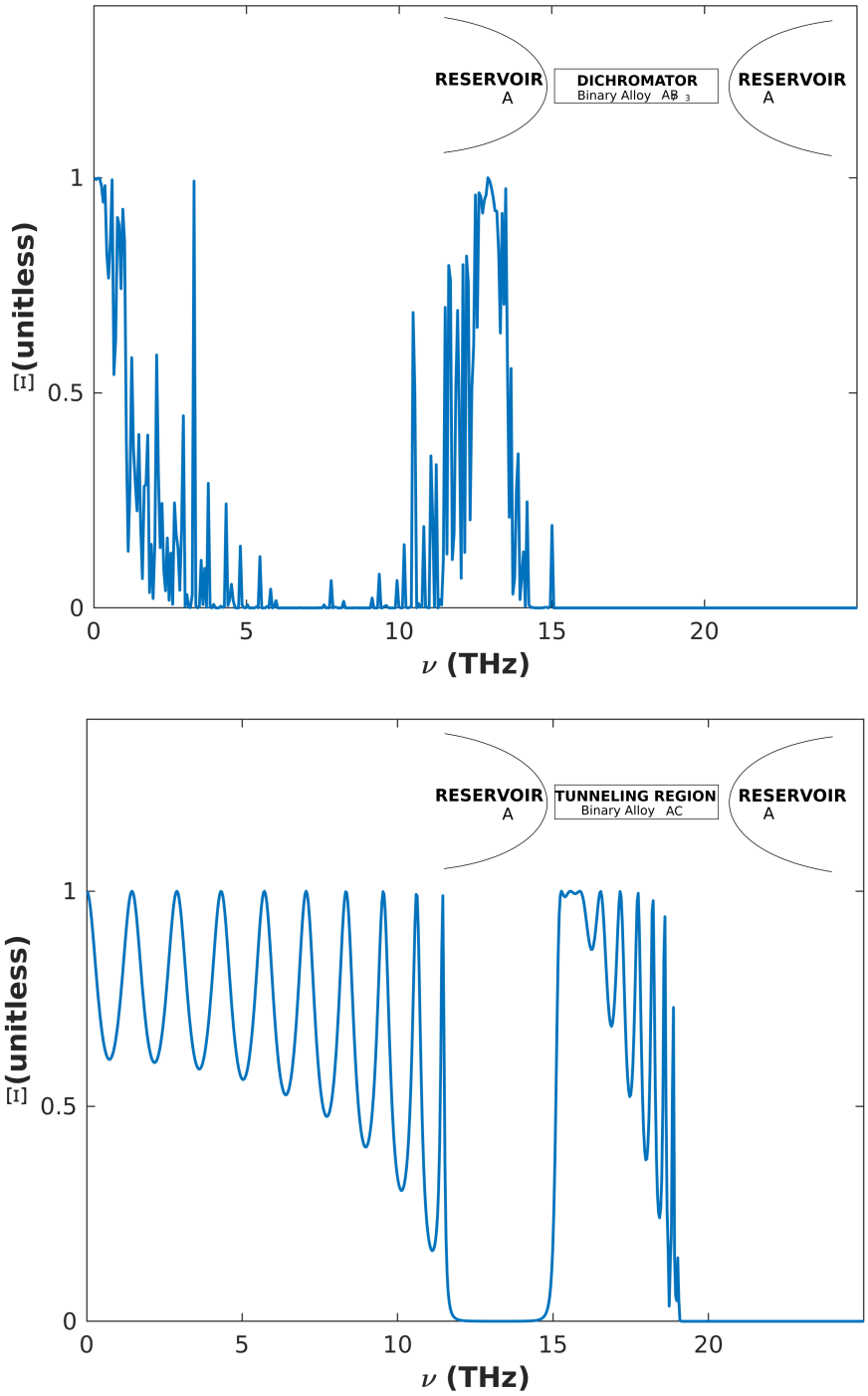

Figure 3.7. The transmission spectra of a dichromator(top) and its corresponding barrier(down). The barrier length is sufficiently long to illustrate the gap distinctly.

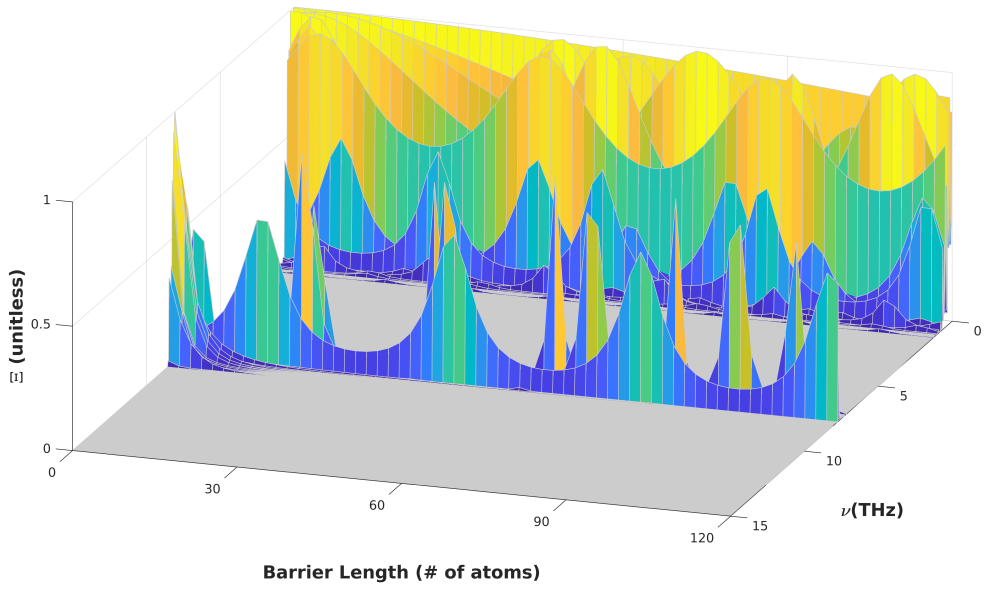

Figure 3.8. The transmission spectrum of a phonon tunneling device.

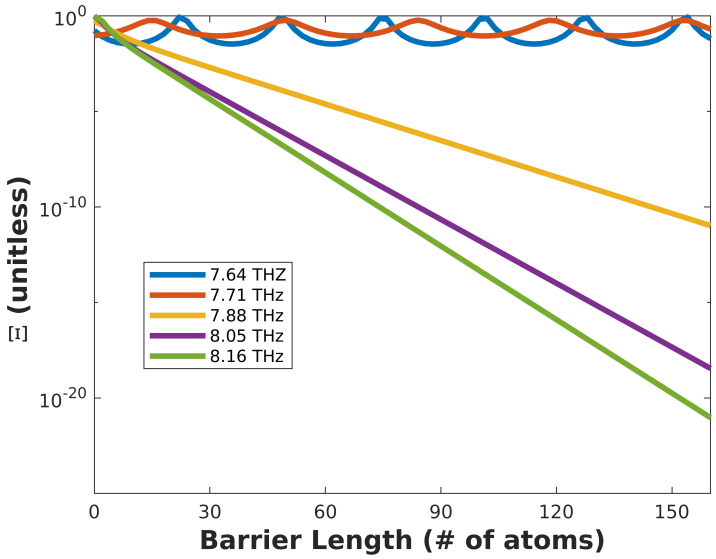

Figure 3.9. The transmission coefficients in logarithmic scale as a length function are plotted for a set of vibrational modes around the resonant frequency of the above system's dichromators.

tween 7.81 THz and 9.37 THz. For this range, the intrinsic parameters, $\mathbf{\Phi}_{ac}(m_c)$, are set to $0.125\ eV/\text{Å}^2$ (0.694) amu. The transmission coefficients of the shared vibrational modes between the dichromator and phononic gap system fluctuate as expected. At the gap, until the barrier length is sufficiently long to prevent tunneling, transmission still occurs due to the penetration of evanescent waves through the barrier. Exponential decays of the transmission coefficients with length are evidence of tunneling. Consequently, the conductivity is expected to be enhanced at a sufficiently small thickness of the phononic gap system. Moreover, the filtering effect of the dichromator can be observed from the spectrum. It stops all the vibrational modes except those neighbors of either the zero-frequency or 8.0583 THz. For a set of vibrational modes from neighbors of the common resonant frequency, the transmissions in logarithmic scale as a function of barrier length are plotted in Fig.3.9. The modes indicated by the blue and red lines are common for both the dichromator and the barrier, and the other three are forbidden because they fall inside the gap. While the transmissions of forbidden modes decay with barrier length, transmission coefficients of the common modes exhibit Fabry-Perot oscillations with the length, and either oscillations' periods or oscillations' amplitudes are diverse.

When the transmission coefficient is calculated considering only harmonic interactions, quantum effects do not come into play. Therefore, an identical value is obtained whether the method is based on classical or quantum mechanics. Thermal conductance values are calculated via the Landauer formula with both the Bose-Einstein and the Maxwell-Boltzmann distribution functions to see the effect of statistics on the tunneling mechanism. Consequently, we verify that the tunneling phenomenon is not purely quantum mechanical; instead, it is also performed by classical waves.

The length dependence of thermal conductivity is investigated to relate the tunneling effect on a measurable quantity. Conductivities, which are calculated with the Bose-Einstein distribution function, are demonstrated in Fig.3.10. Calculations are performed at three different temperatures. The figures are arranged from top to bottom according to their calculation temperatures. The top, middle, and bottom graphs introduce conductivities of 100 K, 300 K, and 1000 K, respectively. In all, conductivity is on a logarithmic scale. The different line styles indicate the dichromator types, while colors characterize the different atomic configurations. The dot-dashed lines indicate the chromator whose common resonant frequency is 8.0583 THz, and the dashed lines represent the chromator whose common resonant frequency is 12.6742 THz. The insets point to the conductivity drops because ten-atom-long barriers have sufficient length to prevent tunneling. The atomic configurations characterized by the same intrinsic parameters

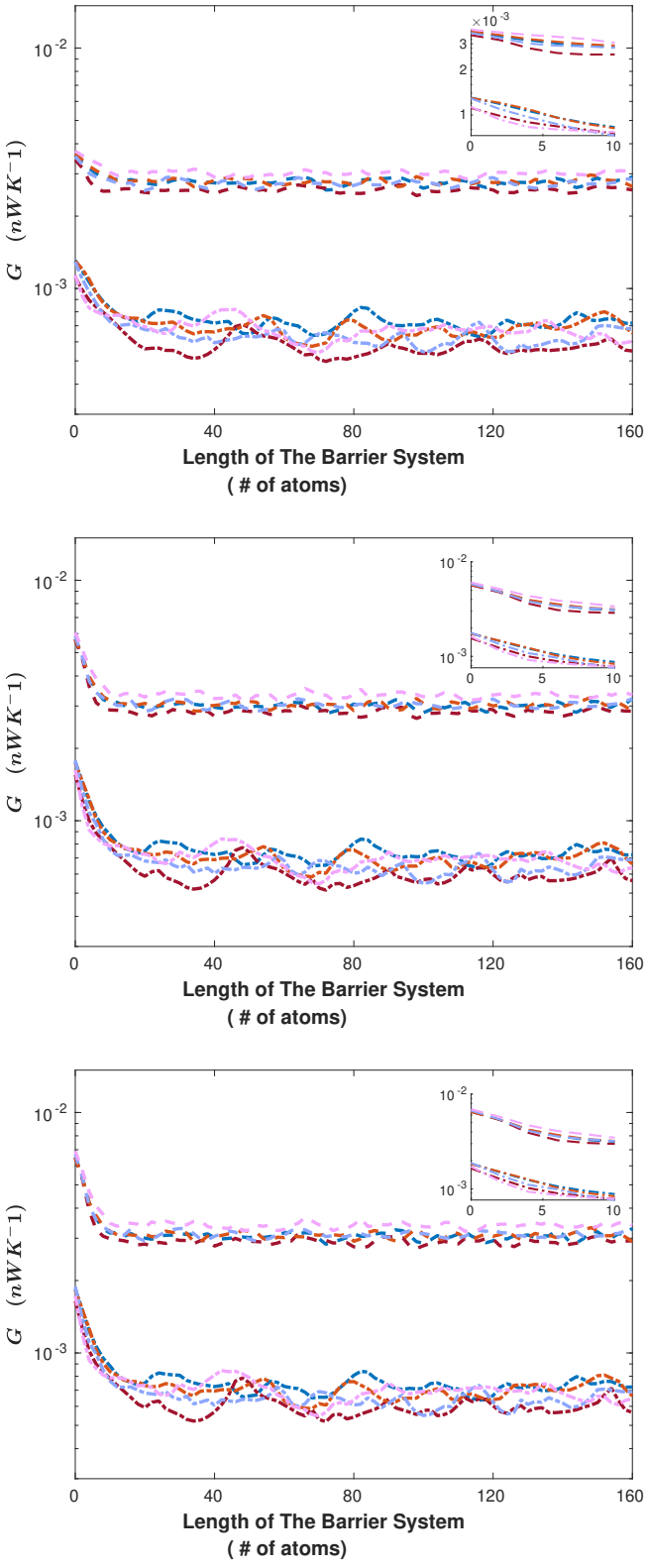

Figure 3.10. Conductivities which are calculated with the Bose-Einstein distribution function at 100 K (top), 300 K (middle), and 1000 K (bottom).

give roughly comparable conductivities. The conductivities of devices in which the used chromator's common resonant frequency is 12.6742 THz are higher than that of the others since chromators have higher force constant and lighter atoms. The fluctuations of the conductivities originate from the Fabry-Perot oscillations in transmission coefficients. They are more distinct in the devices whose dichromator's resonant frequency is 8.0583 THz since this chromator's transmission peak is narrower than the transmission peak of the other chromator due to the higher difference between the multiplications $\Phi_{aa}m_a$ and $k_{bb}m_b$. When the chromator's peaks are broader, more vibrational modes are common for the dichromator and barrier; hence, the fluctuations are averaged out.

When the distribution function is the Bose-Einstein function at absolute temperature, the zero-frequency modes dominates the thermal conductivity because, at low temperatures, low energetic vibrational modes contribute to the conductivity. Hence, conductivity is insensitive to either the barrier system's presence or extension. However, with the temperature rise, the contribution from the common resonant frequency incrementally increases, and conductivity increases. The highest decrease due to tunneling occurs at 1000 K. Conductivities drop within the range between 50% and 70%. Moreover, a considerable drop in conductivity is still possible at room temperature.

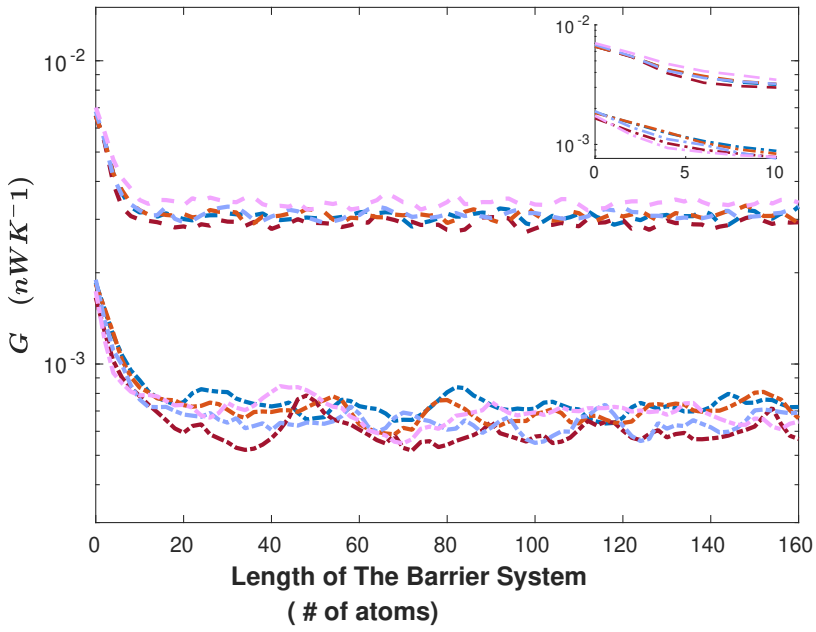

Figure 3.11. Conductances which are calculated with the classical distribution function. When the Maxwell-Boltzman governs the distribution, conductances are independent of temperature.

The conductivities determined with the Maxwell-Boltzmann distribution function are plotted in Fig.3.11. In this figure, the same color and style code with Fig.3.10 is applied. When statistics is classical, conductivities are independent of temperature. Since at sufficiently high temperatures, the behavior of quantum mechanical weight function is similar to that of classic mechanical one, the conductivity values are similar. When Fig.3.10 and Fig.3.11 are carefully compared, the values are approximately the same, and considerable drops in conductivities with length are observable.

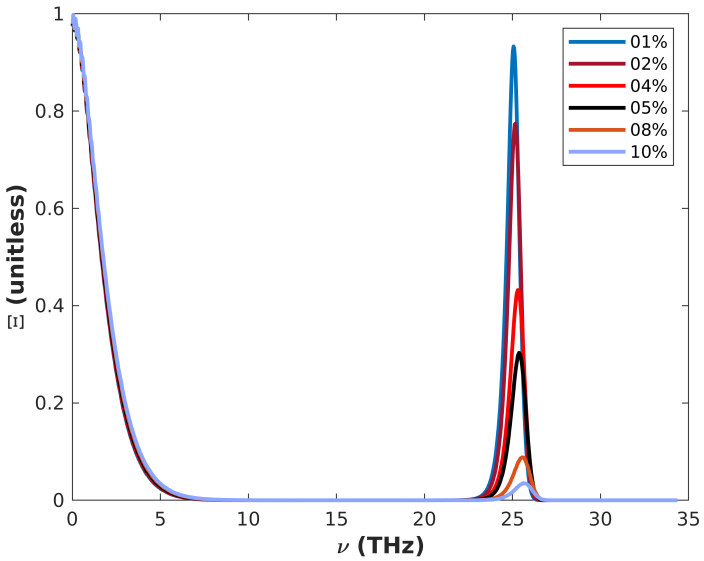

Figure 3.12. The illustration shows the robustness of the common resonant transmission peak against deviations in Φ_{ab} value from the harmonic condition. Both m_a and $\mathbf{\Phi}_{aa}$ are equal to 1.0 .

The endurance of perfect transmission at common resonant frequency against deviations in Φ_{ab} value from the harmonic average of Φ_{aa} and Φ_{bb} was investigated in order to reveal the possibility of construction a phonon tunneling device. In the fig.3.12, transmissions calculated for a set of deviated k_{ab} values are demonstrated. For this reason, the system, indicated by the blue line in Fig.3.5, is chosen. Again, transmissions are average over 10^5 random atomic configurations. Transmission is not unity for slight deviations, but 10 percent to 20 percent drops are acceptable and do not prevent the observation of phonon tunneling. The transmission value decreases to half when the deviation is around 4%. However, the resonant transmission peak completely disappears when the k_{ab} value deviates more than 10% from the harmonic average.

To conclude, this chapter presented a toy model of a phonon tunneling device

based on the bridge structure. Tunneling is an exotic phenomenon displayed by all waves and quantum mechanical particles. Due to the advances in probing the nano-scale heat transfer, with this presented phonon tunneling device, phonon tunneling is expected to be observed. This device comprises a phononic gap system as a barrier, and a phononic dichromator filters incoming phonons. The gap is arranged so that one of the incoming frequencies of the dichromator falls inside the gap. At sufficiently short lengths of the barrier, thermal conductivity is enhanced due to the phonon tunneling. Conductivity is considerably decreased, like 50% and 70% , when the barrier length is sufficient to prevent tunneling completely.

CHAPTER 4

THE SIGNIFANCE OF QUANTUM EFFECTS ON THERMAL CONDUCTIVITY OF AMORPHOUS GRAPHENE

Quantum mechanics comes into play in determining the thermal conductivity of materials in two ways. The first is the effect of phonon occupancy factors on transport, and the second is the role quantum mechanics plays in determining the magnitudes of self-energies arising from multiple phonon scattering in anharmonic processes. In many materials, these effects can be neglected at room temperature so that classical molecular dynamics simulations can give good enough results on the thermal conductivity of materials. However, systems with high Debye temperatures, such as graphene, should be carefully studied. In this study, we investigate the thermal conductivity of amorphous graphene by adapting the Landauer transport formulation to phonon transport. Since multiple phonon scattering is suppressed in the amorphous system, it is studied in the harmonic limit. For this section, structures are created by amorphization in the middle of the 14 nanometer-long graphene. The width of the graphene is 10 nanometers long. The 8-angstrom long regions of the structures from the right and left were fixed. Therefore, buffer zones have been placed between the right and left reservoirs and the device; see Fig.4.1.

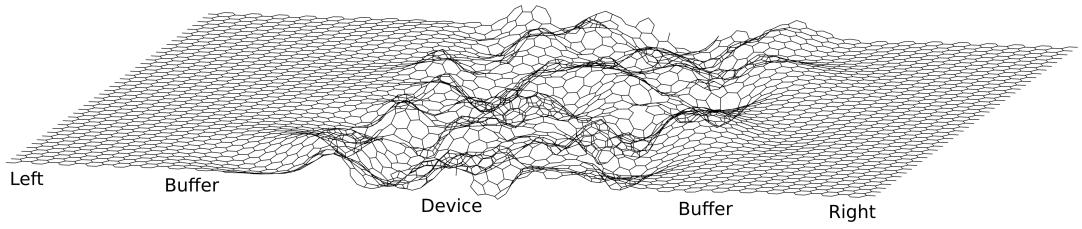

Figure 4.1. The partition of the structure as the left, the device, and the right system is shown.

We have chosen configurations with the same q3 parameter from each type of device region to compare thermal properties. All picked structures are shown in the ap-

pendix. Mass-normalized dynamical matrices of selected systems are obtained by the finite difference method as it is implemented in the LAMMPS package. This step adapts the optimized Tersoff potential parameter to characterize the interatomic potentials.[139] Non-Equilibrium Green's Functions are applied to obtain transmissions. Phonon transmission is calculated by $\Xi = trace[\Gamma_l G_d \Gamma_r G_d^\dagger]$. From transmissions, conductivities are determined with the Landauer formula. Assuming that $\Delta T \rightarrow 0$, namely equilibrium transport, conductivity is defined as

$$\kappa = \frac{G * L}{A} = \frac{L}{A}\frac{J}{\Delta T} = \frac{L}{2\pi A}\int d\omega\ \hbar\omega\ \Xi(\omega)\ \frac{\partial f}{\partial T} \tag{4.1}$$

where f is the distribution function and A is the cross sectional area. We determined thermal conductivities with two distribution functions: Bose-Einstein and Maxwell-Boltzman distribution function, $f_{cl}(\beta, \epsilon) = 1/\beta\,\epsilon$.

In the harmonic approximation, the transmission function does not change under the interchange of mechanics between classical and quantum. So, this work focuses on the effect of alternating the distribution function from classical to quantum mechanics on thermal transport properties. The nobility of this work, classical and quantum mechanical thermal conductivities, can be determined within one scheme.

The calculated vibrational density of states within Green's functions scheme can be seen in Fig.4.2. Despite the differences in both configuration type and q3, the density of states shows a similar character. Correspondingly, the density of states is in agreement with the existing literature. The transmissions are shown in Fig.4.3. Colors characterize the device type. We used red for the 3CGM type, black for the 3C type, and blue for the NC type; this color code is applied to all figures. Solid lines indicate configurations with a q3 parameter of 0.70, dotted lines indicate structures with a q3 parameter of 0.50, and lines with diamonds demonstrate the arrangements with a q3 parameter of 0.40. The first thing to notice when looking at the transmission graphs is that the transmission values decrease as the q3 parameter decreases. While high-energy phonons were most affected by the defects, acoustic modes that are difficult to scatter are less affected by the disorders, regardless of the q3 parameter and the device type. The effect of the absence of three- and four-membered rings is negligible. Irrespective of the q3 parameter, 3CGM and 3C transmissions seem very close. The NC device configuration scatters phonons with moderate energies more than the other two due to the absence of voids and coordination defects. However, in optical and acoustic phonons, the change of configuration type has a minor effect on their transmission.

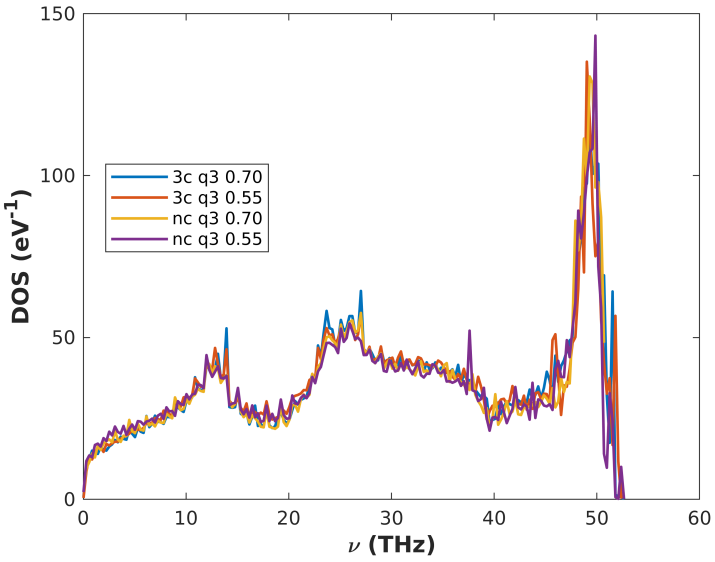

Figure 4.2. The vibrational Density of States of amorphous graphene with different phases and amorphousness degree.

Thus far, all our calculations were common to classical and quantum mechanics. For the impact of classical and quantum mechanical statistics on thermal transport properties, we stated that we calculated the conductivity for two different distribution functions. The obtained conductivities are seen in Fig.4.4. The dashed lines demonstrate the conductivities, which are calculated with classical statistics. The solid lines indicate the conductivities, which are computed with Bose-Einstein statistics. We used the same color and line code for the devices' types and the q3 parameters. As seen in the conductivity figure, there are considerable disparities between classical and quantum mechanical thermal conductivities. As with heat capacity, we expect this disparency between classical and quantum mechanics to disappear at higher temperatures. Since the Debye temperature of graphene is 1813 K[206], we see that the apparent distinction does perish at about those temperatures. Since we're not dealing with high temperatures, we plotted conductivities up to 500 K to inspect temperatures around room temperature. Further, a slight variance between conductivities belonging to different device types with the low q3 parameter is observed. So, we can deduce the absence of three- and four-membered rings has almost no impact on thermal conductivities, and voids and coordination defects have a bare influence when the structure has a high disorder.

Additionally, the calculated conductivities at 300 K and their proportions are listed in table 4.1. Conductivities lower with decreasing q3 parameters as transmissions since

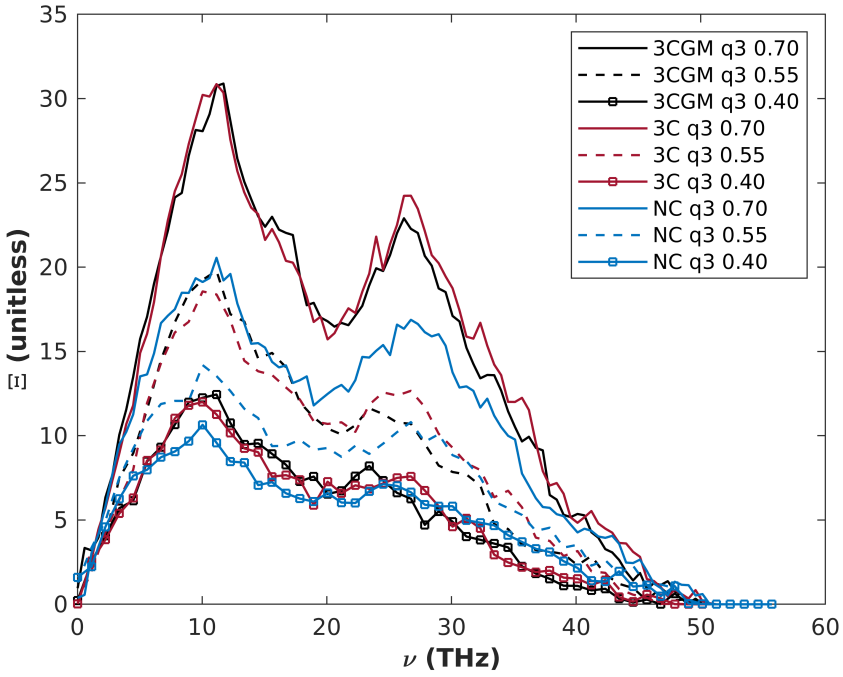

Figure 4.3. Transmissions for different values of q3 and device types. The black, red, and blue lines demonstrate 3CGM, 3C, and NC device types. Lines are dotted(marked with diamonds) to indicate the configurations with q3 = 0.55(0.40).

Table 4.1. The conductivity values and their proportions determined at 300 K.

		Conductivity $(W(mK)^{-1})$		
Device Type	q3	Canonical Ensemble	Quantum Mechanical	Proportion
3CGM	0.70	18.48	9.48	1.95
	0.55	10.77	6.04	1.79
	0.40	6.86	4.02	1.74
3C	0.70	18.93	9.46	1.96
	0.55	10.88	5.92	1.78
	0.40	6.74	3.79	1.74
NC	0.70	14.08	6.98	2.02
	0.55	9.58	4.97	1.93
	0.40	6.74	3.55	1.89

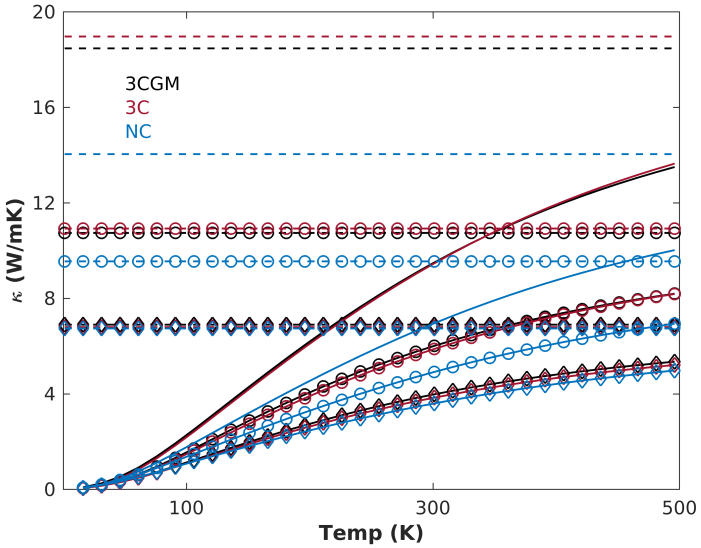

Figure 4.4. Conductivities. The dashed lines demonstrate the conductivities, which are calculated with classical statistics. The solid line shows the conductivities calculated with the Bose-Einstein distribution function. Except this, the line and color codes are the same as the transmission figure.

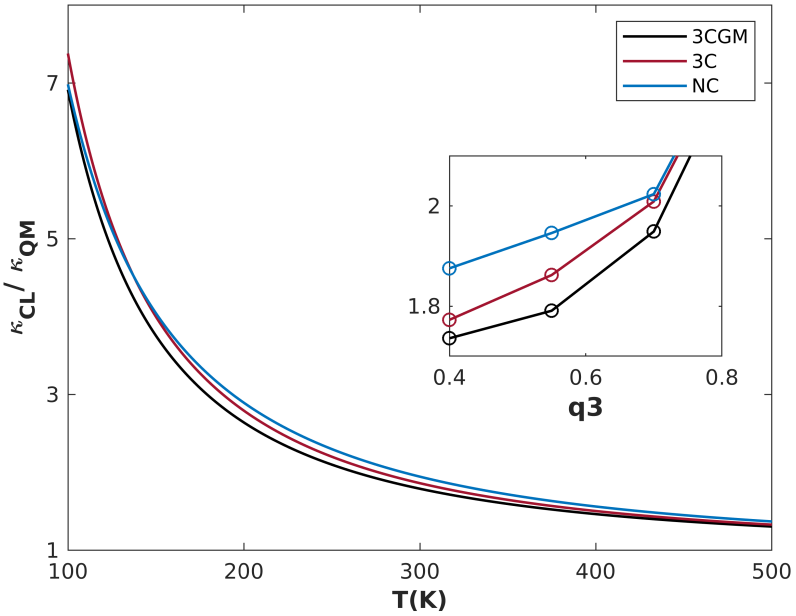

Figure 4.5. The proportions vs. the local bond order parameter, q3. The inset shows the proportions against temperature.

lower q3 means more disorder, thus stronger resistance to heat flow. Moreover, the discrepancies between classical and quantum mechanical conductivities get smaller with lower q3 parameters. However, even at its high amorphous degree, classical mechanics overestimates thermal conductivity by almost 80 percent. To deeply investigate the dependence of the proportion on amorphousness degree, we plot the ratios as a function of temperature as shown in Fig.4.5. At low temperatures, the prediction of classical mechanics is almost five times greater than quantum mechanical conductivities since classical mechanics excite all vibrational modes regardless of the temperature, while quantum mechanics excite vibrational modes according to the ambient temperature. So, the difference gets larger with the decreasing temperature. The inset of Fig.4.5 shows proportions as a function of the q3 parameter. The ratio lifted significantly for all device types with lower amorphousness degrees. NC device configurations give slightly higher proportions than the other two types due to stronger scattering to phonons with moderate energies.

4.1. Size Dependence

The thermal conductivity values and the proportions presented in the previous section must be independent of the length. We showed that our results are independent of size by repeating our transmission and conductivity calculations with two other dimensions, longer and shorter than the structure we used in the previous section. The device lengths of the systems whose results are exhibited in the central part are 4.0 nanometers. While the device length of the configurations we call short is 1.6 nm, the distance of the devices we call long is 7.5 nanometers. All chosen structures are printed on the supplementary material. The width of all systems is 10 nm. Calculations for this purpose were made only for the 3CGM device type. The structures we created for this purpose can be seen in Fig.A5-A6. Transmission and conductivity calculations are only reproduced for the configurations of 0.70 and 0.55 q3 parameters. We demonstrated the transmission figures in a simpler view by grouping these two q3 parameters in a separate graph (Fig.4.6). The blue lines are for perfect graphene($10\text{x}14$ nm^2); the green, black, and orange lines indicate the systems with lengths $1.6, 4.0, 7.5$ nm. The higher the phonon frequencies, the more they are affected by the distortions in the structure. As the length of the device increases, the transmission values of all modes decrease even though the systems have the same q3 parameter; significantly, the scattering of medium-energy frequencies increases. The last figure shows the conductivity values. Again, black, green, and orange line colors indicate the configurations with device lengths of $4.0,\ 1.6$, and 7.5 nm. The dashed lines

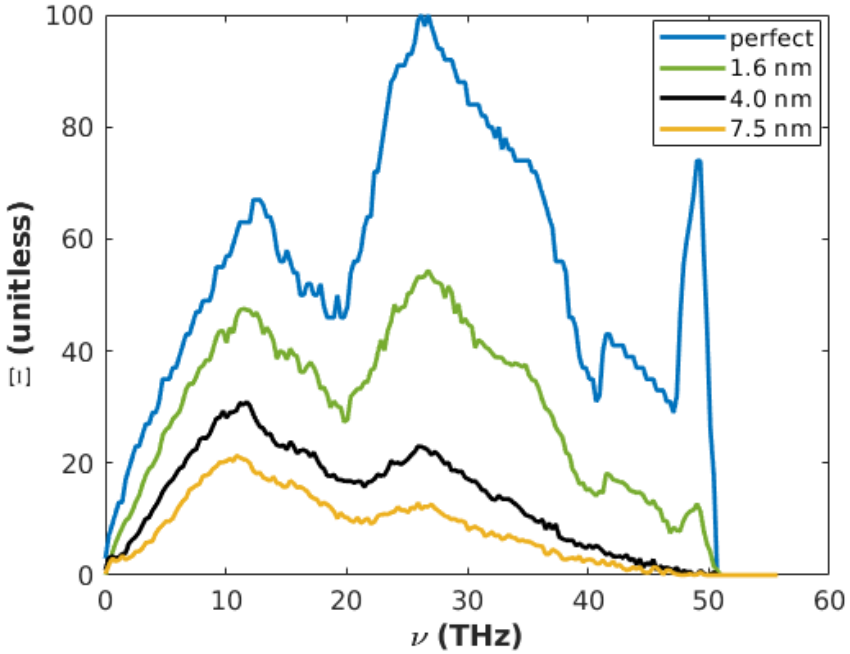

(a) q3: 0.70

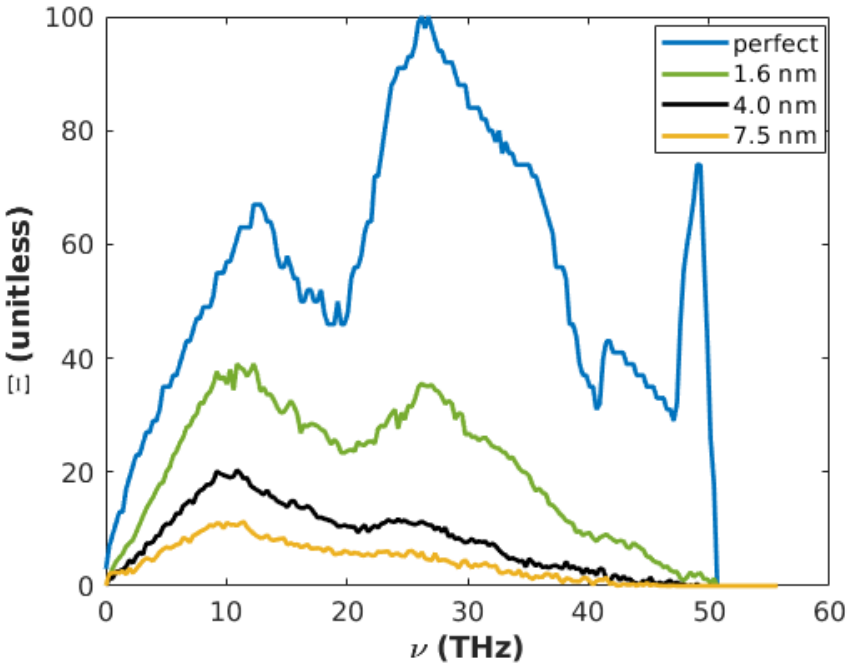

(b) q3: 0.55

Figure 4.6. Transmission figures for systems with different device lengths and the same q3 parameter.

are for classical thermal conductivities, and the dotted lines are for the configurations with $q3 = 0.55$. Slight differences in conductivity are observed, but even though structures have the same q3 parameter, the differences in the structure's atomic details lead to slight differences in conductivity. Nevertheless, when the values are carefully examined, the results demonstrate thermal conductivity values are independent of system size, as expected.

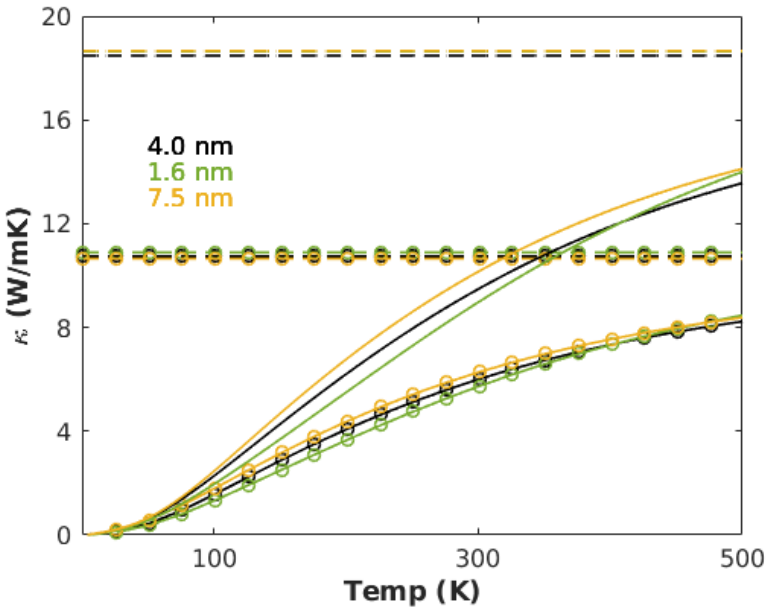

Figure 4.7. Thermal conductivity values as a function of temperature.

4.2. Kubo-Greenwood Results

One issue that can arise from using Green's functions method is the interface effect on thermal conductivity. Kapitza resistance occurs when a carrier crosses an interface. [207] Due to the amorphous and crystalline phases having different resistivities to the heat carriers, the overall structure can cause Kapitza resistance. Another issue can be the length of the device region. If it remains smaller than the mean free path, diffusion may not occur, and carriers that have a diffusional profile may show a ballistic character. The Kubo-Greenwood method can handle much larger structures than Green's functions. The decimation technique can help the size issue, but increasing the width can still be challenging since the block size will increase with the increasing width. Consequently,

we validate our results with the Kubo-Greenwood method, which is free from size and interface issues.

We have chosen the 3C type configuration with q3=0.70 since the presence of three- and four-membered rings have a bare impact on conductivities; we can compare 3CGM and 3C structures. Now, our structure is $25\text{x}25$ nm^2. According to Green's functions results, we estimated the average mean free path to be approximately 4-5 nm for configurations with q3=0.70. So, our sample size is much larger than to uncover whether there is a size issue. The calculated mean free paths are shown in Fig.4.8, and the inset demonstrates the transmission values calculated from the mean free paths via $\Xi(\omega) = N_{ch}(\omega)/(1 + L/\text{mfp}(\omega))$. Mean free path values are closer to the estimated value. We also have estimated the average mean free path for q3=0.40, approximately 1 nm. So, we expect this value to be a quite good approximation. Moreover, when the transmission values of configurations with q=0.70 (Fig.4.6a) are examined, it is observed that the transmission of the structure with a length of 7.5 nm is reduced to one-fifth of that of the perfect one. The values shown in the inset show more reduction in the transmission, as it should be. When the device increases from 1.6 nm to 4.0 nm, the transmission values decrease significantly more than when the device increases from 4.0 nm to 7.5 nm. Consequently, the device with the 1.6 nm length is below the mean free path.

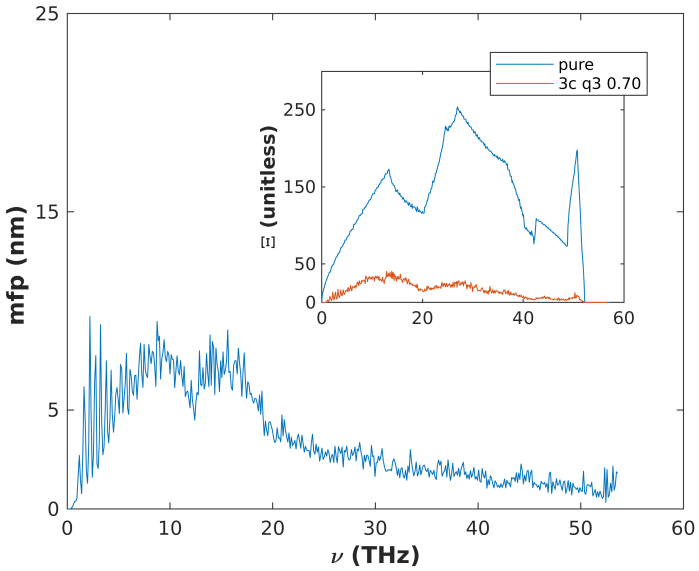

Figure 4.8. Mean free paths of 3C configuration with q3=0.70. The system size is $25\text{x}25$ nm^2. The inset demonstrates the transmissions of pristine and amorphous phases.

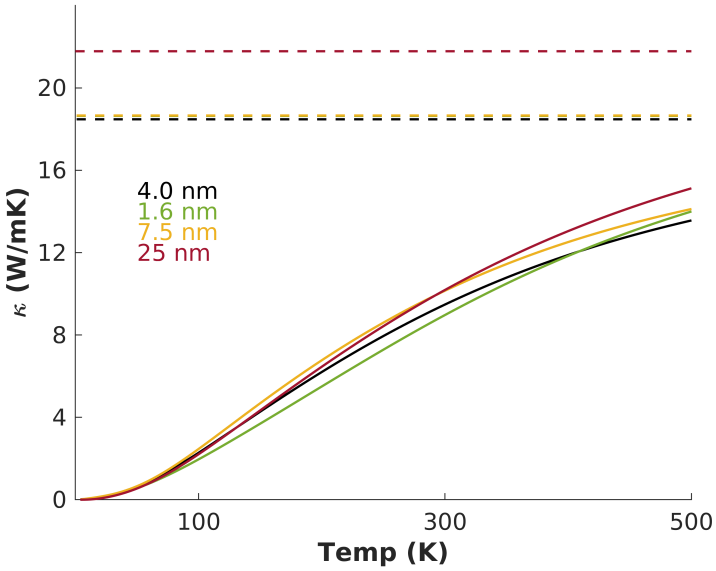

Figure 4.9. Thermal Conductivities of Configurations with q3=0.70. The dashed(solid) lines demonstrate the classical (quantum) conductivities. The 25 nm long configuration is calculated with the Kubo-Greenwood method, while the Green's functions method is applied to others.

The thermal conductivity has also been plotted in Fig.4.9. Here, we have plotted the thermal conductivity with the q3=0.70 configurations from the previous section for a clean comparison. The conductivities are in quite good agreement at low temperatures, while Kubo Greenwood gives higher values at high temperatures. This shows that the Kapitza resistance may have been realized for high-frequency carriers. The interface resistance must be at high-frequency carriers, as there is almost no difference between the quantum thermal conductivities, while the classical thermal conductivity is higher than the Kubo-Greenwood calculation of Green's functions. We made this estimation only quantitatively, so this situation needs more work to estimate interface resistance qualitatively. Still, although there is no ensemble average in our computations, the fact that we get almost the same results with two different methods indicates that our analyses are concrete. With the Kubo-Greenwood results, the classical quantum proportion has increased additionally. These results show that in amorphous materials, where the scatterings due to the interaction between the carriers are suppressed due to the high disorder of the internal structure of the system and where the scatterings due to the deterioration of the internal network are the dominant scattering mechanism, quantum thermal conductivity is deterministic if also the material has high Debye temperature.

Lastly, no plateau region was observed in the temperature-dependence behavior of the thermal conductivities with either method. Henry also did not observe a plateau region in his study of amorphous carbon films.[27] Whether this is due to the amorphous carbon structure or our methods or dimensions requires further investigation. Jund and Julian did not observe a plateau region in thermal conductivity calculations of amorphous SiO_2 until they introduced finite-size correction.[208] Moreover, the literature needs a measurement of the thermal conductivity of two-dimensional amorphous carbon monolayers to reveal this situation.

CHAPTER 5

CONCLUSION

An essential pillar of technological development is discovering materials with functional properties. One way to do this is to tune the properties of materials by controlling the irregularities within them. A specific example of this is the creation of a phononic dichromator using the intrinsic cooperation of impurity atoms. If the common resonant frequency of the dichromator is tuned to coincide with the stop band of the phononic gap material, and the length of the phononic gap material is short enough, tunneling phenomena can be observed. This work links the tunneling phenomenon to a measurable physical property, thermal conductivity. Our calculations show a significant decrease in thermal conductivity when the size of the gap system reaches a sufficient length to prevent tunneling. This property could pave the way for us to develop systems that would allow us to construct devices that are based on phonon tunneling. Similarly, frequency-specific stress sensors can be designed if our toy model becomes a reality. Moreover, we show tunneling is not only a quantum phenomenon but can also occur classically. The only factor that made our analysis quantum mechanical is the Bose-Einstein distribution. So, when the classical distribution governs the distribution function, our analysis is classic mechanical, and the phonon tunneling effect on thermal conductivity is still observable. This shows that the tunneling phenomenon is purely quantum mechanical and can be performed by classical waves.

Quantum effects can affect thermal conductivity in two ways. One is through phonon statistics, and the other is through phonon-phonon interactions. However, phonon scattering due to internal structure disorder is the dominant scattering mechanism in heavily disordered materials. Therefore, the only quantum effects involved in the thermal conductivity of these materials are due to statistics. In this study, we derive the Maxwell-Boltzman distribution function instead of the Bose-Einstein distribution function and calculate the classical and quantum thermal conductivity of amorphous graphene using the Landauer formulation. Thus, the classical thermal conductivity can also be estimated using the Landauer formulation with this developed distribution function. In addition, classical thermal conductivity agrees with existing studies in the literature. Nonetheless, since this material has a high debye temperature, quantum effects were expected to be significant even at room temperature. The results show that the thermal conductivity

calculated using the classical distribution function is about two times higher than the quantum thermal conductivity. This disparity increases with the decreasing temperature, and these results support Henry's findings, which establish approximately ten times lower at lower temperatures when he includes quantum corrections in thermal conductivity.[27]

Finally, as mentioned in the introduction, the plateau region has emerged in the temperature dependence of the thermal conductivity of some three-dimensional amorphous materials. Whether this is a general rule of thumb for all amorphous materials is debatable. Plateau regions are observed at very low temperatures. This indicates that the plateau region can only be observed in quantum mechanical thermal conductivity calculations. Although our calculations are quantum mechanical, we did not observe any plateau region in the temperature dependence of the thermal conductivity of amorphous graphene. Whether this is a size effect or not requires further work.

REFERENCES

[1] Natasha Dropka and Kevin-Peter Gradwohl. Crystal growth, bulk: theory and models. In *reference module in materials science and materials engineering*. Elsevier, 2022.

[2] Arkadiy Simonov and Andrew L. Goodwin. Designing disorder into crystalline materials. *Nature Reviews Chemistry*, 4(12):657–673, 2020.

[3] Yanwen Zhang, Yuri N. Osetsky, and William J. Weber. Tunable chemical disorder in concentrated alloys: defect physics and radiation performance. *Chemical Reviews*, 122(1):789–829, 2022.

[4] Sergei D. Baranovskii, Alexey V. Nenashev, Dirk Hertel, Florian Gebhard, and Klaus Meerholz. Energy scales of compositional disorder in alloy semiconductors. *ACS Omega*, 7(50):45741–45751, 2022.

[5] David Rohlig, Eduard Kuhn, Angela Thranhardt, Thomas Otto, and Thomas Blaudeck. The role of disorder in elementary photonic components. In *2022 Smart Systems Integration (SSI)*, pages 1–3, 2022.

[6] Efstratia N. Sgourou, Yerasimos Panayiotatos, Ruslan V. Vovk, and Alexander Chroneos. Toward defect engineering strategies to optimize energy and electronic materials. *Applied Sciences*, 7(7):674, 2017.

[7] K S Siegert, F R L Lange, E R Sittner, H Volker, C Schlockermann, T Siegrist, and M Wuttig. Impact of vacancy ordering on thermal transport in crystalline phase-change materials. *Reports on Progress in Physics*, 78(1):013001, 2014.

[8] Giorgio Giuffredi and Fabio Di Fonzo. Disorder engineering in transition metal dichalcogenides toward efficient high current density reduction electrocatalysts. *Current Opinion in Electrochemistry*, 25:100639, 2021.

[9] Xiaolong Zou and Boris I. Yakobson. An open canvas 2d materials with defects, disorder, and functionality. *Accounts of Chemical Research*, 48(1):73–80, 2015.

[10] Jun Xiong, Jun Di, Jiexiang Xia, Wenshuai Zhu, and Huaming Li. Surface defect engineering in 2d nanomaterials for photocatalysis. *Advanced Functional Materials*, 28(39):1801983, 2018.

[11] R. Zallen. *The physics of amorphous solids*. Physics textbook. Wiley, 1983.

[12] W. H. Zachariasen. The atomic arrangement in glass. *Journal of the American Chemical Society*, 54(10):3841–3851, 1932.

[13] Zbigniew H. Stachurski. On structure and properties of amorphous materials. *Materials*, 4(9):1564–1598, 2011.

[14] D. Adler, B.B. Schwartz, and M.C. Steele. *Physical properties of amorphous materials*. Institute for amorphous studies series. Springer US, 2013.

[15] Z.H. Stachurski. *Fundamentals of amorphous solids: structure and properties*. Wiley, 2014.

[16] Avishek Kumar, Mark Wilson, and M F Thorpe. Amorphous graphene: a realization of zachariasen's glass. *Journal of Physics: Condensed Matter*, 24(48):485003, 2012.

[17] Chee-Tat Toh, Hongji Zhang, Junhao Lin, Alexander S. Mayorov, Yun-Peng Wang, Carlo M. Orofeo, Darim Badur Ferry, Henrik Andersen, Nurbek Kakenov, Zenglong Guo, Irfan Haider Abidi, Hunter Sims, Kazu Suenaga, Sokrates T. Pantelides, and Barbaros Ozyilmaz. Synthesis and properties of free-standing monolayer amorphous carbon. *Nature*, 577(7789):199–203, 2020.

[18] Won-Jae Joo, Jae-Hyun Lee, Yamujin Jang, Seog-Gyun Kang, Young-Nam Kwon, Jaegwan Chung, Sangyeob Lee, Changhyun Kim, Tae-Hoon Kim, Cheol-Woong Yang, Un Jeong Kim, Byoung Lyong Choi, Dongmok Whang, and Sung-Woo Hwang. Realization of continuous zachariasen carbon monolayer. *Science Advances*, 3(2):e1601821, 2017.

[19] Paras, Kushal Yadav, Prashant Kumar, Dharmasanam Ravi Teja, Sudipto Chakraborty, Monojit Chakraborty, Soumya Sanjeeb Mohapatra, Abanti Sahoo, Mitch M. C. Chou, Chi-Te Liang, and Da-Ren Hang. A review on low-

dimensional nanomaterials: nanofabrication, characterization and applications. *Nanomaterials*, 13(1):160, 2023.

[20] Zhengdi Wang, Tingting Hu, Ruizheng Liang, and Min Wei. Application of zero-dimensional nanomaterials in biosensing. *Frontiers in Chemistry*, 8, 2020.

[21] Subrata Pandit, Pradipta Behera, Jagabandhu Sahoo, and Mrinmoy De. In situ synthesis of amino acid functionalized carbon dots with tunable properties and their biological applications. *ACS Applied Bio Materials*, 2(8):3393–3403, 2019.

[22] Yibo Yan, Jun Gong, Jie Chen, Zhiping Zeng, Wei Huang, Kanyi Pu, Jiyang Liu, and Peng Chen. Recent advances on graphene quantum dots: from chemistry and physics to applications. *Advanced Materials*, 31(21):1808283, 2019.

[23] Chengli Zhang, Junlin He, Yuchan Zhang, Jun Chen, Yilin Zhao, Yazhen Niu, and Chao Yu. Cerium dioxide-doped carboxyl fullerene as novel nanoprobe and catalyst in electrochemical biosensor for amperometric detection of the cyp2c19*2 allele in human serum. *Biosensors and Bioelectronics*, 102:94–100, 2018.

[24] Jiemei Ou, Huijun Tan, Zhong Chen, and Xudong Chen. Fret-based semiconducting polymer dots for ph sensing. *Sensors*, 19(6), 2019.

[25] P. Bhattacharya, R. Fornari, and H. Kamimura. *Comprehensive semiconductor science and technology*. Elsevier Science, 2011.

[26] J.-S. Wang, J. Wang, and J. T. Lü. Quantum thermal transport in nanostructures. *The European Physical Journal B*, 62(4):381–404, 2008.

[27] Lv Wei and Henry Asegun. Phonon transport in amorphous carbon using greenkubo modal analysis. *Applied Physics Letters*, 108(18):181905, 2016.

[28] A. Beiser, S. Mahajan, and S.R. Choudhury. *Concepts of modern physics*. Tata McGraw-Hill, Higher Education, 2003.

[29] P. Debye. Zur theorie der spezifischen warmen. *Annalen der Physik*, 344(14):789–839, 1912.

[30] Gizem KURT. Quantum transport in nanostructured materials. Master's thesis, Izmir Institute of Technology, July 2017.

[31] S.H. Simon. *The oxford solid state basics*. OUP Oxford, 2013.

[32] P. Atkins and J. de Paula. *Atkins' physical chemistry*. OUP Oxford, 2010.

[33] M. Buttiker. Absence of backscattering in the quantum hall effect in multiprobe conductors. *Phys. Rev. B*, 38:9375–9389, 1988.

[34] R. Landauer. Spatial variation of currents and fields due to localized scatterers in metallic conduction. *IBM Journal of Research and Development*, 1(3):223–231, 1957.

[35] Luis G. C. Rego and George Kirczenow. Quantized thermal conductance of dielectric quantum wires. *Phys. Rev. Lett.*, 81:232–235, 1998.

[36] Longji Cui, Wonho Jeong, Sunghoon Hur, Manuel Matt, Jan C. Klöckner, Fabian Pauly, Peter Nielaba, Juan Carlos Cuevas, Edgar Meyhofer, and Pramod Reddy. Quantized thermal transport in single-atom junctions. *Science*, 355(6330):1192–1195, 2017.

[37] K. Schwab, E. A. Henriksen, J. M. Worlock, and M. L. Roukes. Measurement of the quantum of thermal conductance. *Nature*, 404(6781):974–977, 2000.

[38] Paul A. Tipler. *Modern Physics*. Worth Publishers, Incorporated, 1977.

[39] J.P. Wolfe. *Imaging Phonons: Acoustic Wave Propagation in Solids*. Cambridge University Press, 2005.

[40] P. Atkins, V. Walters, J. De Paula, C. Trapp, and M. Cady. *Physical Chemistry for the Life Sciences*. Macmillan Higher Education, 2011.

[41] Konstantinos Termentzidis, Valentina M. Giordano, Maria Katsikini, Eleni Paloura, Gilles Pernot, Maxime Verdier, David Lacroix, Ioannis Karakostas, and Joseph Kioseoglou. Enhanced thermal conductivity in percolating nanocomposites: a molecular dynamics investigation. *Nanoscale*, 10:21732–21741, 2018.

[42] Jianjun Liu, Yang Liu, Yuhang Jing, Yufei Gao, Junqing Zhao, and Bin Ouyang. Phonon transport of zigzag/armchair graphene superlattice nanoribbons. *International Journal of Thermophysics*, 39(11):125, 2018.

[43] Kui-Kui Zhou, Ning Xu, and Guo-Feng Xie. Thermal conductivity of carbon nanotube superlattices: comparative study with defective carbon nanotubes. *Chinese Physics B*, 27(2):026501, 2018.

[44] Ming Hu Yuhang Jing. Phonon transport of rough si/ge superlattice nanotubes. *Computers, Materials & Continua*, 38(1):43–59, 2013.

[45] Ping Yang, Yunqing Tang, Haiying Yang, and Yongsheng Wu. Thermal conductivity reconstruction at tio2/zno multilayer nanoscale interface structure. *Science of Advanced Materials*, 6(9):1986–1992, 2014.

[46] Z. T. Tian, B. E. White, and Y. Sun. Phonon wave-packet interference and phonon tunneling based energy transport across nanostructured thin films. *Applied Physics Letters*, 96(26):263113, 2010.

[47] Zhiyong Wei, Zhonghua Ni, Kedong Bi, Minhua Chen, and Yunfei Chen. Interfacial thermal resistance in multilayer graphene structures. *Physics Letters A*, 375(8):1195 – 1199, 2011.

[48] V. Narayanamurti, H. L. Störmer, M. A. Chin, A. C. Gossard, and W. Wiegmann. Selective transmission of high-frequency phonons by a superlattice: the ”dielectric” phonon filter. *Phys. Rev. Lett.*, 43:2012–2016, 1979.

[49] O. Koblinger, J. Mebert, E. Dittrich, S. Döttinger, W. Eisenmenger, P. V. Santos, and L. Ley. Phonon stop bands in amorphous superlattices. *Phys. Rev. B*, 35:9372–9375, 1987.

[50] Seiji Mizuno and Shin-ichiro Tamura. Theory of acoustic-phonon transmission in finite-size superlattice systems. *Phys. Rev. B*, 45:734–741, 1992.

[51] Seiji Mizuno and Shin-ichiro Tamura. Impurity levels and resonant transmission of acoustic phonons in a double-barrier system. *Phys. Rev. B*, 45:13423–13430, 1992.

[52] Seiji Mizuno and Shin ichiro Tamura. Multiple-barrier systems for phonons: transmission characteristics. *Japanese Journal of Applied Physics*, 32(Part 1, No. 5B):2206–2209, 1993.

[53] Seiji Mizuno and Shin-ichiro Tamura. Transmission and reflection times of phonon packets propagating through superlattices. *Phys. Rev. B*, 50:7708–7718, 1994.

[54] Shin ichiro Tamura and Seiji Mizuno. Dynamic properties of phonons in superlattices. *Physica B: Condensed Matter*, 263-264:455 – 458, 1999.

[55] B. K. Ridley. Optical-phonon tunneling. *Phys. Rev. B*, 49:17253–17258, 1994.

[56] Fernando de León-Pérez and Rolando Pérez-Alvarez. Phonon propagation in nonpolar semiconductor heterostructures. *Phys. Rev. B*, 63:245304, 2001.

[57] Diosdado Villegas, Fernando de Leon-Perez, and Rolando Parez-Alvarez. Tunneling time for phonons: dependence on the system's size. *Physica Status Solidi (b)*, 242(9):1767–1770, 2005.

[58] Diosdado Villegas, Fernando de Leon-Perez, and Rolando Perez-Alvarez. Tunneling time of long-wavelength phonons through semiconductor heterostructures. *Phys. Rev. B*, 71:035322, 2005.

[59] Zorayda Lazcano, Pedro Luis Valdés Negrín, Diosdado Villegas, Jesus Arriaga, and Rolando Pérez-Álvarez. Tunneling times of acoustic phonon packets through a distributed bragg reflector. *Nanoscale Research Letters*, 9(1):449, 2014.

[60] Diosdado Villegas, Fernando de Leon Perez, R. Perez-Alvarez, and J. Arriaga. Phonon tunneling through a double barrier system. *Physica B: Condensed Matter*, 463:7 – 14, 2015.

[61] Gaokun Yu and Xinlong Wang. Extraordinary sound tunneling through a barred horn via subwavelength hole resonance. *Applied Physics Letters*, 99(25):254101, 2011.

[62] W. M. Robertson, J. Ash, and J. M. McGaugh. Breaking the sound barrier: Tunneling of acoustic waves through the forbidden transmission region of a one-dimensional acoustic band gap array. *American Journal of Physics*, 70(7):689–693, 2002.

[63] John H. Page, Suxia Yang, Zhengyou Liu, Michael Cowan, Che Chan, and Ping Sheng. Tunneling and dispersion in 3d phononic crystals. *Zeitschrift Fur Kristallographie - Z Kristallogr*, 220:859–870, 2005.

[64] Suxia Yang, J. H. Page, Zhengyou Liu, M. L. Cowan, C. T. Chan, and Ping Sheng. Ultrasound tunneling through 3d phononic crystals. *Phys. Rev. Lett.*, 88:104301, 2002.

[65] A. van Tiggelen and S.E. Skipetrov. *Wave scattering in complex media: from theory to applications*. Nato Science Series II:. Springer Netherlands, 2002.

[66] F. Van Der Biest, A Sukhovich, A Tourin, J. H Page, B. A. van Tiggelen, Z Liu, and M Fink. Resonant tunneling of acoustic waves through a double barrier consisting of two phononic crystals. *Europhysics Letters*, 71(1):63–69, 2005.

[67] A. Huynh, N. D. Lanzillotti-Kimura, B. Jusserand, B. Perrin, A. Fainstein, M. F. Pascual-Winter, E. Peronne, and A. Lemaître. Subterahertz phonon dynamics in acoustic nanocavities. *Phys. Rev. Lett.*, 97:115502, 2006.

[68] Dvira Segal and Bijay Kumar Agarwalla. Vibrational heat transport in molecular junctions. *Annual Review of Physical Chemistry*, 67(1):185–209, 2016.

[69] Min Nie, Dilhan M. Kalyon, Kishore Pochiraju, and Frank T. Fisher. A controllable way to measure the interfacial strength between carbon nanotube and polymer using a nanobridge structure. *Carbon*, 116:510–517, 2017.

[70] A.V. Khvalkovskii, K.A. Zvezdin, and A.K. Zvezdin. Transport and magnetic properties of magnetic planar nanobridge. *Microelectronic Engineering*, 81(2):336–340, 2005.

[71] Michael D. Fischbein and Marija Drndic. Nanogaps by direct lithography for high-resolution imaging and electronic characterization of nanostructures. *Applied Physics Letters*, 88(6):063116, 2006.

[72] Qian Li, Ivan Duchemin, Shiyun Xiong, Gemma C. Solomon, and Davide Donadio. Mechanical tuning of thermal transport in a molecular junction. *The Journal of Physical Chemistry C*, 119(43):24636–24642, 2015.

[73] Biswajit Pabi, Jakub Sebesta, Richard Korytar, Oren Tal, and Atindra Nath Pal. Structural regulation of mechanical gating in molecular junctions. *Nano Letters*, 23(9):3775–3780, 2023.

[74] Longji Cui, Sunghoon Hur, Zico Alaia Akbar, Jan C. Klockner, Wonho Jeong, Fabian Pauly, Sung-Yeon Jang, Pramod Reddy, and Edgar Meyhofer. Thermal conductance of single-molecule junctions. *Nature*, 572(7771):628–633, 2019.

[75] Wu-Xing Zhou, Yuan Cheng, Ke-Qiu Chen, Guofeng Xie, Tian Wang, and Gang Zhang. Thermal conductivity of amorphous materials. *Advanced Functional Materials*, 30(8):1903829, 2020.

[76] R. C. Zeller and R. O. Pohl. Thermal conductivity and specific heat of noncrystalline solids. *Phys. Rev. B*, 4:2029–2041, 1971.

[77] R. B. Stephens. Low-temperature specific heat and thermal conductivity of noncrystalline dielectric solids. *Phys. Rev. B*, 8:2896–2905, 1973.

[78] Glen A. Slack. The thermal conductivity of nonmetallic crystals. volume 34 of *Solid State Physics*, pages 1 – 71. Academic Press, 1979.

[79] David G. Cahill and R.O. Pohl. Heat flow and lattice vibrations in glasses. *Solid State Communications*, 70(10):927–930, 1989.

[80] David G. Cahill, S. K. Watson, and R. O. Pohl. Lower limit to the thermal conductivity of disordered crystals. *Phys. Rev. B*, 46:6131–6140, 1992.

[81] Matthias T. Agne, Riley Hanus, and G. Jeffrey Snyder. Minimum thermal conductivity in the context of diffuson-mediated thermal transport. *Energy Environ. Sci.*, 11:609–616, 2018.

[82] Hamid Reza Seyf, Luke Yates, Thomas L. Bougher, Samuel Graham, Baratunde A. Cola, Theeradetch Detchprohm, Mi-Hee Ji, Jeomoh Kim, Russell Dupuis, Wei Lv, and Asegun Henry. Rethinking phonons: the issue of disorder. *Npj Computational Materials*, 3(1):49, 2017.

[83] Philip B. Allen and Joseph L. Feldman. Thermal conductivity of disordered harmonic

solids. *Phys. Rev. B*, 48:12581–12588, 1993.

[84] Joseph L. Feldman, Mark D. Kluge, Philip B. Allen, and Frederick Wooten. Thermal conductivity and localization in glasses: numerical study of a model of amorphous silicon. *Phys. Rev. B*, 48:12589–12602, 1993.

[85] Philip B. Allen, Joseph L. Feldman, Jaroslav Fabian, and Frederick Wooten. Diffusons, locons and propagons: character of atomic vibrations in amorphous si. *Philosophical Magazine B*, 79(11-12):1715–1731, 1999.

[86] Jaeyun Moon Hamid Reza Seyf Austin J. Minnich Alan J. H. McGaughey Freddy DeAngelis, Murali Gopal Muraleedharan and Asegun Henry. Thermal transport in disordered materials. *Nanoscale and Microscale Thermophysical Engineering*, 23(2):81–116, 2019.

[87] Taishan Zhu and Elif Ertekin. Phonons, localization, and thermal conductivity of diamond nanothreads and amorphous graphene. *Nano Letters*, 16(8):4763–4772, 2016.

[88] G.P. Srivastava. *The physics of phonons*. Taylor & Francis, 1990.

[89] Gianluca Fiori, Francesco Bonaccorso, Giuseppe Iannaccone, Tomás Palacios, Daniel Neumaier, Alan Seabaugh, Sanjay K. Banerjee, and Luigi Colombo. Electronics based on two-dimensional materials. *Nature Nanotechnology*, 9(10):768–779, 2014.

[90] Fengnian Xia, Han Wang, Di Xiao, Madan Dubey, and Ashwin Ramasubramaniam. Two-dimensional material nanophotonics. *Nature Photonics*, 8(12):899–907, 2014.

[91] Xinyi Chia and Martin Pumera. Characteristics and performance of two-dimensional materials for electrocatalysis. *Nature Catalysis*, 1(12):909–921, 2018.

[92] Chunsen Liu, Huawei Chen, Shuiyuan Wang, Qi Liu, Yu-Gang Jiang, David Wei Zhang, Ming Liu, and Peng Zhou. Two-dimensional materials for next-generation computing technologies. *Nature Nanotechnology*, 15(7):545–557, 2020.

[93] Zhibin Yang, Jianhua Hao, and Shu Ping Lau. Synthesis, properties, and applications of 2d amorphous inorganic materials. *Journal of Applied Physics*, 127(22):220901, 2020.

[94] Hewei Zhao, Xiangjun Chen, Guangzhen Wang, Yongfu Qiu, and Lin Guo. Two-dimensional amorphous nanomaterials: synthesis and applications. *2d Materials*, 6(3):032002, 2019.

[95] Huarong Peng, Ming Zhou, Yanhong Li, Xun Cui, Yang Yang, Yunhuai Zhang, and Peng Xiao. Ultrahigh voltage synthesis of 2d amorphous nickel cobalt hydroxide nanosheets on cfp for high performance energy storage device. *Electrochimica Acta*, 190:695–702, 2016.

[96] Zhaoyong Lin, Chun Du, Bo Yan, Chengxin Wang, and Guowei Yang. Two-dimensional amorphous nio as a plasmonic photocatalyst for solar h2 evolution. *Nature Communications*, 9(1):4036, 2018.

[97] Juzhe Liu, Yongfei Ji, Jianwei Nai, Xiaogang Niu, Yi Luo, Lin Guo, and Shihe Yang. Ultrathin amorphous cobalt vanadium hydr(oxy)oxide catalysts for the oxygen evolution reaction. *Energy Environ. Sci.*, 11:1736–1741, 2018.

[98] Qiong Liu, Fengren Cao, Fangli Wu, Hao Lu, and Liang Li. Ultrathin amorphous ni(oh)2 nanosheets on ultrathin α-fe2o3 films for improved photoelectrochemical water oxidation. *Advanced Materials Interfaces*, 3(21):1600256, 2016.

[99] A. K. Geim and K. S. Novoselov. The rise of graphene. *Nature Materials*, 6(3):183–191, 2007.

[100] Francesco Bonaccorso, Luigi Colombo, Guihua Yu, Meryl Stoller, Valentina Tozzini, Andrea C. Ferrari, Rodney S. Ruoff, and Vittorio Pellegrini. Graphene, related two-dimensional crystals, and hybrid systems for energy conversion and storage. *Science*, 347(6217), 2015.

[101] Zhibin Yang, Jianhua Hao, Shuoguo Yuan, Shenghuang Lin, Hei Man Yau, Jiyan Dai, and Shu Ping Lau. Field-effect transistors based on amorphous black phosphorus ultrathin films by pulsed laser deposition. *Advanced Materials*, 27(25):3748–

3754, 2015.

[102] Chaoliang Tan, Xiehong Cao, Xue-Jun Wu, Qiyuan He, Jian Yang, Xiao Zhang, Junze Chen, Wei Zhao, Shikui Han, Gwang-Hyeon Nam, Melinda Sindoro, and Hua Zhang. Recent advances in ultrathin two-dimensional nanomaterials. *Chemical Reviews*, 117(9):6225–6331, 2017.

[103] Ming Wen, YaFen Wang, Qingsheng Wu, Yi Jin, and MingZhu Cheng. Controlled fabrication of 0 & 2d nicu amorphous nanoalloys by the cooperation of hard soft interfacial templates. *Journal of Colloid and Interface Science*, 342(2):229–235, 2010.

[104] Jeong Min Park, Jae Hyun Cho, Jung Hoon Ha, Hae Sik Kim, Sung Wook Kim, Jaejun Lee, Kyung Yoon Chung, Byung Won Cho, and Heon Jin Choi. Reversible crystalline-amorphous phase transformation in si nanosheets with lithidelithiation. *Nanotechnology*, 28(25):255401, 2017.

[105] Nicholas R. Glavin, Christopher Muratore, Michael L. Jespersen, Jianjun Hu, Phillip T. Hagerty, Al M. Hilton, Austin T. Blake, Christopher A. Grabowski, Michael F. Durstock, Michael E. McConney, Drew M. Hilgefort, Timothy S. Fisher, and Andrey A. Voevodin. Amorphous boron nitride: a universal, ultrathin dielectric for 2d nanoelectronics. *Advanced Functional Materials*, 26(16):2640–2647, 2016.

[106] Benjamin Sirota, Nicholas Glavin, Sergiy Krylyuk, Albert V. Davydov, and Andrey A. Voevodin. Hexagonal mote2 with amorphous bn passivation layer for improved oxidation resistance and endurance of 2d field effect transistors. *Scientific Reports*, 8(1):8668, 2018.

[107] Matthew Z. Bellus, Zhibin Yang, Peymon Zereshki, Jianhua Hao, Shu Ping Lau, and Hui Zhao. Efficient hole transfer from monolayer ws2 to ultrathin amorphous black phosphorus. *Nanoscale Horiz.*, 4:236–242, 2019.

[108] Matthew Z Bellus, Zhibin Yang, Jianhua Hao, Shu Ping Lau, and Hui Zhao. Amorphous two-dimensional black phosphorus with exceptional photocarrier transport properties. *2D Materials*, 4(2):025063, 2017.

[109] Xiaoyan Zhang, Libo Li, Yaxiao Guo, Dong Liu, and Tianyan You. Amorphous flower like molybdenum sulfide nitrogen doped carbon nanofiber film for use in the hydrogen evolution reaction. *Journal of Colloid and Interface Science*, 472:69–75, 2016.

[110] Min Qian, Yue Ping Niu, and Shang Qing Gong. Influence of laser wavelength on two-dimensional carbon nanosheet formation from laser-induced exfoliation of naphthalene. *Applied Surface Science*, 428:549–554, 2018.

[111] Xiang Ren, Dan Wu, Ruixiang Ge, Xu Sun, Hongmin Ma, Tao Yan, Yong Zhang, Bin Du, Qin Wei, and Liang Chen. Self-supported comos4 nanosheet array as an efficient catalyst for hydrogen evolution reaction at neutral ph. *Nano Research*, 11(4):2024–2033, 2018.

[112] K. S. Novoselov, A. K. Geim, S. V. Morozov, D. Jiang, Y. Zhang, S. V. Dubonos, I. V. Grigorieva, and A. A. Firsov. Electric field effect in atomically thin carbon films. *Science*, 306(5696):666–669, 2004.

[113] Changgu Lee, Xiaoding Wei, Jeffrey W. Kysar, and James Hone. Measurement of the elastic properties and intrinsic strength of monolayer graphene. *Science*, 321(5887):385–388, 2008.

[114] Alexander A. Balandin. Thermal properties of graphene and nanostructured carbon materials. *Nature Materials*, 10(8):569–581, 2011.

[115] J. R. Williams, L. DiCarlo, and C. M. Marcus. Quantum hall effect in a gate-controlled p-n junction of graphene. *Science*, 317(5838):638–641, 2007.

[116] Claire Berger, Zhimin Song, Tianbo Li, Xuebin Li, Asmerom Y. Ogbazghi, Rui Feng, Zhenting Dai, Alexei N. Marchenkov, Edward H. Conrad, Phillip N. First, and Walt A. de Heer. Ultrathin epitaxial graphite: 2d electron gas properties and a route toward graphene-based nanoelectronics. *The Journal of Physical Chemistry B*, 108(52):19912–19916, 2004.

[117] Emilie J. Siochi. Graphene in the sky and beyond. *Nature Nanotechnology*, 9(10):745–747, 2014.

[118] Tanmoy Das, Bhupendra K. Sharma, Ajit K. Katiyar, and Jong-Hyun Ahn. Graphene-based flexible and wearable electronics. *Journal of Semiconductors*, 39(1):011007, 2018.

[119] Felice Torrisi and Tian Carey. Graphene, related two-dimensional crystals and hybrid systems for printed and wearable electronics. *Nano Today*, 23:73–96, 2018.

[120] Jing Lin, Zhaoran Zhu, Chi Fai Cheung, Feng Yan, and Guijun Li. Digital manufacturing of functional materials for wearable electronics. *J. Mater. Chem. C*, 8:10587–10603, 2020.

[121] Andreas Isacsson, Aron W Cummings, Luciano Colombo, Luigi Colombo, Jari M Kinaret, and Stephan Roche. Scaling properties of polycrystalline graphene: a review. *2d Materials*, 4(1):012002, 2016.

[122] J. Kotakoski, A. V. Krasheninnikov, U. Kaiser, and J. C. Meyer. From point defects in graphene to two-dimensional amorphous carbon. *Phys. Rev. Lett.*, 106:105505, 2011.

[123] Jin Zhao, Guoyin Zhu, Wen Huang, Zhi He, Xiaomiao Feng, Yanwen Ma, Xiaochen Dong, Quli Fan, Lianhui Wang, Zheng Hu, Yinong Lu, and Wei Huang. Synthesis of large-scale undoped and nitrogen-doped amorphous graphene on mgo substrate by chemical vapor deposition. *J. Mater. Chem.*, 22:19679–19683, 2012.

[124] Mississippi Missouri Bhunia, Karamjyoti Panigrahi, Swati Das, Kalyan Kumar Chattopadhyay, and Paramita Chattopadhyay. Amorphous graphene transformer oil nanofluids with superior thermal and insulating properties. *Carbon*, 139:1010 – 1019, 2018.

[125] K.K. Chattopadhyay, D. Banerjee, N.S. Das, and D. Sarkar. Easy synthesis of amorphous graphene and related hybrids for cold cathode application. *Carbon*, 72:4 – 14, 2014.

[126] Aleandro Antidormi, Luciano Colombo, and Stephan Roche. Thermal transport in amorphous graphene with varying structural quality. *2d Materials*, 8(1):015028, dec 2020.

[127] Saeed Bazrafshan and Ali Rajabpour. Thermal transport engineering in amorphous graphene: non-equilibrium molecular dynamics study. *International Journal of Heat and Mass Transfer*, 112:379 – 386, 2017.

[128] Bohayra Mortazavi and Said Ahzi. Thermal conductivity and tensile response of defective graphene: a molecular dynamics study. *Carbon*, 63:460–470, 2013.

[129] Raghavan Ranganathan, Srujan Rokkam, Tapan Desai, and Pawel Keblinski. Generation of amorphous carbon models using liquid quench method: a reactive molecular dynamics study. *Carbon*, 113:87 – 99, 2017.

[130] Huifeng Tian, Zhixin Yao, Zhenjiang Li, Junjie Guo, and Lei Liu. Unlocking more potentials in two-dimensional space: disorder engineering in two-dimensional amorphous carbon. *ACS Nano*, 17(24):24468–24478, 2023.

[131] A. P. Thompson, H. M. Aktulga, R. Berger, D. S. Bolintineanu, W. M. Brown, P. S. Crozier, P. J. in 't Veld, A. Kohlmeyer, S. G. Moore, T. D. Nguyen, R. Shan, M. J. Stevens, J. Tranchida, C. Trott, and S. J. Plimpton. Lammps - a flexible simulation tool for particle-based materials modeling at the atomic, meso, and continuum scales. *Comp. Phys. Comm.*, 271:108171, 2022.

[132] Jianing Zhuang, Ruiqi Zhao, Jichen Dong, Tianying Yan, and Feng Ding. Evolution of domains and grain boundaries in graphene: a kinetic monte carlo simulation. *Phys. Chem. Chem. Phys.*, 18:2932–2939, 2016.

[133] Paul J. Steinhardt, David R. Nelson, and Marco Ronchetti. Bond-orientational order in liquids and glasses. *Phys. Rev. B*, 28:784–805, 1983.

[134] L. M. Ghiringhelli, C. Valeriani, E. J. Meijer, and D. Frenkel. Local structure of liquid carbon controls diamond nucleation. *Phys. Rev. Lett.*, 99:055702, 2007.

[135] Hossein Eslami, Neda Khanjari, and Florian Muller-Plathe. A local order parameter-based method for simulation of free energy barriers in crystal nucleation. *Journal of Chemical Theory and Computation*, 13(3):1307–1316, 2017.

[136] Batuhan Yildirim and Hamish Galloway Brown. by256/rdfpy: rdfpy-v1.0.0, March 2021.

[137] J. Tersoff. New empirical approach for the structure and energy of covalent systems. *Phys. Rev. B*, 37:6991–7000, 1988.

[138] J. Tersoff. Empirical interatomic potential for carbon, with applications to amorphous carbon. *Phys. Rev. Lett.*, 61:2879–2882, 1988.

[139] L. Lindsay and D. A. Broido. Optimized tersoff and brenner empirical potential parameters for lattice dynamics and phonon thermal transport in carbon nanotubes and graphene. *Phys. Rev. B*, 81:205441, 2010.

[140] M. Mohr, J. Maultzsch, E. Dobardzic, S. Reich, I. Milosevica, M. Damnjanovic, A. Bosak, M. Krisch, and C. Thomsen. Phonon dispersion of graphite by inelastic x-ray scattering. *Phys. Rev. B*, 76:035439, 2007.

[141] Asir Intisar Khan, Ishtiaque Ahmed Navid, Maliha Noshin, H. M. Ahsan Uddin, Fahim Ferdous Hossain, and Samia Subrina. Equilibrium molecular dynamics simulation study of thermal conductivity of graphene nanoribbon: a comparative study on md potentials. *Electronics*, 4(4):1109–1124, 2015.

[142] Wei-Jun Ren, Shuang Lu, Cui-Qian Yu, Jia He, and Jie Chen. Carbon honeycomb structure with high axial thermal transport and strong robustness. *Rare Metals*, 42(8):2679–2687, 2023.

[143] Hamoon Pourmirzaagha and Saeed Rouhi. Molecular dynamic simulations of the heat transfer in double-layered graphene/silicene nanosheets. *Physica B: Condensed Matter*, 666:415079, 2023.

[144] Reza Pahlavan Yali, Ali Mehri, and Maryam Jamaati. Nonlinear thermal transport in graphene nanoribbon: a molecular dynamics study. *Physica A: Statistical Mechanics and its Applications*, 610:128416, 2023.

[145] Cuiqian Yu, Shuyue Shan, Shuang Lu, Zhongwei Zhang, and Jie Chen. Characteristics of distinct thermal transport behaviors in single-layer and multilayer graphene. *Phys. Rev. B*, 107:165424, 2023.

[146] Yu Li and Jin-Wu Jiang. Modulation of thermal conductivity of single-walled carbon nanotubes by fullerene encapsulation: the effect of vacancy defects. *Phys. Chem.*

Chem. Phys., 25:7734–7740, 2023.

[147] Mingjian Zhou, Liqing Liu, Jiahao Liu, and Zihang Mei. Prediction and control of thermal transport at defective state gr/h-bn heterojunction interfaces. *Nanomaterials*, 13(9), 2023.

[148] Yajuan Cheng, Zheyong Fan, Tao Zhang, Masahiro Nomura, Sebastian Volz, Guimei Zhu, Baowen Li, and Shiyun Xiong. Magic angle in thermal conductivity of twisted bilayer graphene. *Materials Today Physics*, 35:101093, 2023.

[149] Wenkai Liu, Ling Qin, C. Y. Zhao, and Shenghong Ju. Microscopic mechanism of tunable thermal conductivity in carbon nanotube-geopolymer nanocomposites. *The Journal of Physical Chemistry B*, 127(10):2267–2276, 2023.

[150] Bingcheng Wang, Wei Shao, Qun Cao, and Zheng Cui. Investigation of the heat transport in intersected graphene. *International Journal of Heat and Mass Transfer*, 209:124162, 2023.

[151] Han Wei, Yue Hu, and Hua Bao. Influence of point defects and multiscale pores on the different phonon transport regimes. *Communications Materials*, 4(1):3, 2023.

[152] Zhiyong Wei, Yi Tao, Xi Lu, Yajing Kan, Yan Zhang, and Yunfei Chen. Frictional energy dissipation due to phonon resonance in two-layer graphene system. *Tribology Letters*, 70(4):113, 2022.

[153] Yun Dong, Weibin Hui, Fangming Lian, Yusong Ding, and Zhiyuan Rui. Phononic friction in monolayer/bilayer graphene. *Tribology Letters*, 70(3):72, May 2022.

[154] Xin Wu and Qiang Han. Tunable anisotropic in-plane thermal transport of multilayer graphene induced by 2d empty space: insights from interfaces. *Surfaces and Interfaces*, 33:102296, 2022.

[155] Meng An, Haotian Wang, Yuejin Yuan, Dongsheng Chen, Weigang Ma, Swellam W. Sharshir, Zhiheng Zheng, Yaoxiao Zhao, and Xing Zhang. Strong phonon coupling induces low thermal conductivity of one-dimensional carbon boron nanotube. *Surfaces and Interfaces*, 28:101690, 2022.

[156] Alexander V. Savin and Yuri S. Kivshar. Modeling of second sound in carbon nanostructures. *Phys. Rev. B*, 105:205414, 2022.

[157] Wenxiang Liu, Yang Hong, Jingchao Zhang, and Yanan Yue. Anisotropic thermal transport in twisted bilayer graphene. *Phys. Chem. Chem. Phys.*, 24:21722–21728, 2022.

[158] Xiang Huang, Shengluo Ma, Haidong Wang, Shangchao Lin, C.Y. Zhao, Hong Wang, and Shenghong Ju. Enhancing thermoelectric properties of isotope graphene nanoribbons via machine learning guided manipulation of disordered antidots and interfaces. *International Journal of Heat and Mass Transfer*, 197:123332, 2022.

[159] Xin Wu and Qiang Han. Maximum thermal conductivity of multilayer graphene with periodic two-dimensional empty space. *International Journal of Heat and Mass Transfer*, 191:122829, 2022.

[160] Wei-Jen Chen, Biao Feng, Cheng Shao, Jin Yang, Liwu Fan, Wee-Liat Ong, and I-Ling Chang. Asymmetrical carbon nanotubes exhibit opposing thermal rectification behaviors under different heat baths. *International Journal of Heat and Mass Transfer*, 184:122341, 2022.

[161] O. Farzadian, F. Yousefi, C. Spitas, and K.V. Kostas. Phonon heat transport in two-dimensional phagraphene-graphene superlattice. *International Journal of Heat and Mass Transfer*, 182:121917, 2022.

[162] Han Wei, Yue Hu, Hua Bao, and Xiulin Ruan. Quantifying the diverse wave effects in thermal transport of nanoporous graphene. *Carbon*, 197:18–26, 2022.

[163] Jun Cai, Ehsan Estakhrianhaghighi, and Abdolhamid Akbarzadeh. Functionalized graphene origami metamaterials with tunable thermal conductivity. *Carbon*, 191:610–624, 2022.

[164] Yu-Tian Zhang, Yun-Peng Wang, Yu-Yang Zhang, Shixuan Du, and Sokrates T. Pantelides. Thermal transport of monolayer amorphous carbon and boron nitride. *Applied Physics Letters*, 120(22):222201, 2022.

[165] Zhuoran Li, Peng He, Yunxia Ping, Na Guo, Xianzhe Zeng, Siwei Yang, and Guqiao

Ding. Dimension effects of graphene sheets as building blocks: Implications for thermal conductivity improvement of graphene films. *ACS Applied Nano Materials*, 5(8):10471–10484, 2022.

[166] Giuseppe Barbalinardo, Zekun Chen, Haikuan Dong, Zheyong Fan, and Davide Donadio. Ultrahigh convergent thermal conductivity of carbon nanotubes from comprehensive atomistic modeling. *Phys. Rev. Lett.*, 127:025902, 2021.

[167] Masato Ohnishi and Junichiro Shiomi. Strain-induced band modulation of thermal phonons in carbon nanotubes. *Phys. Rev. B*, 104:014306, 2021.

[168] Daniel Bruns, Alireza Nojeh, A. Srikantha Phani, and Jörg Rottler. Nanotube heat conductors under tensile strain: Reducing the three-phonon scattering strength of acoustic phonons. *Phys. Rev. B*, 104:075440, 2021.

[169] Wenxiang Liu, Yongqiang Wu, Yang Hong, Bo Hou, Jingchao Zhang, and Yanan Yue. Full-spectrum thermal analysis in twisted bilayer graphene. *Phys. Chem. Chem. Phys.*, 23:19166–19172, 2021.

[170] Huicong Dong, Shuaichao Yu, Zhihao Feng, and Bin Wen. Structural property-induced different phonon-twin-boundary scattering in diamond. *Phys. Chem. Chem. Phys.*, 23:3874–3882, 2021.

[171] Xiao Wan, Dengke Ma, Dongkai Pan, Lina Yang, and Nuo Yang. Optimizing thermal transport in graphene nanoribbon based on phonon resonance hybridization. *Materials Today Physics*, 20:100445, 2021.

[172] Mohammad Nasr Esfahani, Masoud Jabbari, Yongbing Xu, and Costas Soutis. Effect of nanoscale defects on the thermal conductivity of graphene. *Materials Today Communications*, 26:101856, 2021.

[173] Qing-Gang Li, Xiao-Meng Zhang, Chao Si, Long Han, Ying-Jie Zhong, Xiao-Dong Wang, and Long Jiao. Phononic analyses of rectangular graphene and annular graphene under in-plane shear stress. *Journal of Applied Physics*, 129(23):233101, 2021.

[174] Chenghao Diao, Yuan Dong, and Jian Lin. Reactive force field simulation on thermal

conductivities of carbon nanotubes and graphene. *International Journal of Heat and Mass Transfer*, 112:903–912, 2017.

[175] Xin Mu, Xufei Wu, Teng Zhang, David B. Go, and Tengfei Luo. Thermal transport in graphene oxide: from ballistic extreme to amorphous limit. *Scientific Reports*, 4(1):3909, 2014.

[176] Takahiro Yamamoto and Kazuyuki Watanabe. Nonequilibrium green's function approach to phonon transport in defective carbon nanotubes. *Phys. Rev. Lett.*, 96:255503, 2006.

[177] T. S. Fisher W. Zhang and N. Mingo. The atomistic green's function method: an efficient simulation approach for nanoscale phonon transport. *Numerical Heat Transfer, Part B: Fundamentals*, 51(4):333–349, 2007.

[178] M P Lopez Sancho, J M Lopez Sancho, J M L Sancho, and J Rubio. Highly convergent schemes for the calculation of bulk and surface green functions. *Journal of Physics F: Metal Physics*, 15(4):851, 1985.

[179] F. Guinea, C. Tejedor, F. Flores, and E. Louis. Effective two-dimensional hamiltonian at surfaces. *Phys. Rev. B*, 28:4397–4402, 1983.

[180] Marco Buongiorno Nardelli. Electronic transport in extended systems: application to carbon nanotubes. *Phys. Rev. B*, 60:7828–7833, 1999.

[181] Norbert Nemec. *Quantum transport in carbon-based nanostructures*. PhD thesis, University of Regensburg, July 2007.

[182] H Sevincli, S Roche, G Cuniberti, M Brandbyge, R Gutierrez, and L Medrano Sandonas. Green function, quasi-classical langevin and kubo-greenwood methods in quantum thermal transport. *Journal of Physics: Condensed Matter*, 31(27):273003, 2019.

[183] Wu Li, Hâldun Sevincli, Stephan Roche, and Gianaurelio Cuniberti. Efficient linear scaling method for computing the thermal conductivity of disordered materials. *Phys. Rev. B*, 83:155416, 2011.

[184] L.E.F.F. Torres, S. Roche, and J.C. Charlier. *Introduction to graphene-based nanomaterials: from electronic structure to quantum transport*. Cambridge University Press, 2014.

[185] Atsushi Togo, Laurent Chaput, Terumasa Tadano, and Isao Tanaka. Implementation strategies in phonopy and phono3py. *J. Phys. Condens. Matter*, 35(35):353001, 2023.

[186] Atsushi Togo. First-principles phonon calculations with phonopy and phono3py. *J. Phys. Soc. Jpn.*, 92(1):012001, 2023.

[187] Cornelius Lanczos. An iteration method for the solution of the eigenvalue problem of linear differential and integral operators. *Journal of Research of the National Bureau of Standards*, 45(4), 1950.

[188] Yousef Saad. *Iterative methods for sparse linear systems*. Other titles in applied mathematics. SIAM, second edition, 2003.

[189] T.J. Rivlin. *Chebyshev polynomials*. Dover books on mathematics. Dover Publications, 2020.

[190] Francis Begnaud. Hildebrand. *Introduction to numerical analysis*. McGraw-Hill New York, 2d ed. edition, 1973.

[191] Zheyong Fan, Jose H. Garcia, Aron W. Cummings, Jose Eduardo Barrios-Vargas, Michel Panhans, Ari Harju, Frank Ortmann, and Stephan Roche. Linear scaling quantum transport methodologies. *Physics Reports*, 903:1–69, 2021.

[192] A. G. Greenhill. A treatise on bessel functions and their applications to physics. *Nature*, 52(1353):542–543.

[193] P. G. Klemens and Franz Eugen Simon. The thermal conductivity of dielectric solids at low temperatures (theoretical). *Proceedings of the Royal Society of London. Series A. Mathematical and Physical Sciences*, 208(1092):108–133, 1951.

[194] Gabriel Stoltz, Natalio Mingo, and Francesco Mauri. Reducing the thermal conductivity of carbon nanotubes below the random isotope limit. *Phys. Rev. B*,

80:113408, 2009.

[195] C. Kittel. *Introduction to solid state physics*. Wiley, 2004.

[196] N.W. Ashcroft and N.D. Mermin. *Solid state physics*. Hrw international editions. Holt, Rinehart and Winston, 1976.

[197] P. Hofmann. *Solid state physics: an introduction*. Wiley, 2015.

[198] Toshio Suzuki and Paul K.L. Yu. Complex elastic wave band structures in three-dimensional periodic elastic media. *Journal of the Mechanics and Physics of Solids*, 46(1):115 – 138, 1998.

[199] Ch. Fabry and A. Perot. On a new form of interferometer. *The Astrophysical Journal*, 13:265, 1970.

[200] A. Perot and Charles Fabry. On the application of interference phenomena to the solution of various problems of spectroscopy and metrology. *The Astrophysical Journal*, 9:87, 1970.

[201] P. Hariharan. Chapter 5 multiple-beam interference. In P. Hariharan, editor, *Basics of Interferometry*, pages 37 – 43. Academic Press, San Diego, 1992.

[202] Cefe Lepez. The true value of disorder. *Advanced Optical Materials*, 6(16):1800439, 2018.

[203] Pan Ren, Yamei Liu, Jian He, Tu Lv, Junling Gao, and Guiying Xu. Recent advances in inorganic material thermoelectrics. *Inorganic Chemistry Frontiers*, 5:2380, 2018.

[204] P. W. Anderson. Absence of diffusion in certain random lattices. *Physical Review*, 109(5):1492, 1958.

[205] Jianxiong Zhai, Qingyun Zhang, Zihan Cheng, Jie Ren, Youqi Ke, and Baowen Li. Anomalous transparency induced by cooperative disorders in phonon transport. *Phys. Rev. B*, 99:195429, 2019.

[206] Yangsu Xie, Zaoli Xu, Shen Xu, Zhe Cheng, Nastaran Hashemi, Cheng Deng, and Xinwei Wang. The defect level and ideal thermal conductivity of graphene uncovered by residual thermal reffusivity at the 0 k limit. *Nanoscale*, 7:10101–10110, 2015.

[207] P. L. Kapitza. Heat transfer and superfluidity of helium ii. *Phys. Rev.*, 60:354–355, 1941.

[208] Philippe Jund and Rémi Jullien. Molecular dynamics calculation of the thermal conductivity of vitreous silica. *Phys. Rev. B*, 59:13707–13711, 1999.

APPENDIX A

AMORPHOUS GRAPHENE STRUCTURES

As a supplement, we have added all the structures used in the transmission and thermal conductivity calculations achieved within Green's functions. Colormap represents the individual q3 value of carbon atoms and can be seen; blue(red) represents one(zero). For systems designed for Green's function method, the systems' local bond order parameters are averaged over just scattering region atoms; the buffer and reservoir regions are excluded from the average. The structures are documented in ascending order of iteration from top to bottom. The amorphization algorithm starts with a pristine graphene structure and runs towards a lower q3 value. The crystallization algorithm begins with a random network, and as iteration progresses, the system moves toward a higher q3 value. The q3 values of some hexagons are below one because of the out-of-plane deteriorations. The device lengths of the systems whose results are exhibited in the central part are 4.0 nanometers. While the device length of the configurations we call short is 1.6 nm, the distance of the devices we call long is 7.5 nanometers. The width of all systems is 10 nm long. The length of the system with a scattering region of four nanometers is 14 nm, and the length of the system with a scattering region of 1.6(7.5) nm is 11.6(17.5) nm. We have again printed the partition figure(Fig.4.1) here for a complete look.

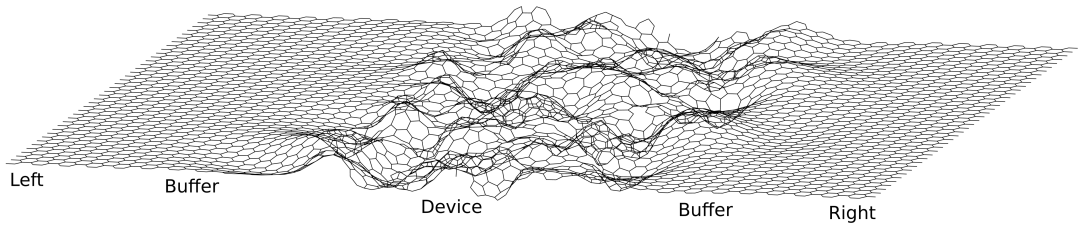

Figure A1. The partition of the structure as the left, the device, and the right system is shown.

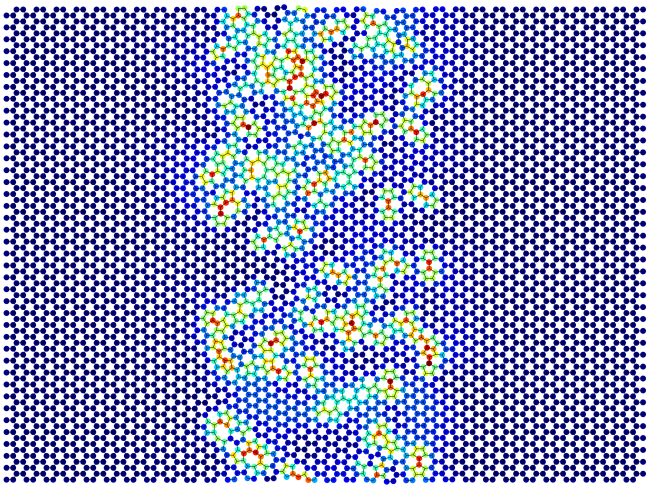

(a) q3: 0.70, 149th step

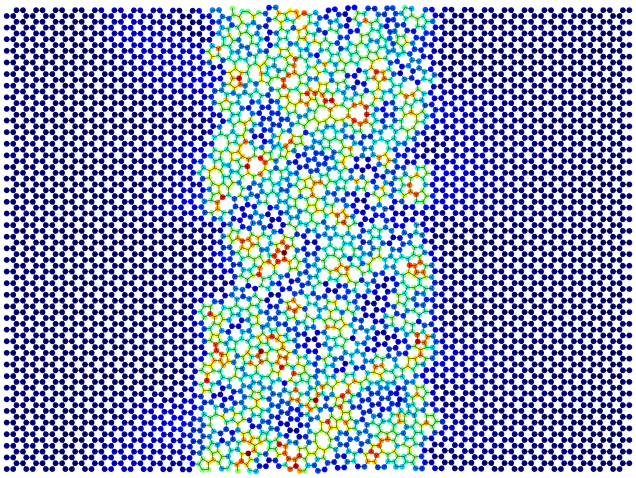

(b) q3: 0.55, 553th step

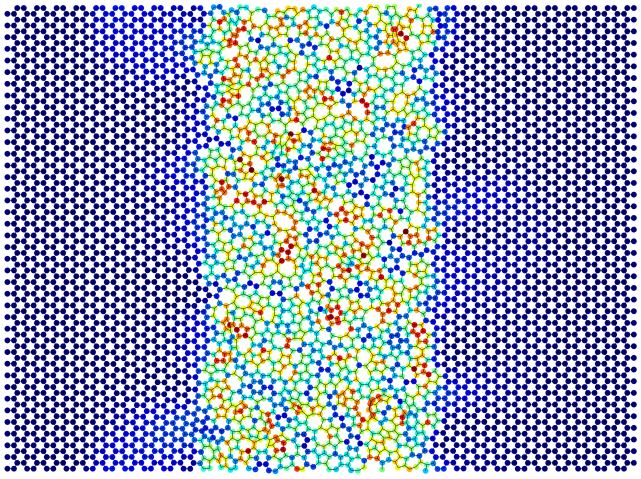

(c) q3: 0.40, 8441th step

Figure A2. 3CGM type configurations, device length: 4.0 nm

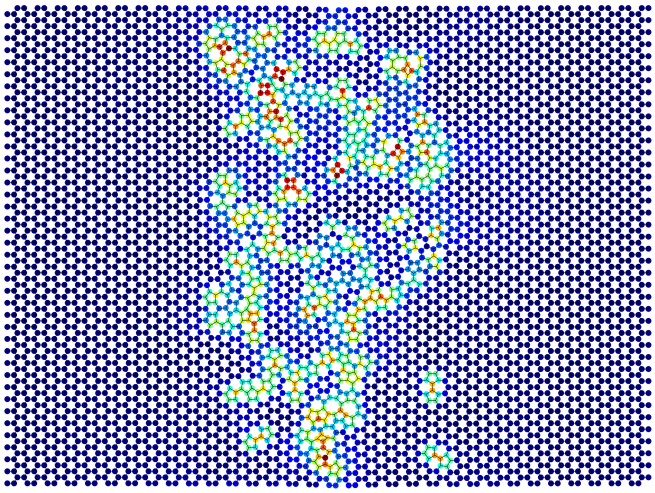

(a) q3: 0.70, 126th step

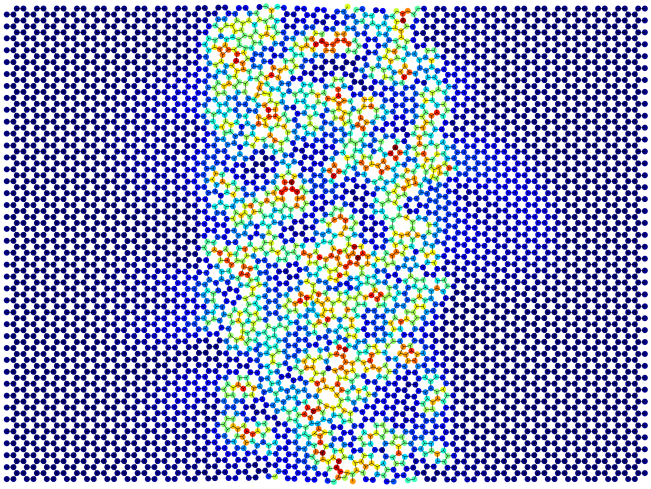

(b) q3: 0.55, 249th step

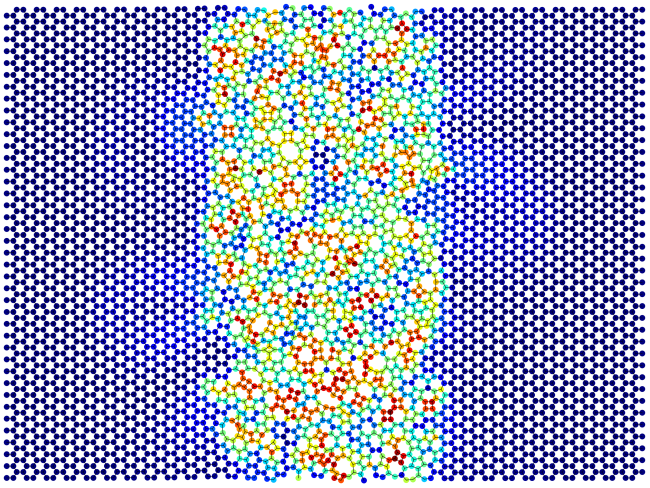

(c) q3: 0.40, 500th step

Figure A3. 3C type configurations, device length: 4.0 nm

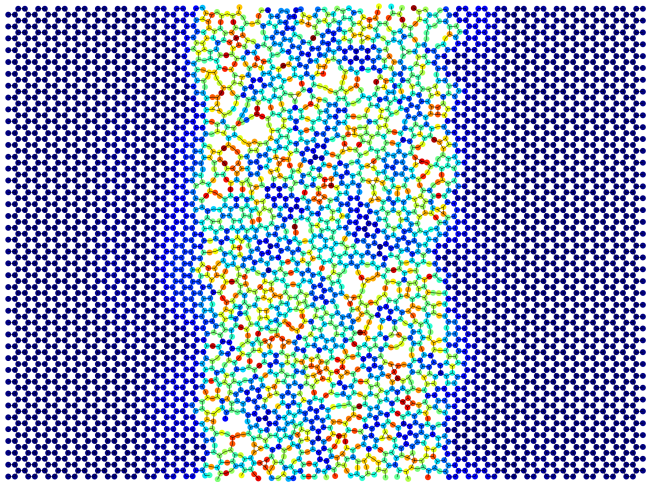

(a) q3: 0.40, 5362th step

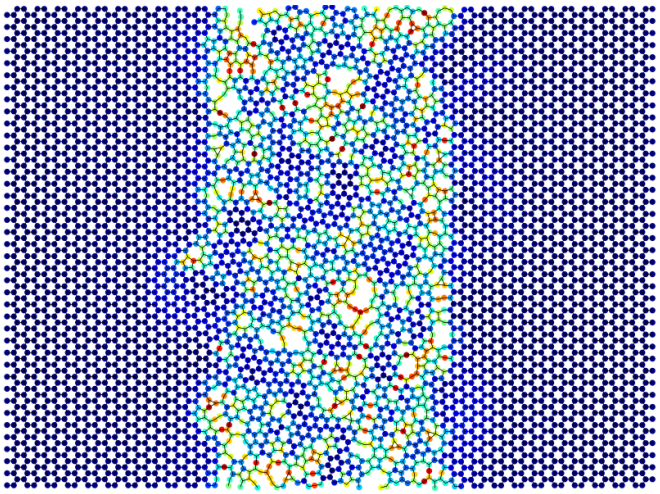

(b) q3: 0.55, 26152th step

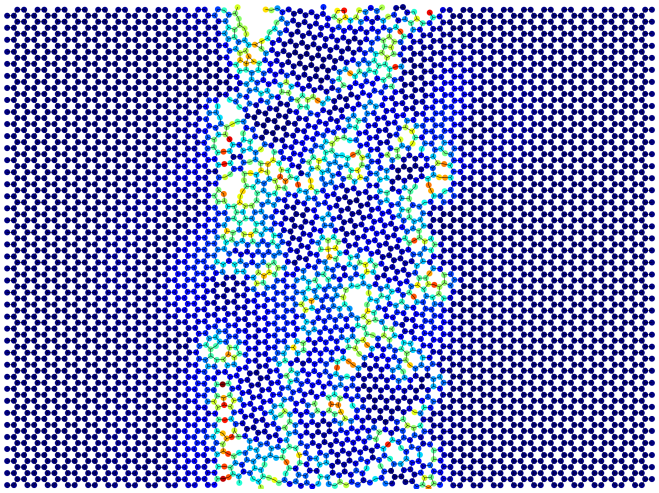

(c) q3: 0.70, 93996th step

Figure A4. NC type configurations, device length: 4.0 nm

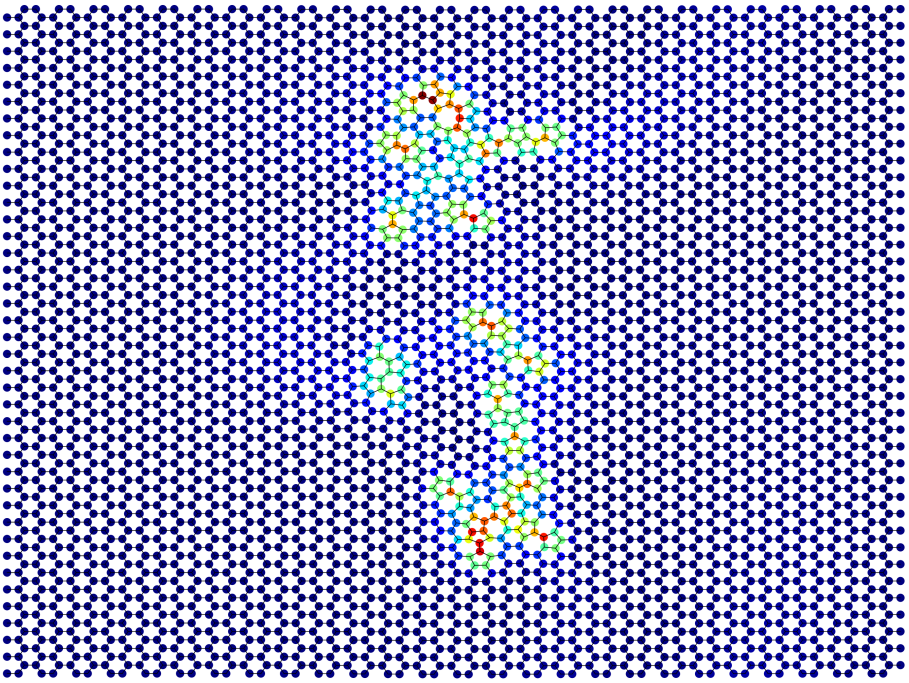

(a) q3: 0.70, 36th step

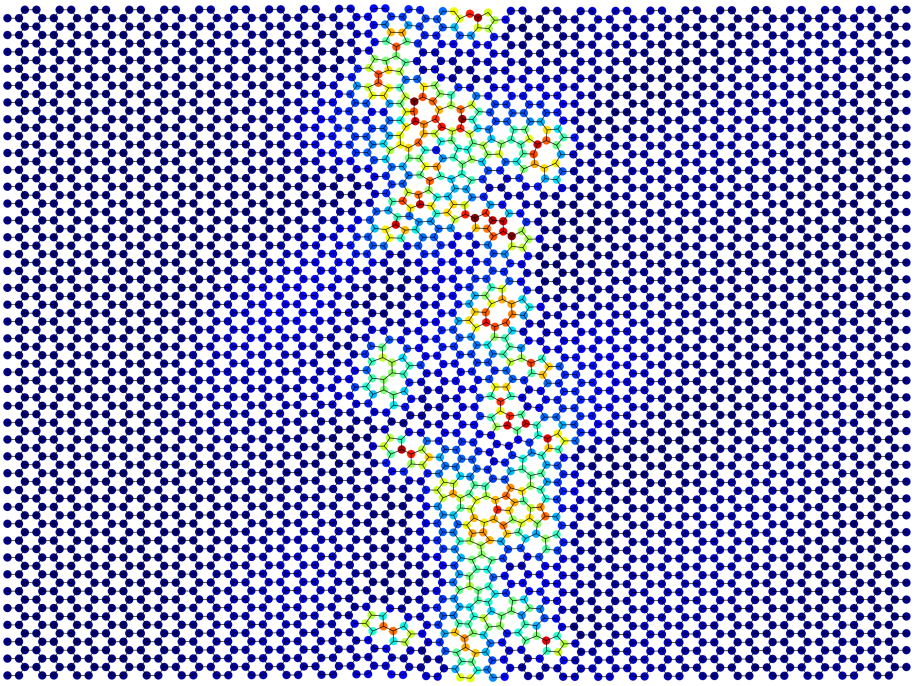

(b) q3: 0.55, 64th step

Figure A5. 3CGM configuration type, device length: 1.6 nm

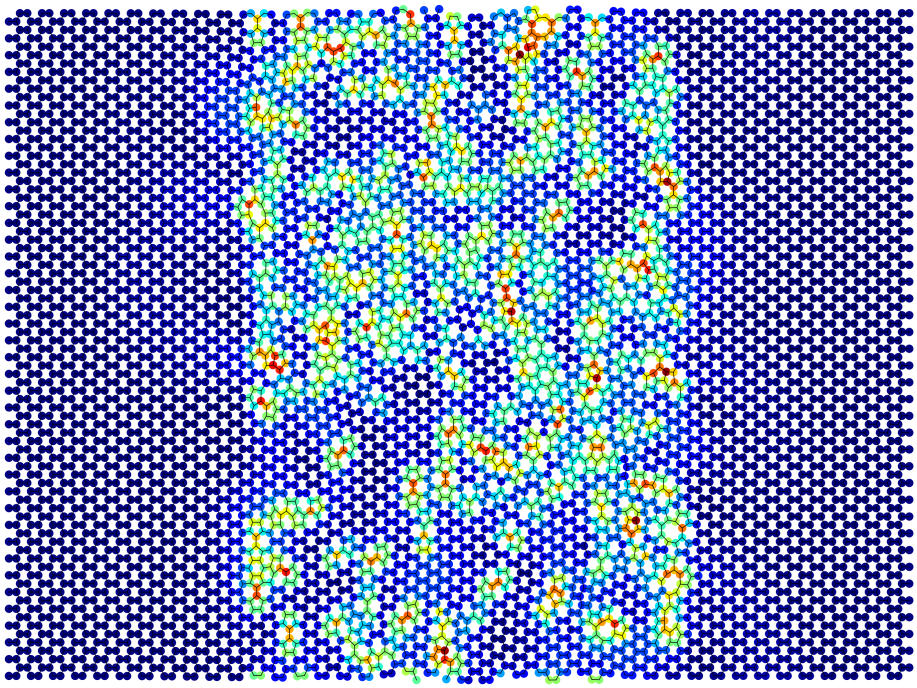

(a) q3: 0.70, 357th step

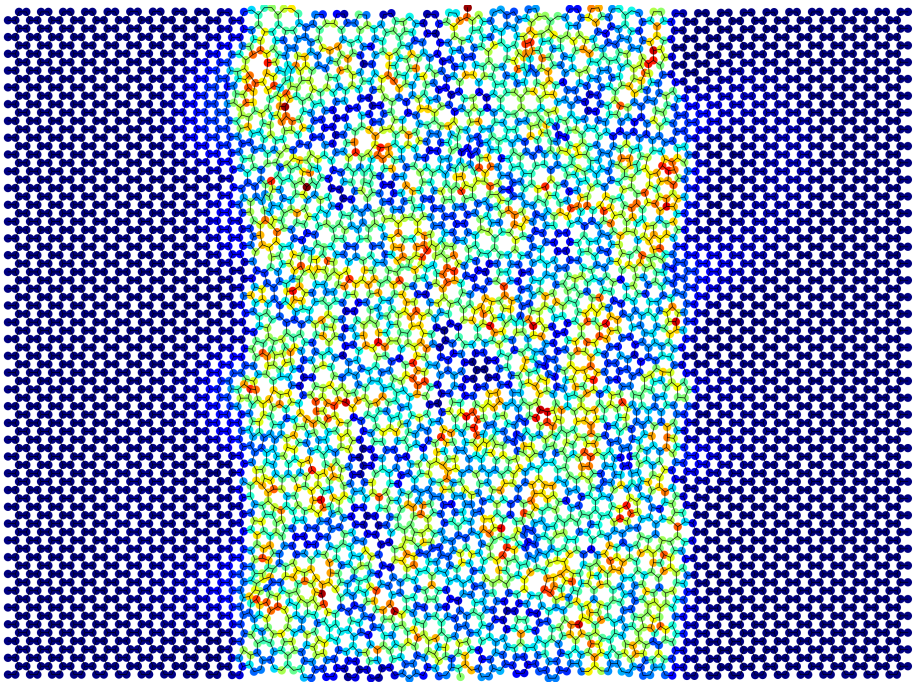

(b) q3: 0.55, 8122th step

Figure A6. 3CGM type configurations, device length: 7.5 nm

VITA

Gizem KURT

Education
Ph.D. in Materials Science and Engineering
Izmir Institute of Technology, 2023
M.Sc. in Materials Science and Engineering
Izmir Institute of Technology, 2017
B.Sc. in Chemistry
Izmir Institute of Technology, 2014

Employment
Izmir Institute of Technology, Research and Teaching Assistant, from 2015

Projects
Researcher in TUBITAK-117F480
"Mechanic: Modeling Charge and Thermal Transport in Two-Dimensional Material-Based Composites"
Researcher in TUBITAK-119F353
"Effects of disorder and multiparticle interactions on transport in systems with quartic dispersion"

Teaching Experience
Assistant, Introduction to Computer Programming
Assistant, Solid State Physics
Assistant, Materials Physics
Assistant, Introduction to Quantum Chemistry
Assistant, Atomic Simulation of Materials

Publications
"Ballistic thermoelectric transport properties of two-dimensional group III-VI monolayers"
M.Çınar, G. Ö. Sargın, K. Sevim, B. Özdamar, **G. Kurt**, and H. Sevinçli
Phys. Rev. B 103, 16542 (2021)
"First-principles based investigation of photoisomeric switching of vibrational heat current across molecular junctions"
G. Kurt and H. Sevinçli
Physical Review Applied 14, 064045 (2020)
"Structural, vibrational, and electronic properties of single-layer hexagonal crystals of group IV and V elements"
B. Özdamar, G. Özbal, M. N. Çınar, K. Sevim**, G. Kurt,** B. Kaya, H. Sevinçli
Physical Review B 98, 045431 (2018)